



EJBI 2013

ISSN 1801 - 5603

An Official Journal of the European Federation for Medical Informatics

European Journal for Biomedical Informatics

Volume 9 (2013), Issue 2

Special Topic

**Applications of Computational Techniques in Infectious
Diseases and Clinical Research**

Editors

Mannar Jawahar Ponnuswamy, Kamalanand Krishnamurthy

www.ejbi.eu

Aims and Scope

The **European Journal for Biomedical Informatics** reacts on the great European need to share the information in the multilingual and multicultural European area. The journal publishes peer-reviewed papers in English and other European languages simultaneously. This opens new possibilities for faster transfer of scientific-research pieces of knowledge to large international community of biomedical researchers, physicians, other health personnel and citizens. From time to time, the journal publishes articles on particular focus themes as part of a journal's issue.

The generally accepted translations of the English version of the abstract and keywords or full paper are to the European languages, which can be found at <http://www.ejbi.org/en/about/>.

Editors and Management

Editor in Chief

Jana Zvárová, Czech Republic

Managing Editor

Petra Přechková, Czech Republic

Graphic Design

Anna Schlenker, Czech Republic

Sales and Marketing Manager

Karel Zvára, Czech Republic

Editorial Board: National Members

Ammenwerth, Elske	Austria
Masic, Izet	Bosnia and Herzegovina
Vinarova, Jivka	Bulgaria
Kern, Josipa	Croatia
Zvárová, Jana	Czech Republic
Andersen, Stig Kjaer	Denmark
Ruotsalainen, Pekka	Finland
Degoulet, Patrice	France
Horsch, Alexander	Germany
Mantas, John	Greece
Surján, György	Hungary
Hurl, Gerard	Ireland
Reichert, Assa	Israel
Mazzoleni, Cristina	Italy
Lukosevicius, Arunas	Lithuania
Hofdijk, Jacob	Netherlands
Moen, Anne	Norway
Bobrowski, Leon	Poland
da Costa Pereira, Altamiro	Portugal
Mihalas, George	Romania
Shifrin, Michael	Russian Federation
Živčák, Jozef	Slovakia
Orel, Andrej	Slovenia
Nordberg, Ragnar	Sweden

Lovis, Christian	Switzerland
Saka, Osman	Turkey
Mayorow, Oleg	Ukraine
de Lusignan, Simon	United Kingdom

Editorial Board: Representatives of Cooperating Journals

Mayorow, Oleg	Clinical Informatics and Telemedicine
Marolt, Christian	Health IT Management
Brumini, Gordana	Hrvatski društvo za medicinsku informatiku
Rosina, Jozef	Lékař a technika
Svačina, Štěpán	Medicína po promoci
Haux, Reinhold	Methods of Information in Medicine

Publisher

EuroMISE s.r.o.
Paprsková 330/15
CZ-14000 Praha 4
Czech Republic
EU VAT ID: CZ25666011

Office

EuroMISE s.r.o.
Paprsková 330/15
CZ-14000 Praha 4
Czech Republic

Contact

Karel Zvára
zvara@euromise.com

Instructions to Authors

Please access <http://www.ejbi.org/en/instructions/>

EJBI Online

The online version of the full volume is available at <http://www.ejbi.org/en/ejbi/>.

Instructions to Authors

General Remarks

This journal follows the guidelines of the International Committee of Medical Journal Editors (<http://www.icmje.org/index.html>) and the Committee on Publication Ethics (<http://www.publicationethics.org>).

Authors should especially be aware of the following relevant issues in these guidelines:

Authorship

All authors should have made

- (1) substantial contributions to conception and design, acquisition of data, or analysis and interpretation of data;
- (2) drafting the article or revising it critically for important intellectual content; and
- (3) final approval of the version to be published.

Conflicts of interest

All authors must disclose any financial and personal relationships with other people or organizations that could inappropriately influence (bias) their actions.

Protection of human subjects and animals in research

Authors who submit a manuscript on research involving human subjects should indicate in the manuscript whether the procedures followed were in compliance with the ethical standards of the responsible committee on human experimentation (institutional and national) and with the World Medical Association Declaration of Helsinki on Ethical Principles for Medical Research Involving Human Subjects (<http://www.wma.net/en/30publications/10policies/b3/>).

European Journal for Biomedical Informatics does not publish material that has already appeared elsewhere. Submitted manuscripts should not be submitted in parallel to any other journal.

Manuscript preparation

Authors are kindly requested to carefully follow all instructions on how to write a paper. In cases where the instructions are not followed, the paper will be returned immediately with a request for changes, and the editorial review process will only start when the paper has been resubmitted in the correct style.

Authors are responsible for obtaining permission to reproduce any copyrighted material and this permission should be acknowledged in the paper.

Authors should not use the names of patients. Patients should not be recognizable from photographs unless their

written permission has first been obtained. This permission should be acknowledged in the paper.

In general the manuscript text (excluding summary, references, figures, and tables) should not exceed 5 000 words.

Kindly send the final and checked source and PDF files of your paper to manuscripts@ejbi.org. You should make sure that the L^AT_EX and the PDF files are identical and correct and that only one version of your paper is sent. Please note that we do not need the printed paper.

Where appropriate, the paper should be organised into the following sections: *Abstract, Introduction, Objectives, Methods, Results, Discussion, Conclusions, Acknowledgments and References*. Apart from the main headings, subheadings should be used and may be numbered.

Authors are strongly encouraged to use L^AT_EX 2_ε for the preparation of manuscript. The L^AT_EX template `ejbi_template.tex` can be downloaded from www.ejbi.org/en/instructions/.

When you are not able to use L^AT_EX, please use MS Word or OO Writer and send us the unformatted text. Kindly follow just instructions about preparing figures, tables and references. We are going to convert your text into L^AT_EX instead of you.

If you use L^AT_EX together with our template file, `ejbi_template.tex`, your text is typeset automatically. Please do *not* change the preset fonts. Do not use your own macros, or styles.

Please use the commands `\label` and `\ref` for cross-references and the commands `\bibitem` and `\cite` for references to the bibliography, to enable us to create hyperlinks at these places.

Title page

The first page of the article should contain: title of the paper (also the shorter version for running heads), initials and last name of each author, to be followed with their institutional affiliations, the name, address, e-mail address and telephone of the corresponding author.

Abstract and Keywords

The abstract should summarize the contents of the paper and should not exceed 250 words. Authors are requested to write a structured summary, adhering to the following headings: Background (optional), Objectives, Methods, Results, Conclusions.

At the end of the Abstract, the contents of the paper should be specified by, at most, five keywords. We recommend using MeSH keywords.

Headings

Headings should be capitalized (i.e. nouns, verbs, and all other words except articles, prepositions, and conjunctions should be set with an initial capital) and should be aligned to the left. Words joined by a hyphen are subject

to a special rule. If the first word can stand alone, the second word should be capitalized.

Figures and Tables

Attach figures and tables as separate files. Do not integrate them into the text. Do not save your table as an image file or insert a table into your manuscript text document as an image. Figures and tables should be referenced in the manuscript by their numbers.

Annotations belong in a (self-)explanatory legend, do not use headings in the figure, explain abbreviations in the legend. Label all axes. Use a uniform type size (we recommend Arial 10 point), and avoid borders around tables and figures.

Submit graphics as a sharp printout as well as a file. The printout and the file must be identical. Submit the image file with clear labelling (e.g. Fig_1 instead of joint_ap).

Image resolution is the number of dots per width of 1 inch, the "dots per inch" (dpi). Printing images require a resolution of 800 dpi for graphics and 300 dpi for photographs.

Vector graphics have no resolution problems. Some programs produce images not with a limited number of dots but as a vector graphic. Vectorisation eliminates the problem of resolution. However, if halftone images ("photos") are copied into such a program, these images retain their low resolution.

If screenshots are necessary, please make sure that you are happy with the print quality before you send the files.

In the printed volumes, illustrations are generally black and white (halftones), and only in exceptional cases, and if the author is prepared to cover the extra cost for colour reproduction, are coloured pictures accepted. Coloured pictures are welcome in the electronic version free of charge. If you send coloured figures that are to be printed in black and white, please make sure that they really are legible in black and white. Some colours as well as the contrast of converted colours show up very poorly when printed in black and white.

Formulas

Displayed equations or formulas are centred and set on a separate line (with an extra line or halfline space above and below). Displayed expressions should be numbered for reference. The numbers should be consecutive within each section or within the contribution, with numbers enclosed in parentheses and set on the right margin.

Footnotes

The superscript numeral used to refer to a footnote appears in the text either directly after the word to be

¹The footnote numeral is set flush left and the text follows with the usual word spacing.

discussed or – in relation to a phrase or a sentence – following the punctuation sign (comma, semicolon, or period). Footnotes should appear at the bottom of the normal text area, with a line of about 2 cm set immediately above them.¹

Program Code

Program listings or program commands in the text are normally set in a typewriter font, e.g. CMTT10 or Courier.

Acknowledgements

Scientific advice, technical assistance, and credit for financial support and materials may be grouped in a section headed Acknowledgements that will appear at the end of the text (immediately after the Conclusions section). The heading should be treated as a subsubsection heading and should not be assigned a number.

In case that a financial support of the paper development (e.g. sponsors, projects) is acknowledged, the fee of 50 EUR will be charged by Publisher. The accepted peer-reviewed papers with an acknowledgement of a financial support, where the fee was not paid, will be published free of charge, but the financial acknowledgement will be withdrawn.

References

The list of references is headed "References" and is not assigned a number. The list should be set in small print and placed at the end of your contribution, in front of the appendix, if one exists. Please do not insert a pagebreak before the list of references if the page is not completely filled. For citations in the text please use square brackets. In the text number the references consecutively in the order in which they first appear. Use the style, which is based on the formats used by the US National Library of Medicine in MEDLINE (sometimes called the "Vancouver style"). For details see the guidelines from the International Committee of Medical Journal Editors (http://www.nlm.nih.gov/bsd/uniform_requirements.html).

Examples:

- [1] Blobel B. Architectural Approach to eHealth for Enabling Paradigm Changes in Health. *Methods Inf Med.* 2010; 49(2): 123–134.
- [2] Kalina J. Robustní analýza obrazu obličeje pro genetické aplikace. *EJBI [Internet]*. 2010 [cited 2011 Jun 28]; 6(2): cs95–cs102. Available from: <http://www.ejbi.eu/articles/201012/47/2.html>
- [3] van Bommel JH, Musen M, editors. *Handbook of Medical Informatics*. Heidelberg: Springer; 1997.

- [4] Zvarova J, Zvara K. e3Health: Three Main Features of Modern Healthcare. In: Mourtoglou A, Kastania A. E-Health Systems Quality and Reliability: Models and Standards, Hershey: IGI Global; 2010; 18–27.

Multilingual Issue

The authors are asked to translate English version of Abstract and Keywords to at least one European language. The translated versions of Abstract and Keywords should be sent to manuscripts@ejbi.org

Checking the PDF File

Kindly assure that the Contact Volume Editor is given the name and email address of the contact author for your paper. The contact author is asked to check through the final PDF files to make sure that no errors have crept in during the transfer or preparation of the files. Only errors introduced during the preparation of the files will be corrected.

If we do not receive a reply from a particular contact author, within the timeframe given, then it is presumed that the author has found no errors in the paper.

Copyright Transfer Agreement

The copyright form may be downloaded from <http://www.ejbi.org/en/downloads/>. Please send your signed copyright form to the Contact Volume Editor, either as a scanned pdf or by fax or by courier. One author may sign on behalf of all the other authors of a particular paper. Digital signatures are acceptable.

EuroMISE Copyright Permission Policy

Written permission is required to reproduce material from EuroMISE s.r.o. publications in other publications, electronic products, or other media. To obtain a copyright permission please contact Jana Zvárová: zvarova@ejbi.org, fax: +420 241471337. You may fax or e-mail your request along with the full citation of the journal in which the paper appears in with volume number and page number(s) as well as what you are requesting to use the material for. Use of copyrighted material always requires proper citation.

Creative Commons Attribution-NonCommercial-NoDerivs (CC-BY-NC-ND): for non-commercial purposes, lets others distribute and copy the article, and to include in a collective work (such as an anthology), as long as credit the author(s) and provided they do not alter or modify the article.

Contents

- en1 – en2 Computational Techniques for Infectious Diseases and Clinical Research
Ponnuswamy MJ., Krishnamurthy K.
- en3 – en8 Automated Decision Support System for Tuberculosis Digital Images Using Evolutionary Learning Machines
Priya E., Srinivasan S.
- en9 – en13 Predicting Anti HIV Activity of Quinolone Carboxylic Acids – Computation Approach Using Topological Indices
Senbagamalar J., Baskar Babujee J.
- en14 – en26 Comparative Evaluation of Antimicrobial Activity of Selected Three Herbal Plants Extract with Digital Image Processing Technique
Subashini R., Mahesh V., Kavitha A., Geethanjali B., Rakshitha S.U.
- en27 – en36 Musculoskeletal Modeling of Hip Joint and Fracture Analysis for Surgical Planning Using FEA
Ganapathi S., Thoppay Premkumar S., Malaikannu T., Anandan K.
- en37 – en41 Computer Aided Segmentation and Classification of Mass in Mammographic Images using ANFIS
Yuvaraj K., Ragupathy U.S.
- en42 – en51 Comparison of Intelligent Computing Techniques for Classification of Clinical EEG Signals
Najumnissa D., Rangaswamy T.R.
- en52 – en57 A Rapid and Reproducible Report on the Morphological and Functional Characteristics of Spermatozoa Using Digital Image Processing Technique
Pushpa Innocent D.J., Suseela M.R., Priya L.N., Jesuchristopher J.
- en58 – en68 An Image Based Microtiter Plate Reader System for 96-well Format Fluorescence Assays
Durai Arun P., Sankaran K., Muttan S.

Computational Techniques for Infectious Diseases and Clinical Research

Mannar Jawahar Ponnuswamy¹, Kamalanand Krishnamurthy²

¹ Centre for University Industry Collaboration, Anna University, Chennai 600025, India

² Department of Instrumentation Engineering, MIT Campus, Anna University, Chennai 600044, India

The unpredictable nature of infectious diseases has been a source of fear and superstition since early times. The purpose of introducing mathematics in the field of infectious diseases is to understand the dynamics of infections and for analysis [1]. The first mathematical model of an infectious disease was proposed by Daniel Bernoulli, a Swiss Mathematician and Physicist. In 1760, Daniel Bernoulli developed a differential equation model to quantitatively analyze how cowpox inoculation affects the spread of smallpox. Further, Bernoulli used the model to assess the practical advantages of a vaccination program [2, 3].

Over the years, the use of mathematical and computational models for understanding the dynamics of the infection, for analyzing the spread of diseases and for establishing the effectiveness of vaccines, has greatly revolutionized the study of infectious diseases and epidemic outbreaks [4]. The computational techniques for analyzing infectious diseases are diverse and growing rapidly. Some techniques have been newly developed, whereas others have been derived from diverse fields including dynamical systems, stochastic processes, statistical physics, graph theory, statistics, operations research and high-performance computing [5].

Recently, several computational methods such as image processing, numerical methods, optimization, statistics, artificial intelligence etc. have been successfully employed for biomedical analysis and medical diagnostics. Such tools have proved to be valuable for treatment and surgery planning, design of biosensors and development of decision support systems.

The European Journal for Biomedical Informatics (EJBI), being an official journal of the European Federation for Medical Informatics, offers an excellent forum for sharing and understanding of interdisciplinary scientific knowledge between the biomedical researchers and the healthcare industry. Being a multilingual journal, EJBI also ensures the wide reach of information on an international scale.

This special issue of EJBI entitled "Applications of Computational Techniques in Infectious Diseases and Clinical Research" gathers the authors' effort to bring relevant scientific and technological discussion about the applicability of computational methods such as image processing, intelligent computing, finite element methods, etc. in multidisciplinary areas of infectious diseases and clinical research.

This issue comprises eight excellent contributions which depict ideas applied in diverse areas such as intelligent biosensor development, infectious diseases such as HIV and tuber-

culosis, analysis of clinical signals and images, and clinical biomechanics.

Tuberculosis is a highly infectious disease and is a major cause of death in underdeveloped and developing countries. In the paper presented by Priya and Srinivasan, an automated decision support system based on evolutionary extreme learning machines and sputum smear images has been developed for diagnosis of Tuberculosis infection.

In recent years, the spread of HIV/AIDS has become a global problem and is considered to be the most severe health crisis of modern times. In the article submitted by Senbagamalar and Baskar Babujee, the authors have analyzed the anti HIV activity of Quinolone Carboxylic acids using graph theory.

Next, in the research article presented by Subashini et al., the authors have extensively analyzed the antimicrobial effects of the selected herbal plants such as *Solanum xanthocarpum*, *Solanum nigrum* and *Helianthus annuus*, using digital image processing techniques.

In the next paper authored by Ganapathi et al., the authors have used finite element methods for design and analysis of a hip implant model for surgical planning. The authors have further optimized the implant for improving patient safety.

Breast cancer is one of the most common malignancy in women and is a continuing threat worldwide. In the paper presented by Yuvaraj and Ragupathy, a computer aided method for segmentation and classification of mass in mammographic images has been developed using a hybrid neuro-fuzzy system.

In the next article presented by Najumnissa and Rangaswamy, a detailed comparison on the classification performance of intelligent computing techniques such as back propagation networks, adaptive neuro-fuzzy inference system, particle swarm optimization based neural networks and radial basis function neural networks, for classification of normal and abnormal EEG signals, has been performed.

The paper authored by Innocent et al., describes a computer aided semen quantification technique for analyzing the quality of sperm in men. At present, infertility has become a major concern in marital relationships and an automated system for evaluation of sperm quality is highly useful for fast and efficient analysis of infertility in men.

In the final paper of this special issue, presented by Durai Arun et al., the authors have developed an image based microtiter plate reader system for 96-well format fluorescence

assays, using a blue light excitation and a k-means classifier. Very promising results have been obtained and this interesting work appears to be of high clinical importance.

This joint Indo-European effort clearly magnifies the applicability and importance of computational methods in the fields of infectious diseases and clinical research. We are indebted to the Editor-in-Chief, Prof. Dr. Jana Zvárová and the Executive Editor, Dr. Petra Přechková for their valuable support. The Editors would like to thank the Reviewers of this special issue, for their excellent reviews and comments.

References

- [1] Choisy M, Guégan J.-F, Rohani P. Mathematical Modeling of Infectious Diseases Dynamics. Chapter 22. Encyclopedia of Infectious Diseases: Modern Methodologies, by M.Tibayrenc. John Wiley Sons. 2007.
- [2] Bernoulli D. Essai d'une nouvelle analyse de la mortalité causée par la petite vérole et des avantages de l'inoculum pour la prévenir. Mém Math Phys Acad Roy Sci Paris 1760; 1–45.
- [3] Dietz K, Heesterbeek JAP. Daniel Bernoulli's epidemiological model revisited. Mathematical Biosciences 2002; 180: 1–21.
- [4] Hollingsworth TD. Controlling infectious disease outbreaks: Lessons from mathematical modelling. Journal of Public Health Policy 2009; 30(3): 328-341.
- [5] Dimitrov NB, Meyers LA. Mathematical Approaches to Infectious Disease Prediction and Control. Tutorials in Operations Research, INFORMS 2010; 1-25.

Automated Decision Support System for Tuberculosis Digital Images Using Evolutionary Learning Machines

E. Priya¹, S. Srinivasan¹

¹ Department of Instrumentation Engineering, Madras Institute of Technology, Anna University, Chennai

Abstract

Background: Tuberculosis (TB) is a major cause of illness and death in many countries, especially in Asia and Africa. Repeated tests of microscopic examination are needed to be performed for early detection of the disease. Hence there is a need to automate the diagnostic process for improvement in the sensitivity and accuracy of the test.

Objective: To automate the decision support system for tuberculosis digital images using histogram based statistical features and evolutionary based extreme learning machines.

Materials and methods: The sputum smear positive and negative images recorded under standard image acquisition protocol are subjected to histogram based feature extraction technique. Most significant features are selected using student 't' test.

These significant features are further used as input to the differential evolutionary extreme learning machine classifier.

Results: Results demonstrate that the histogram based significant features are able to differentiate TB positive and negative images with a higher specificity and accuracy.

Conclusion: The methodology used in this work seems to be useful for the automated analysis of TB sputum smear images in mass screening disorders such as pulmonary tuberculosis.

Keywords

Tuberculosis, sputum smear, histogram, differential evolution, extreme learning machines

Correspondence to:

S. Srinivasan

Department of Instrumentation Engineering,
Madras Institute of Technology
Address: Anna University, Chennai – 600 044
E-mail: srini@mitindia.edu

EJBI 2013; 9(2):3–8

received: January 9, 2013

accepted: March 25, 2013

published: August 30, 2013

1 Introduction

Tuberculosis (TB) is a communicable disease for which early diagnosis is critical to control the disease. Sputum smear microscopy continues to be the most widely used TB diagnostic method. The microscopy based TB screening method provides significant benefit to a large number of TB burdened communities across the globe [1].

The International Union Against Tuberculosis and Lung Disease recommend at least 100 view fields to be examined per sputum sample. The number of bacilli in these view fields is counted to grade the severity of the disease [2].

Manual screening using microscope is a conventional method employed for TB identification but it is tedious and requires highly trained experts [3]. Besides huge variability in sensitivity, manual screening for bacillus identification is a labor intensive task.

It consumes 40 minutes to 3 hours depending on patient's level of infection and it is needed to analyse 40 to

100 images of one slide. Hence automatic methods for TB identification are highly demanded [3, 4].

Several image analysis techniques have been reported for the automatic identification and classification of sputum smear samples [4, 5, 6]. Image histogram is an important digital image tool that represents the statistical information of the data within an image. The shape of the histogram provides many clues to the characteristics of the image. Different useful features from the histogram describe quantitatively the first and higher order statistical properties of the image. Common features include mean, variance, skewness, kurtosis, energy and entropy [7]. In order to classify the TB images into positive and negative, most significant features are derived from the original data sets. These significant features are used as input to the evolutionary based learning machine for the classification of sputum smear images into TB positive and negative.

Various machine learning techniques have been applied in classifying the TB positive and negative images.

The hybrid approach which takes advantages of both Differential Evolution (DE) and Extreme Learning Machine (ELM) has a more compact network. The DE process is a global searching optimization method used to tune the input weights and hidden layer biases where the output weights are determined by the generalized inverse procedure. The ELM learning algorithm is faster and has good generalization ability. The ELM algorithm overcomes many issues in traditional gradient algorithms such as stopping criterion, learning rate, number of epochs and local minima. On account of these advantages, DE-ELM has been effectively used in the field of medical diagnosis [8, 9].

In this work, histogram based statistical features are extracted from the sputum images. Most significant features are further given as input to the DE-ELM classifier to classify the TB positive and negative images.

2 Methods and Materials

2.1 Image Acquisition

The digital images of TB sputum smears captured using a fluorescence microscope at magnification $20\times$ with a camera in monochrome binning mode are used for this analysis. The digitized sputum smear images ($N = 100$) are subjected to histogram based feature extraction to identify and classify the images into TB positive and negative.

2.2 Histogram Based Statistical Features

The histograms are constructed by quantizing the image into bins. The statistical features such as mean, variance, skewness, kurtosis, energy and entropy are calculated by the probability distribution of intensity levels in the histogram bins. The statistical feature mean represents the brightness of the image. The mean measures the average value of intensity values. The image is bright if mean value is high and dark if it is low. The variance is the second order moment and it shows the contrast of gray level intensities. The low value of the variance indicates low contrast and the high value shows the high contrast of the image [10].

Skewness is a third order moment and it measures the inequality of intensity level distribution about the mean. The negative skewness value indicates a large number of intensity values on the right side of the mean or the tail on the left side is longer than the right side. The positive value indicates a large number of intensity values on the left side of the mean or the tail on right side is longer than the left side. The zero value indicates that the distribution of the intensity values is relatively equal on both sides of the mean [11].

The fourth order moment kurtosis is used to measure the peak distribution of intensity values around the mean. The high value of kurtosis indicates a sharp peak distribution with long and fat tail. The low value of kurtosis indicates a rounded peak distribution with short and thin tail. The kurtosis of normal distribution is three. Kurtosis value is greater than three for the distributions that are more outlier prone than normal distribution. Distributions that are less outlier prone have kurtosis less than three [10].

The energy feature measures the uniformity of intensity level distribution. If the value is high, then the distribution is to a small number of intensity levels. The entropy measures the randomness of the distribution of the coefficients values over the intensity levels. If the value of entropy is high, then the distribution is among more intensity levels in the image and this measurement is the inverse of energy [10].

The mathematical formulations of the statistical features extracted from the histogram are given in Table 1. The n^{th} moment of the normalized gray level histogram is given by:

$$\mu_n = \sum_{l=1}^L (k_l - m)^n p(k_l) \quad (1)$$

where k_l is the gray value of the l^{th} pixel, m is the mean gray value of the pixel, L is the number of distinct gray levels, $p(k_l)$ is the normalized histogram representing the probability density function of the pixel [11, 12, 13].

Table 1: Mathematical formulations of histogram based statistical features.

Features	Formula
Mean	$m = \sum_{l=1}^L k_l p(k_l)$
Variance	$\sigma^2 = \sqrt{\sum_{l=1}^L (k_l - m)^2 p(k_l)}$
Skewness	$H_S = \frac{1}{\sigma^3} \sum_{l=1}^L (k_l - m)^3 p(k_l)$
Kurtosis	$H_K = \frac{1}{\sigma^4} \sum_{l=1}^L (k_l - m)^4 p(k_l) - 3$
Energy	$H_E = \sum_{l=1}^L \{p(k_l)\}^2$
Entropy	$H_N = - \sum_{l=1}^L p(k_l) \log\{p(k_l)\}$

To choose the most significant features, student 't' test is performed over the feature sets for further classification of the sputum smear images. The statistically significant ($p < 0.0001$) features chosen are mean, skewness and kurtosis.

2.3 Differential Evolutionary Extreme Learning Machines

Differential evolution proposed by Storn and Price is a global searching optimization method which obtains more compact network than the original ELM, as they require a large number of hidden units and long time for responding to new input patterns [9]. The network archi-

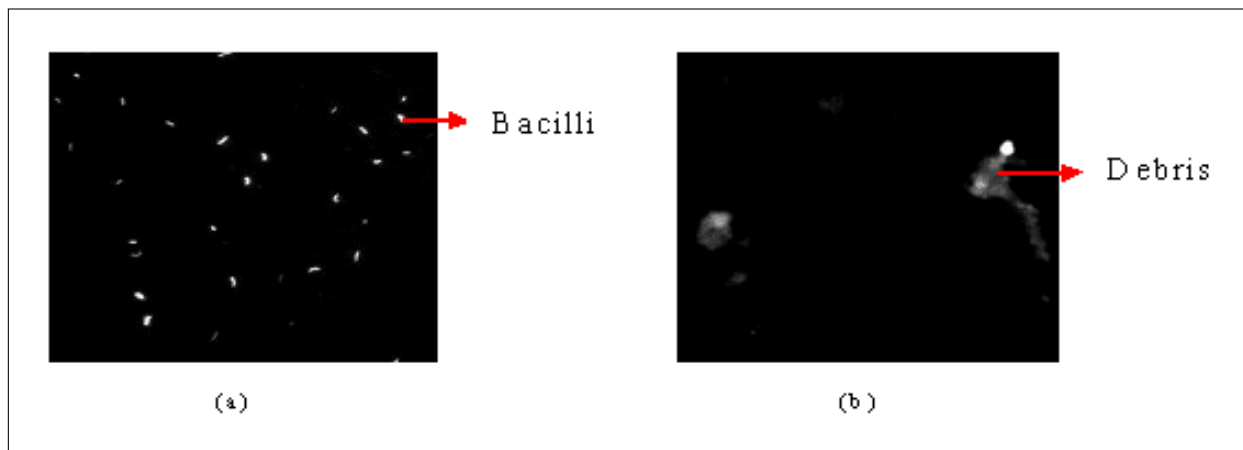


Figure 1: Typical TB (a) positive and (b) negative sputum smear image.

texture comprises of three layers such as input, hidden and output each consisting of one layer and is trained with K hidden neurons to learn N distinct samples. In the ELM algorithm, the network weights w_i and bias b_i are randomly assigned. The hidden layer output matrix, $H = \{h_{ij}\} (i = 1, \dots, N \text{ and } j = 1, \dots, K)$ is then calculated where $h_{ij} = g(w_j \cdot x_i + b_j)$ denotes the output of the j^{th} hidden neuron with respect to the input x_i and $g(x)$ represents the activation function. Finally, the output weight β is computed from the least square solutions $\beta = H^\dagger T$, where H^\dagger is the Moore-Penrose generalized inverse of H and $T = [t_1, \dots, t_N]^T$ is the matrix of desired outputs [8]. The Root Mean Square Error (RMSE) between the test target and the actual target is calculated. The RMSE of testing samples is used as a standard to analyze the testing accuracy, which is affected by the number of hidden neurons and activation function. Classification accuracy increases with decrease in RMSE and reflects the discrepancy between the actual and target values and is evaluated as [14]

$$RMSE = \sqrt{\frac{\sum_{i=1}^N \left\| \sum_{j=1}^K \beta_j g(w_j x_i + b_j) - t_i \right\|_2^2}{N}} \quad (2)$$

The performance of the classifier is tested using sensitivity, specificity and accuracy. Sensitivity is referred to the fraction of positive images correctly classified as positive, specificity is referred to the fraction of negative images correctly classified as negative and accuracy is referred to the ratio of correctly classified images to the total images.

3 Results and Discussion

Typical representative of TB positive and negative smear images are shown in Figures 1 (a) and (b) respectively. TB positive image shows the presence of rod shaped bacilli objects on a dark background. The negative images may contain scanty or absence of bacilli. The spu-

tum smear images considered contain debris, which can be due to poor or nonspecific staining of the smear slides and due to overlapping bacilli. These debris objects do not have uniform morphology. Histogram based statistical features are extracted from these images to extract useful statistical information that aid in differentiating the images into TB positive and negative.

The normalized average and standard deviation values of the histogram based statistical features for TB positive and negative images are shown in Table 2. It is observed that the average values of the features mean, variance, skewness, kurtosis and entropy except energy are found to be high for TB positive images than negative. The mean intensity value of positive images is higher than the negative that represents the brightness of the image. Since the number of bacilli in TB negative images is lower, the brightness is less and image is dark as represented by the mean feature in Table 2.

Table 2: Average and standard deviation values of the histogram based statistical features.

Histogram based statistical features	Average \pm SD	
	TB positive	TB negative
Mean	0.87 ± 0.03	0.83 ± 0.02 *
Variance	0.27 ± 0.19	0.16 ± 0.16
Skewness	0.56 ± 0.17	0.30 ± 0.18 *
Kurtosis	0.32 ± 0.18	0.11 ± 0.15 *
Energy	0.97 ± 0.05	0.97 ± 0.03
Entropy	0.29 ± 0.24	0.17 ± 0.10

* ($p < 0.0001$) highly statistically significant

TB positive images consists of a large number of rod shaped objects, hence the contrast is comparatively higher than negative images. Contrast of TB negative images is lower because of the absence or presence of scanty number of bacilli exhibiting a lower variance value. The positive skewness of both positive and negative indicates the uniformity of background intensity values. Because of the

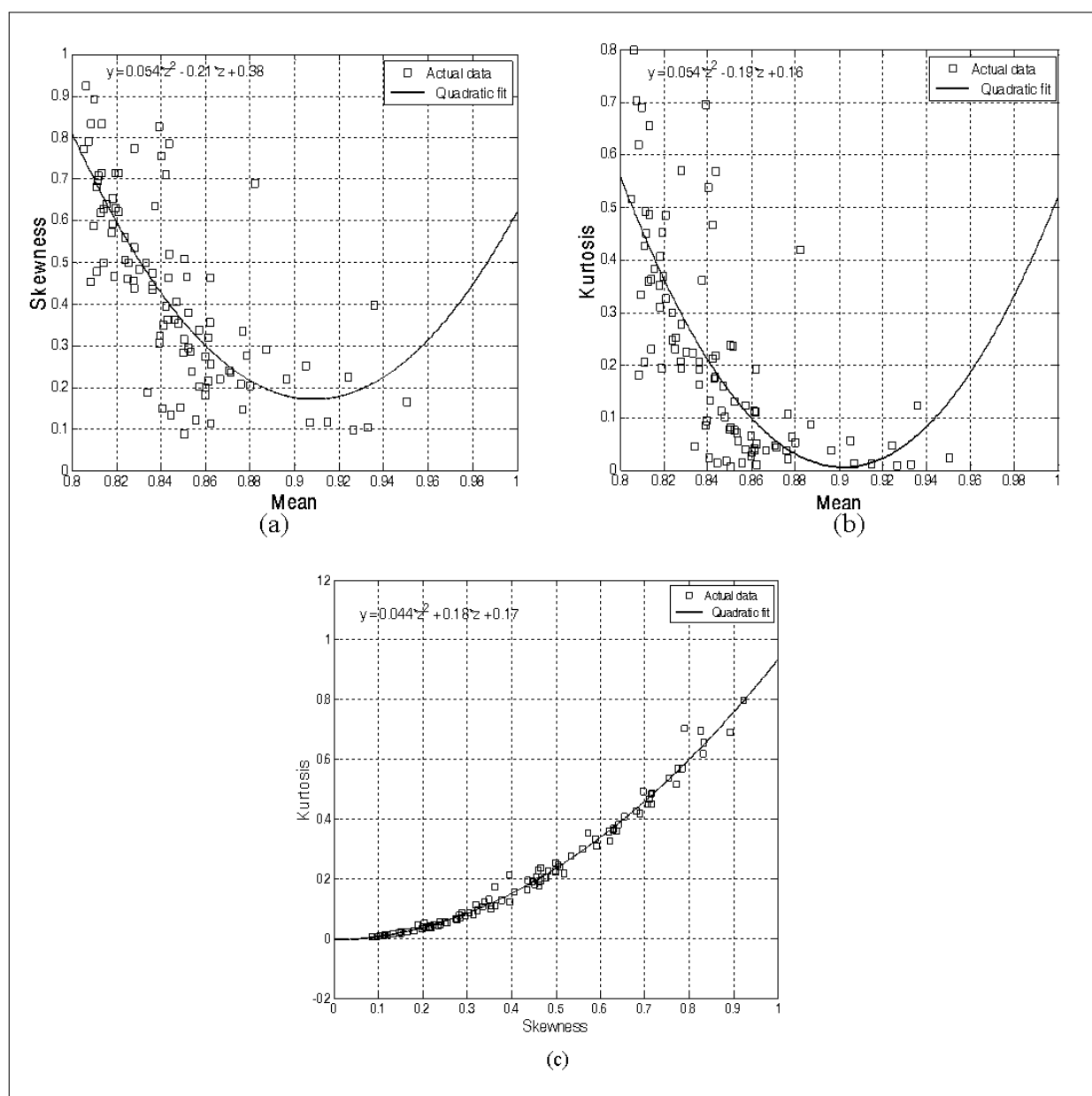


Figure 2: Quadratic fit of (a) skewness (b) kurtosis as a function of mean values (c) kurtosis as a function of skewness value.

presence of numerous foreground objects (bacilli) in positive images, the skewness is higher than negative.

The higher value of kurtosis is due to the sharp change in gray level that arises around the edge of bacilli and smears in the positive images. The energy feature measures an equal value which measures the uniformity of intensity level distribution in both positive and negative images. The entropy is observed to be high for positive images as the distribution is among more intensity levels than negative. To reduce the complexity in classifying the positive and negative images the most significant features are chosen using student 't' test. Table 2 shows the highly statistically significant ($p < 0.0001$) features mean, skewness and kurtosis.

Quadratic fit of skewness and kurtosis as a function of mean values are shown in Figures 2 (a) and (b). The mean

value of TB positive images is 0.87 that differs from that of negative which is about 0.83. The plot in Figure 2 (a) shows the variation of average intensity with respect to the distribution of intensity values for both positive and negative images. It is observed that the two (TB positive and negative) groups centred on the mean value assist in classification of these images. Similarly Figure 2 (b) shows the variation of average intensity with respect to degree of peaked-ness of the distribution.

The quadratic fit of kurtosis as a function of skewness value is shown in Figure 2 (c). It is observed that the skewness value of TB positive images is centered on 0.56 and for negative images it is centered on 0.30. Also, Figure 2 (c) presents the variation in distribution of intensity values with respect to degree of peaked-ness. In order to differentiate the positive and negative images, the

three significant features are further given as input to the DE-ELM classifier.

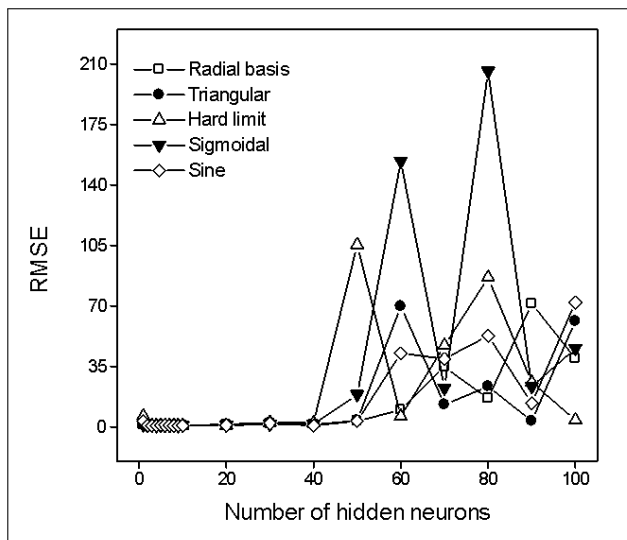


Figure 3: Error plot for varying number of hidden neurons and activation function.

The performance of the classifier is evaluated using RMSE by varying the number of hidden neurons as shown in Figure 3. The evaluation is performed for different activation function such as radial basis, triangular, hard limit,

sigmoidal and sine. The corresponding RMSE values are presented in Table 3.

It is observed from Table 3 that radial basis activation function seems to perform with a lower RMSE value (0.637) for ten numbers of hidden neurons. Hence radial basis activation function is considered for further analysis of the classifier.

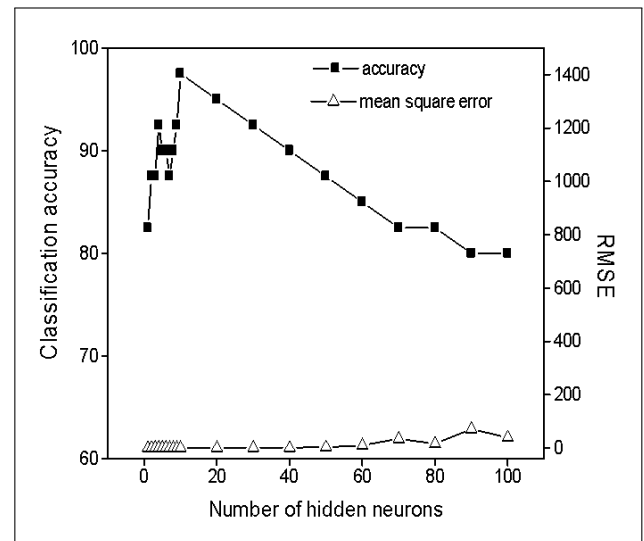


Figure 4: Error plot for varying number of hidden neurons and activation function.

Table 3: RMSE for varying number of hidden neurons and activation function.

No. of hidden neurons	RMSE for different activation function				
	Radial basis	Triangular	Hard limit	Sigmoidal	Sine
1	1.055	3.073	6.252	0.957	3.243
2	0.747	0.816	0.837	0.810	0.771
3	0.806	0.802	0.732	0.785	0.770
4	0.838	0.757	0.717	0.724	0.655
5	0.927	0.750	0.762	0.893	0.723
6	0.715	0.779	0.755	0.833	0.834
7	0.723	0.711	0.732	0.718	0.735
8	0.686	0.675	0.729	0.716	0.706
9	0.651	0.652	0.717	0.694	0.683
10	0.637	0.753	0.687	0.851	0.713
20	1.225	1.368	0.718	0.922	0.881
30	1.831	2.397	2.418	1.479	2.069
40	1.427	0.827	2.305	1.506	0.733
50	3.186	3.637	105.334	18.671	3.297
60	9.800	69.665	6.010	153.675	42.551
70	34.667	12.810	47.046	22.404	39.253
80	16.367	23.439	86.396	205.710	52.618
90	71.383	3.315	25.680	23.258	13.691
100	39.535	61.134	3.892	45.384	71.945

* ($p < 0.0001$) highly statistically significant

The error plot and classification accuracy is shown in Figure 4 for different number of hidden neurons with radial basis function as the activation function. The number of hidden neurons is observed to be ten for the minimum RMSE and maximum classification accuracy.

Table 4: Confusion matrix of the classifier.

Confusion matrix		Predicted class	
		Positive (train/test)	Negative (train/test)
Actual class	Positive (train/test)	28/17	02/03
	Negative (train/test)	00/00	30/20

Table 4 shows the confusion matrix of the classifier, presenting the actual and the predicted classes for both training and testing. Since all the negative images subjected to this methodology are predicted correctly, specificity of both training and testing is observed to be 100%. Except three of the 40% test data remaining are correctly predicted and thus the accuracy is observed to be 92.5% with a training accuracy of 96.7%.

4 Conclusion

Any person with active tuberculosis is capable of infecting on average between 10 and 15 people every year [15]. Therefore, early automated detection of the disease is vital for monitoring, control and for treatment of tuberculosis.

In this work, an attempt has been made to automate the decision support system for tuberculosis digital images using histogram based statistical features and evolutionary based extreme learning machines. Results demonstrate that the significant histogram features are able to differentiate TB positive and negative images with a higher specificity and accuracy. Thus the methodology seems to be useful for the automated analysis of TB sputum smear images in mass screening disorders such as pulmonary tuberculosis.

Acknowledgements

The authors acknowledge Tania S. Douglas of Medical Imaging Research Unit, University of Cape Town, South Africa for the sputum smear images.

References

- [1] Chang J., Arbelaez P., Switz N., Reber C., Tapley A., Davis L., Cattamanchi A., Fletcher D., Malik J. Automated tuberculosis diagnosis using fluorescence images from a mobile microscope. Ayache N. et al. Editors. MICCAI 2012, Part III, LNCS, 2012; 7512: 345-352.
- [2] Laszlo A. Technical Guide, Sputum examination for tuberculosis by direct microscopy in low income countries, Fifth edition 2000, International Union Against Tuberculosis and Lung Disease, Paris, France.
- [3] Zhai Y., Liu Y., Zhou D., Liu S. Automatic identification of mycobacterium tuberculosis from ZN-stained sputum smear: Algorithm and system design, in Proceedings of the IEEE International Conference on Robotics and Biomimetics, 2010, Tianjin, China, 41-46.
- [4] Sotaquirra M., Rueda L., Narvaez R. Detection and quantification of bacilli and clusters present in sputum smear samples: a novel algorithm for pulmonary tuberculosis diagnosis, in Proceedings of the International Conference on Digital Image Processing, 2009, Bangkok, Thailand, 117-121.
- [5] Khutlang R., Krishnan S., Whitelaw A., Douglas T.S. Automated detection of tuberculosis in Ziehl-Neelsen-stained sputum smears using two one-class classifiers. J Microsc. 2010; 237: 96-102.
- [6] Forero M.G., Cristobal G., Desco M. Automatic identification of mycobacterium tuberculosis by Gaussian mixture models. J Microsc. 2006; 223:120-132.
- [7] Srinivasan G.N., Shobha G. Statistical Texture Analysis, in Proceedings of World Academy of Science, Engineering and Technology, 2008; 36: 1264-1269.
- [8] Huynh H.T., Won Y. Hematocrit estimation from compact single hidden layer feedforward neural networks trained by evolutionary algorithm, IEEE Congress on Evolutionary Computation, 2008, Hong Kong, 2962-2966.
- [9] Yusoff I.A., Isa N.A.M., Othman N.H., Sulaiman S.N., Jusman Y. Performance of neural network architectures: Cascaded MLP versus extreme learning machine on cervical cell image classification. In Proceedings of 10th International Conference on Information Science, Signal Processing and their Applications, 2010, Kuala Lumpur, Malaysia, 308-311.
- [10] Seetha M., Malini Devi G., Sunitha K.V.N. Performance assessment of feature based image retrieval using neural networks, International Journal of Systems , Algorithms Applications, 2012, 2: 4-8.
- [11] Shi X., Cheng H.D., Hu L. Mass detection and classification in breast ultrasound images using fuzzy SVM, in Proceedings of the Joint Conference on Information Science, 2006.
- [12] Nurhayati O.D., Widodo T.S., Susanto A. Tjokronagoro M. First order statistical feature for breast cancer detection using thermal images, World Academy of Science, Engineering and Technology, 2010, 46: 424-426.
- [13] Younus A.M., Widodo A., Yang B.S. Evaluation of thermography image data for machine fault diagnosis, Nondestr Test Eval. 2010; 25: 231-247.
- [14] Zhu Q.Y., Qin A.K., Suganthan P.N., Huang G.B., Evolutionary extreme learning machine, Pattern Recognit. 2005, 38: 1759-1763.
- [15] Tuberculosis Fact. World Health Organization (WHO), Geneva, 2010, Sheet No. 104.

Predicting Anti HIV Activity of Quinolone Carboxylic Acids – Computation Approach Using Topological Indices

J. Senbagamalar¹, J. Baskar Babujee¹

¹ Department of Mathematics, Anna University, India

Abstract

Background: Quantitative structure–activity relationships (QSAR) are a major factor in contemporary drug designing. Thus, it is quite clear that a large number of users of QSAR are located in industrial research units.

Objectives: A Topological Index is a numeric quantity that is mathematically derived in a direct and unambiguous manner from the structural graph of a molecule. In structure–activity relationship studies, molecular topology quantifies chemical structure into characteristic numerical descriptors. All structural formulas of chemical compounds are molecular graphs where vertices represent the set of atoms and edges represent chemical bonds. The construction and investigation of topological indices that could be used to describe molecular structures is one of the important directions of mathematical chemistry. Topological descriptors developed for predicting physicochemical properties and biological activities of chemical substances can be used for drug design.

Materials and Methods: A number of successful QSAR studies were made based on the Wiener index, Terminal Wiener Index and Platt Number. These indices are derived from matrices, like distance matrix and adjacency matrix which represents a molecular graph. Zagreb Index is based on degree connectivity indices.

Results and Conclusion: In this paper we analyze, Quantitative structure activity relationship studies were performed on anti-HIV activity of Quinolone carboxylic acid for Wiener Index, Terminal Wiener Index, Platt Number and Zagreb Index.

Keywords

Graph, vertices, wiener index, degree, atom, quinolone carboxylic acid

Correspondence to:

J. Senbagamalar

Department of Mathematics, Anna University

Address: Chennai – 600 025, India

E-mail: senbagamalar2005@yahoo.com

EJBI 2013; 9(2):9–13

received: January 9, 2013

accepted: March 18, 2013

published: August 30, 2013

1 Introduction

The discovery of the human immunodeficiency virus (HIV) as the causative agent of AIDS has led to enormous efforts to unravel the basic action of the virus at a molecular level. From this effort, a variety of targets for potential intervention of HIV multiplication have been identified. Anti-HIV therapy, today, is in need of new drugs, which are less toxic, active against the drug resistant mutants selected by current therapies in the viral replicative cycle.

In the last decade, synthetic chemists have done tremendous research efforts for the development of newer anti-HIV agents [3]. Structure-based design, spurred by the significant pitfalls of the traditional method and the rapid advances in molecular-structure determination and computational resources, has now been accepted as a rational approach for the generation of new pharmaceuticals. The successful implementation of quantitative struc-

ture–property/activity relationship (QSPR/QSAR) certainly decreases the number of compounds synthesized, by making it possible to select most promising compounds. Non empirical parameters of chemical structure derived from graph theoretic formalism are being used more frequently by many researchers in QSAR studies pertaining to molecular design, pharmaceutical drug-design, and environmental hazard assessment of chemicals. In chemistry, a graph represents the topology of a molecule in the sense that it depicts the pattern of connectedness of atoms in the molecule, being at the same time, independent of such metric aspects of molecular structure as equilibrium distance between nuclei, bond angles, etc. When a single number represents a graph invariant, it is known as topological index or topological descriptor. These indices are derived from matrices, like distance matrix and adjacency matrix, which represent a molecular graph. Though numerous topological descriptors have been reported in the literature but only handful of them has been successfully

employed for structure–activity relationship studies. Notable amongst these are Wiener index, Terminal Wiener Index, Zagreb index and Platt Number.

In the present investigation, relationship of Wiener index, Terminal Wiener Index, Zagreb index and Platt Number for anti-HIV activity of Quinolone Carboxylic Acid has been investigated and suitable models have been developed for prediction of anti-HIV activity.

1.1 Definition

The Wiener index [2] is a distance-based graph invariant used as one of the structure descriptors for predicting physicochemical properties of organic compounds. The Wiener index was introduced by the chemist H. Wiener about 60 years ago to demonstrate correlations between physicochemical properties of organic compounds and the topological structure of their molecular graphs. This concept has been one of the most widely used descriptors in relating a chemical compound's property to its molecular graph.

The Wiener index $W(G)$ of a graph G is defined as the sum of the half of the distances between every pair of vertices of G .

$$W(G) = \frac{1}{2} \sum_{i=1}^n \sum_{j=1}^n d(v_i, v_j) \quad (1)$$

Where $d(v_i, v_j)$ is the number of edges in a shortest path connecting the vertices v_i , and v_j . Wiener index of a complete graph K_n is

$$W(K_n) = \frac{n^2 - n}{2} \quad (2)$$

and path graph P_n ,

$$W(P_n) = \frac{n^3 - n}{6}. \quad (3)$$

Among all the trees on n vertices, the star $K_{1,n-1}$ has the lowest Wiener number and the path P_n has the largest Wiener number and hence

$$W(K_{1,n-1}) \leq W(T) \leq W(P_n). \quad (4)$$

1.2 Definition

The Terminal distance matrix [4] or reduced distance matrix of trees was introduced by Gutman, B. Furtula, and M. Petrovic. If an n -vertex graph G has k pendent vertices (vertices of degree one), labeled $v_1, v_2, v_3, \dots, v_k$, then its terminal distance matrix is the square matrix of order k whose (i, j) - entry is $d(v_i, v_j | G)$. The Terminal Wiener index $TW(G)$ of a graph G is the sum of the distances between all pairs of pendent vertices.

$$TW(G) = \sum_{1 \leq i < j \leq k} d(v_i, v_j | G) \quad (5)$$

where $d(v_i, v_j | G)$ is the distance between pair of pendent vertices in a graph G . Consider a graph G , vertices having degree one is called pendent vertices or terminal vertices and vertices having more than one degree are called interior vertices.

1.3 Definition

The Zagreb group indexes of a graph G denoted by $M_1(G)$ (first Zagreb index) [1] and $M_2(G)$ (second Zagreb index) are defined as

$$M_1(G) = \sum_{j=1}^N D_j^2 \quad (6)$$

$$M_2(G) = \sum_{i,j} D_i D_j \quad (7)$$

where D_j stands for the degree of a vertex j . The sum in (6) is over all vertices of G , while the sum in (7) is over all edges of G .

1.4 Definition

Platt was also interested in devising a scheme for predicting the physical parameters (molar refractions, molar volumes, boiling points, heats of formation, heats of vaporization) of alkanes. He introduced an index $F(G)$, which is equal to the total sum of degrees of edges in a graph. The degree of an edge e , $D(e)$ is the number of the adjacency edges.

$$F(G) = \sum_{i=1}^M D(e_i) \quad (8)$$

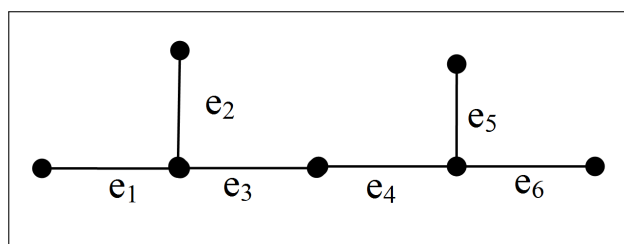


Figure 1: The Graph G .

$$\begin{aligned} F(G) &= D(e_1) + D(e_2) + D(e_3) + D(e_4) + D(e_5) + D(e_6) \\ F(G) &= 2 + 2 + 3 + 3 + 2 + 2 \\ F(G) &= 14 \end{aligned} \quad (9)$$

The calculation of Wiener index, Terminal Wiener Index for three isomers of eight-membered molecule (heptylamine) has been exemplified in Figure 2.

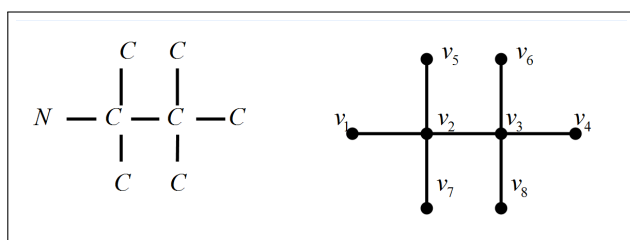


Figure 2: The chemical compound heptylamine is isomorphic to 1,4 biregular-caterpillar graph.

1.5 Chemical Distance Matrices

In the above Figure 2, the chemical compound heptylamine is isomorphic to the corresponding graph 1,4 biregular-caterpillar. In the graph, total number of vertices is eight and number of pendent vertices is six. We calculate the Wiener Index and Terminal Wiener Index of 1,4 biregular graph and tabulated below.

Table 1: Calculation of Wiener Index of 1, 4 bi regular caterpillar graph.

	1	2	3	4	5	6	7	8	$W(G)$
1	0	1	2	3	2	3	2	3	16
2	1	0	1	2	1	2	1	2	10
3	2	1	0	1	2	1	2	1	10
4	3	2	1	0	3	2	3	2	16
5	2	1	2	3	0	3	2	3	16
6	3	2	1	2	3	0	3	0	16
7	2	1	2	3	2	3	0	3	16
8	3	2	1	2	3	2	3	0	16

Table 2: Calculation of Wiener Index and Terminal Wiener Index of 1,4 bi regular caterpillar graph.

	1	2	3	4	5	6	$TW(G)$
1	0	3	2	3	2	3	13
2	3	0	3	2	3	2	13
3	2	3	0	3	2	3	13
4	3	2	3	0	3	2	13
5	2	3	2	3	0	3	13
6	3	2	3	2	3	0	13

Using the Table 1, The Wiener Index for 1,4 bi regular-caterpillar graph is

$$W(G) = \frac{16 + 10 + 10 + 16 + 16 + 16 + 16 + 16}{2} = \frac{116}{2} = 58. \quad (10)$$

Using the Table 2, The Terminal Wiener Index for 1,4 bi regular-caterpillar graph is

$$TW(G) = \frac{13 + 13 + 13 + 13 + 13 + 13}{2} = \frac{78}{2} = 39. \quad (11)$$

2 Results

In this paper we analyse Wiener index, Terminal Wiener Index, Zagreb index and Platt number for anti-HIV activity of Quinolone Carboxylic Acid [5].

We attach the functional group in the basic structures of quinolone carboxylic acid and calculate the values of Wiener Index, Terminal Wiener Index, Zagreb Index and Platt Number.

3 Discussion and Conclusion

We have fixed the active and inactive range values for the compounds as per the reference [3] where eccentric conductivity topochemical index, molecular conductivity topochemical index and Balaban's mean square distance topochemmmmmical index are discussed. In our paper we have analyzed Wiener index $W(G)$, Terminal wiener index $TW(G)$, Zagreb Index $Z(G)$ and Platt Number $F(G)$. Models based on Wiener Index, above the range 2049, quinolone carboxylic acid is active. Out of 46 compounds 38 compounds are inactive. But for the Terminal Wiener Index, the value depends on the pendent vertices hence quinolone carboxylic acid is in transitional range. In the case of Zagreb Index, below the range of 152 the quinolone carboxylic acid is inactive. In case of Platt Number above the range 96 the quinolone carboxylic acid is active.

From the Figure 4, high predictability of the models derived from Wiener Index can provide valuable leads for development of anti HIV agents. Moreover high discriminating amalgamated of Wiener Index with low degeneracy of Platt Number and Zagreb Index offers a vast potential for its use in structure-activity / property studies.

References

- [1] Baskar Babujee J., Senbagamalar J.: Wiener Index of Graphs using Degree Sequence Journal of Applied Mathematical Sciences, Vol. 6, no. 88, 4387 – 4395, 2012.
- [2] Dobrynin, R. Entringer and I. Gutman, Wiener index of trees: Theory and applications, Acta Appl. Math. 66 (2001) 211–249.
- [3] Harish Dureja and Anil Kumar Madan “ Predicting Anti-HIV Activity of Dimethylaminopyridin – 2-ones: Computational Approach using Topochemical Descriptors” Chem Biol. Drug Des. 2009; 73: 258 -270.
- [4] Ivan Gutman, Boris Furtula, Miroslav Petrovic “ Terminal Wiener Index” – Journal of Mathematical Chemistry 2009, 46 (2) 522-531.
- [5] Monika Gupta and Anil Kumar Madan “ Diverse Models for the Prediction of HIV Integrase Inhibitory Activity of Substituted Quinolone Carboxylic Acids” Arch. Pharm Chem. Life Sci. 2012, 000, 1 -12.

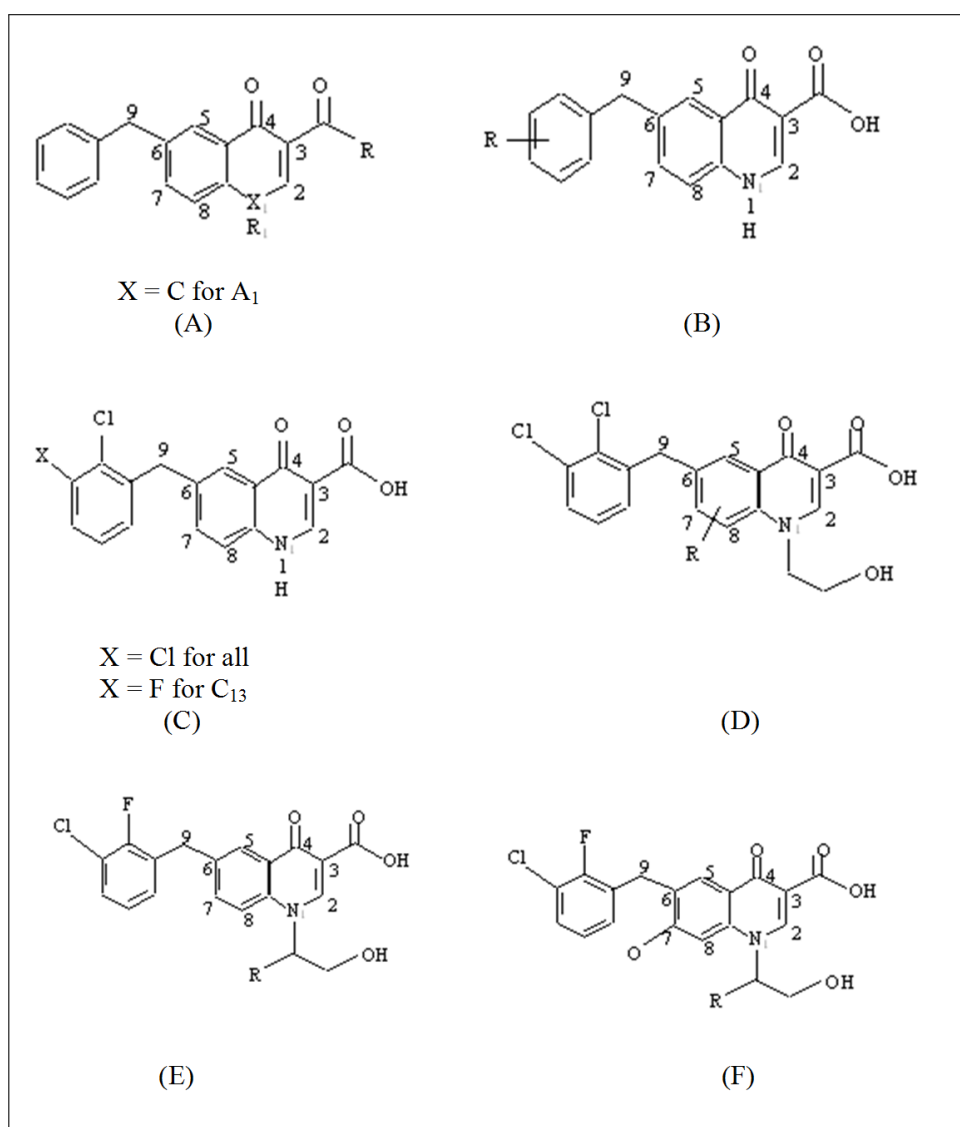


Figure 3: Basic structures and arbitrary atom numbering scheme for the quinolone carboxylic acid.

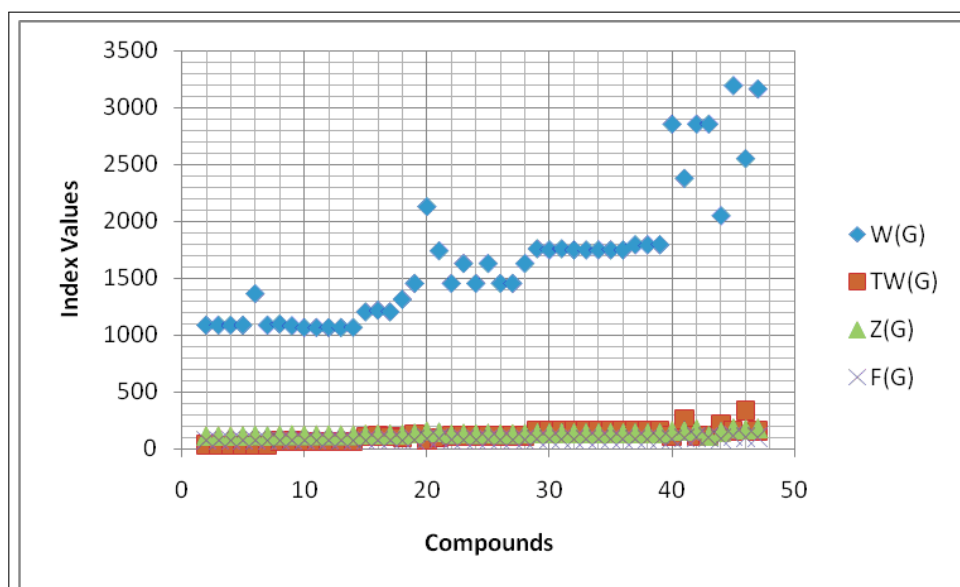
Figure 4: Graphically significant values of $W(G)$, $TW(G)$, $F(G)$ and $Z(G)$.

Table 3: Calculation of Wiener Index, Terminal Wiener Index, Zagreb Index and Platt Number for HIV integrase inhibitory activity.

Compound Number	R/R ₁ (Functional group)	W(G)	TW(G)	M ₁ (G)	F(G)	HIV integrase inhibitory activity		
						W(G)	M ₁ (G)	F(G)
A ₁	–COCOOH	1088	34	115	72	–	–	–
A ₂	–COCOOH / –CH ₃	1088	31	115	74	–	–	–
A ₃	–OH	1088	31	115	72	–	–	–
A ₄	–OH / –CH ₃	1088	31	115	72	–	–	–
A ₅	–OEt	1364	31	120	76	–	–	–
A ₆	NH ₂	1088	31	115	72	–	–	–
B ₁	3 –Cl	1097	70	122	72	–	–	–
B ₂	2 –Cl	1082	66	122	72	–	–	–
B ₃	1 –Cl	1067	62	122	72	–	–	–
B ₄	1 –F	1067	62	122	72	–	–	–
B ₅	1 –Me	1067	62	122	72	–	–	–
B ₆	1 –OMe	1067	62	122	72	–	–	–
B ₇	1 –CF ₃	1067	62	122	72	–	–	–
B ₈	1,4 –Cl ₂	1205	108	128	76	–	–	–
B ₉	2,4 –Cl ₂	1219	112	128	76	–	–	–
B ₁₀	1,2 –Cl ₂	1205	106	128	76	–	–	–
C ₁	–Me	1315	94	128	76	–	–	–
C ₂	–Et	1455	129	138	78	–	–	–
C ₃	–Pr	2129	72	156	91	–	+	–
C ₄	–Bu	1741	94	146	88	–	–	–
C ₅	CH ₂ CO ₂ H	1455	111	132	78	–	–	–
C ₆	CH ₂ CH ₂ CO ₂ H	1630	116	136	80	–	–	–
C ₇	CH ₂ CONH ₂	1455	111	132	78	–	–	–
C ₈	(CH ₂) ₂ CONH ₂	1630	116	136	80	–	–	–
C ₉	(CH ₂) ₂ NH ₂	1455	111	132	78	–	–	–
C ₁₀	(CH ₂) ₂ OH	1455	111	132	78	–	–	–
C ₁₁	(CH ₂) ₃ OH	1630	116	136	80	–	–	–
D ₁	8 –F	1759	160	142	84	–	–	–
D ₂	5 –F	1749	155	142	84	–	–	–
D ₃	9 –F	1759	160	142	84	–	–	–
D ₄	5 –OMe	1749	160	142	84	–	–	–
D ₅	5 –Cl	1749	160	142	84	–	–	–
D ₆	5 –Me	1749	160	142	84	–	–	–
D ₇	5 –CF ₃	1749	160	142	84	–	–	–
D ₈	5 –CN	1749	160	142	84	–	–	–
E ₁	–H	1794	156	142	86	–	–	–
E ₂	–Me	1794	156	142	86	–	–	–
E ₃	–Et	1794	156	142	86	–	–	–
E ₄	–Pr	2854	115	160	86	+	+	–
E ₅	iBu	2378	259	160	96	+	+	+
E ₆	Cyclohexyl	2854	115	174	100	+	+	+
E ₇	Ph	2854	115	116	100	+	–	+
F ₁	5 –OMe	2049	211	152	90	+	+	–
F ₂	–Pr	3192	160	180	116	+	+	+
F ₃	iBu	2551	338	170	100	+	+	+
F ₄	Cyclohexyl	3162	160	180	104	+	+	+

+, active compound; – inactive compound

Comparative Evaluation of Antimicrobial Activity of Selected Three Herbal Plants Extract with Digital Image Processing Technique

Rajakannu Subashini¹, Veezhinathan Mahesh¹, Anandan Kavitha¹, Balasubramaniam Geethanjali¹, Sritharan Umamaheshwari Rakshitha¹

¹ Department of Biomedical Engineering, SSN College of Engineering

Abstract

Background and Objectives: The development in the technology have witnessed that there is a revival of interest in drug discovery from medicinal plants for treatment of the most destructive diseases. Our investigation characterizes the usage of digital image processing techniques in Matlab to process and analyze the antimicrobial effects of the selected herbal plants.

Methods: The first stage of our investigation involves the extraction of components with methanol from the selected three herbal plants- *Solanum xanthocarpum*, *Solanum nigrum* and *Helianthus annuus* by using soxhlet apparatus. These plant extracts were assayed for antimicrobial activity against 4 different bacterial and fungal species using disk diffusion method.

Results: Notable cell growth inhibitions were observed from the selected microbes. *Solanum xanthocarpum* exhibits better antibacterial properties on comparison to other two extracts.

Solanum nigrum and *Helianthus annuus* exhibit better antifungal properties by being sensitive factor towards fungal medium. The obtained images were processed using color coding techniques to determine the activity of the extract by isolating the region of inhibition area. The region of inhibition was measured using matlab code and tabulation was compiled to compare the manually measured distances to the automated measurements.

Conclusions: The results provided evidence that the studied plant extracts might indeed be potential sources of natural antimicrobial agents and the introduction of an evaluation technique using image processing was shown to be suitable for the purpose of accurate measurements of zone of inhibition.

Keywords

Solanum xanthocarpum, *Solanum nigrum*, *Helianthus annuus*, image processing, antimicrobial activity

Correspondence to:

Mahesh Veezhinathan
Department of Biomedical Engineering
SSN College of Engineering, Kalavakkam
Address: Chennai - 603110
E-mail: maheshv@ssn.edu.in

EJBI 2013; 9(2):14-26

received: January 13, 2013

accepted: March 25, 2013

published: August 30, 2013

1 Introduction

The medicinal plants are the ones whose parts like leaves, seeds, stem, roots, fruits and foliage are used in the preparation of varied extracts, infusions, decoctions and powders in different compositions which are used in the treatment of different diseases of humans, plants and animals and they cause comparatively less side effects and activity of the herbal extracts are considerably high. The use of different parts of several medicinal parts to cure specific ailments has been in vogue from ancient times [1].

Solanum xanthocarpum is a perennial, thorny, herbaceous weeded plant with bright green leaves and zigzag

stem, mostly found in arid region. It is commonly known as yellow-berried night shade and also called as Kandankathri in Tamil. It has been widely used in traditional medicine in India and other countries to cure liver disorders, inflammatory conditions, dysmenorrhea, fever, diarrhea, eye diseases, hydrophobia, chronic skin ailments namely psoriasis and ringworm. Crude plant extract is beneficial in bronchial asthma and non-specific cough, influenza, painful and difficult urination, bladder stones and rheumatism [2].

Solanum nigrum commonly known as "Black night shade" belongs to solanaceae family. It is called as Manathakkali in Tamil. It shows medicinal properties like an-

timicrobial, anti-oxidant, cytotoxic properties, antiulcerogenic, and hepatoprotective activity. It is an African pediatric plant utilized for several ailments that are responsible for infant mortality especially feverish convulsions, eye diseases, hydrophobia and chronic skin ailments. It is a potential herbal alternative as anti-cancer agent [3].

Helianthus annuus is an important oilseed crop worldwide and commonly called as sunflower. Sunflower seeds are a good source of protein and Vitamins D, E, K, and B. Studies have shown that seeds can prevent invasion of cancer and many more harmful diseases. The Seeds are used as diuretic and expectorant and also used for cough, throat and lung infections. It is a folk remedy for blindness, bronchitis, carbuncles, colic, diarrhea, dysentery, dysuria, eyes, fever, inflammation, laryngitis, menorrhagia, pleuritis, rheumatism, scorpion stings, snakebite, splenitis, urogenital ailments and wounds. The flowering head and seeds are febrifuge, nutritive and stomachic. A thick decoction of the roots is used as a warm wash on rheumatic aches and pains [4].

Studies have shown that *Solanum xanthocarpum*, *Solanum nigrum* and *Helianthus annuus* display antimicrobial activity, antioxidant and anti-tumor effect respectively [5, 6, 7]. This reveals pharmaceutically useful phytochemicals enriched in these herbal plants and also suggests that the extraction of active compounds from those plants would be useful to destroy pathogenic microorganisms. The present study has evaluated the antimicrobial activity of methanolic extract of *Solanum xanthocarpum*, *Solanum nigrum* and *Helianthus annuus* on pathological strains. The digital image processing technology and Mat lab tool were used to measure the zone of inhibition and was compared with manually measured distances."

Various image processing routines can be carried out to measure the zone of inhibition and compare with manually measured distances. Digital image processing uses computer algorithms to perform image processing on digital color images. Digital image processing allows a much wider range of algorithms to be applied to the input data and can avoid commonly occurring problems such as the build-up of noise and signal distortion during processing. The output of image processing may be either an image or a set of characteristics or parameters related to the image, which is commonly referred to as extraction of features. Most image-processing techniques involve treating the image as a two-dimensional signal and applying standard signal-processing techniques to it [8].

The application of digital image processing and Mat lab tool for the automation of inhibition zone calculation would give accurate data in the screening of antimicrobial property of herbal plants.

The objective of this study was to evaluate the potential of plant extracts on standard microorganism strains and the obtained results was compared with automated values from digital image processing technique.

2 Materials and Methods

2.1 Collection of Plants and Identification

Seeds of *Solanum xanthocarpum*, *Solanum nigrum* and *Helianthus annuus* were collected from Anna medicinal farm, Chennai. The plants were identified and authenticated by Lifetech Research Centre, Chennai. The seeds were sorted, cleaned and air dried at room temperature for two weeks and powdered.

2.2 Preparation of plant extracts

2.2.1 Soxhlet Extraction

Solid material containing 50g of the finely powdered plant parts- air dried seeds in the case of *Helianthus annuus* and dried fruits in case of *Solanum xanthocarpum* and *Solanum nigrum* was placed in thick filter paper in thimble. The Soxhlet extractor was placed over a flask containing the extraction solvent. The solvent used in this process was methanol. It is then equipped with a condenser. The solvent was heated to reflux. The solvent vapor travels up a distillation arm and floods into the thimble which contains the powdered seeds. The condenser, which occupies the top portion of the setup, ensures that solvent vapor cools, and drips back down into the chamber housing the solid material. The thimble containing the solid material slowly fills with warm solvent. Some of the desired compound will then dissolve in the warm methanol [10]. When the Soxhlet chamber was almost full, the chamber was automatically emptied by a siphon side arm, with the methanol running back down to the distillation flask below. This cycle was repeated for 3 times to get the purified extract. The purified extract was air dried and then weighed to measure the amount of extract obtained from the soxhlet apparatus. The dried extract is then mixed with DMSO, a universal solvent. The quantity of DMSO is approximately equal to one half the total quantity of the extract. This mixture is stored in a air tight storage container and then used for further procedures.

2.3 Antimicrobial Studies

2.3.1 Assay of Antibacterial Activity

The bacterial clinical isolates (*Bacillus subtilis*, *Staphylococcus aureus*, *Salmonella typhi* and *Vibrio cholera*) were obtained from Lifetech Research Centre, Chennai.

2.3.2 Preparation of Active Bacterial Suspension

Nutrient broth was made up to 100ml (1.95g in 100ml of distilled water) and was transferred to four different boiling tubes and they were kept for sterilization for

30 minutes in autoclave. This broth was cooled. Active cultures for experiments were prepared by transferring a loopful of stock culture to 25ml of nutrient broth and incubating aerobically at 37°C for 24 hours for bacterial proliferation [11].

2.3.3 Determination of Antibacterial Activity of Herbal Plant Extracts

Muller Hinton agar solid media was used for culturing of bacteria. Agar diffusion assay was carried out to check the antibacterial activity. Muller Hinton agar (6g) was mixed with 300 ml of distilled water along with Agar Agar type1 (3.75g). The medium was sterilized in autoclave at 121°C for 30 minutes and then allowed to cool but not solidify. They were transferred to twelve different sterile petri dishes and the medium was left in the laminar air flow chamber for 30-60 min. After solidification 20 µl of the fungal cultures were inoculated to the Petri plates and incubated at 30°C. Freshly prepared sterilized cotton was used to swab the developed bacterial culture onto the solidified medium. Whatman No 3 filter paper discs were impregnated with 20 µl of different concentration of plant extract, kept onto the petri plate and incubated at 37°C for 24 hours. The antifungal activity was assayed by measuring the zone of inhibition for the respective plant extract and it was compared with standard antibiotic. Muller Hinton agar plates without adding cultures were used as control [12].

2.3.4 Assay of Antifungal Activity

The fungal clinical isolates (*Rhizopus* species, *Aspergillus fumigatus*, *Fusarium* and *Candida albicans*) were obtained from Lifetech Research Centre, Chennai.

2.3.5 Preparation of Working Fungal Cultures

Potato dextrose broth was prepared by dissolving Potato dextrose agar (3.9g) in 300ml of distilled water and was filtered and the filtrate was transferred to four different boiling tubes and they were sterilized in autoclave at 121°C for 30 minutes. This broth was cooled. Loop full of fungal culture was transferred to the broth and incubating aerobically at 37°C for 24 hours for fungal proliferation [13].

2.3.6 Preparation of Medium

Potato dextrose agar (3.9g) was mixed with 300 ml of distilled water along with Agar Agar type1 (3.75g). It was then sterilized in autoclave for 30 minutes and then allowed to cool but not solidify. Then they were transferred to twelve different sterile petri dishes and the medium was left in the laminar air flow chamber for 30-60 min. After solidification 20 µl of the fungal cultures were inoculated to the Petri plates and incubated at 30°C. Freshly prepared sterilized cotton swabs were used to swab the de-

veloped fungal culture onto the solidified medium. Then the filter paper disks immersed in the extract which was serial diluted (sample 1g/100ml of solvent was prepared [10]).

Five test tubes with 0.5ml of methanol were taken. 0.5ml of the prepared extract was dissolved in the test tube numbered one and 0.5ml of extract was taken and dissolved in test tube numbered two and the process continues till the test tube numbered five). Hence five different serial dilutions were used. Then they were kept onto the petriplate and observed zone of inhibition for 24-48 hours. The antifungal activity was assayed by measuring the zone of inhibition for the respective plant extract [14]. Potato dextrose agar plates without adding cultures were used as control.

2.4 Digital Image Processing

The images obtained after the antimicrobial effects were processed in Mat lab using digital image processing techniques to differentiate the region of inhibition from the surrounding areas which were prone to bacterial growth. The region of inhibition was around the disc of filter paper immersed in varying concentrations of extracts. This region is represented with dark blue color and the remaining areas with shades of orange and yellow. To measure the region of inhibition from the zoomed picture and to compare the obtained automated values to that of the values that were measured manually.

2.5 Comparative Evaluation of Antimicrobial Images Using Digital Image Processing

In a bitmap, colors were coded on three bytes representing their decomposition on the three primary colors. Colors were interpreted as vectors in a three dimension space where each axis stands for one of the primary colors. The difference between two colors could be quantified by computing the geometric distance between the vectors representing those two colors.

However if there is a very blurry source it should be passed through a sharpness filter first. Each pixel could be compared with its second or third nearest neighbors on the right and on the bottom instead of the nearest neighbors. The edges will be thicker but also more exact depending on the source image's sharpness. There was another way to make edge detection with matrix convolution.

The quality of the results depends on the sharpness of the source image. If the source image was very sharp edged, the result will reach perfection. The other immediate application of pixel comparison was color extraction. Instead of comparing each pixel with its neighbors, we were going to compare it with a given color C1. This algorithm will try to detect all the objects in the image that were colored with C1.

Table 1: Antibacterial activity of *Solanum xanthocarpum*, *Solanum nigrum* and *Helianthus annuus*.

Bacterial species	Zone of Inhibition (cm)		
	<i>Solanum xanthocarpum</i>	<i>Solanum nigrum</i>	<i>Helianthus annuus</i>
<i>Salmonella typhi</i>	0.11	0.6	1
<i>Bacillus subtilis</i>	0.4	0.5	0.5
<i>Staphylococcus aureus</i>	0.5	0.8	0.7
<i>Vibrio cholera</i>	0.9	0.7	0.6

Table 2: Antifungal activity of *Solanum xanthocarpum*.

Fungal species	Zone of Inhibition (cm)				
	0.5 ml	0.25 ml	0.125 ml	0.0625 ml	0.3125 ml
<i>Fusarium</i>	0.8	0.6	0.5	0.3	0.3
<i>Rhizopus species</i>	0.7	0.6	0.4	0.3	0.3
<i>Candida albicans</i>	0.7	0.5	0.5	0.4	0.3
<i>Aspergillus fumigatus</i>	0.5	0.4	0.4	0.3	0.3

Table 3: Antifungal activity of *Solanum nigrum*.

Fungal species	Zone of Inhibition (cm)				
	0.5 ml	0.25 ml	0.125 ml	0.0625 ml	0.3125 ml
<i>Fusarium</i>	0.4	0.4	0.3	0.3	0.3
<i>Rhizopus species</i>	0.8	0.7	0.6	0.5	0.3
<i>Candida albicans</i>	0.7	0.5	0.4	0.3	0.3
<i>Aspergillus fumigatus</i>	0.8	0.5	0.5	0.4	0.3

Table 4: Antifungal activity of *Helianthus annuus*.

Fungal species	Zone of Inhibition (cm)				
	0.5 ml	0.25 ml	0.125 ml	0.0625 ml	0.3125 ml
<i>Fusarium</i>	0.5	0.4	0.4	0.3	0.3
<i>Rhizopus species</i>	0.5	0.4	0.4	0.4	0.3
<i>Candida albicans</i>	0.6	0.5	0.4	0.3	0.3
<i>Aspergillus fumigatus</i>	1.0	0.9	0.7	0.5	0.4

The Distance calculated using MATLAB displays the Euclidean distance between the two endpoints of the line in a label superimposed over the line and specifies the distance in data units determined by the X Data and Y Data properties, which is pixels. This is used as input for calculating the automated distance which measures the zoomed distance and original distance.

3 Results

Antibacterial and antifungal activity was performed and obtained images were represented in Figure 1, 2, 3, 4, 5, 6. Table 1 represents antibacterial activity of extracts of *Solanum xanthocarpum*, *Solanum nigrum* and *Helianthus annuus*. Zone of inhibition were measured for antibacterial activity. *Solanum xanthocarpum* showed better activity when compared to *Solanum nigrum* and *Helianthus*

annuus. Table 2, 3, 4 represents antifungal activity of the extracts. *Solanum nigrum* and *Helianthus annuus* exhibit better antifungal activity (the region of inhibition measures a maximum value of 0.5cm in a low concentration of 0.0625ml) when compared to *Solanum xanthocarpum*. Comparative analysis of manual and automated measurements of region of inhibition was represented in Table 5, 6.

4 Discussion

Solanum xanthocarpum is non-toxic and safe for human use and is regarded as a valuable plant in both Ayurveda and modern drug development areas for its versatile medicinal uses. *Solanum nigrum* inhibits the growth of several carcinomas. Further studies of other phytoactive compounds will possibly lead to exploration of new

Table 5: Antibacterial assay and Comparative analysis of manual and automated measurements of region of inhibition.

Extract	Name of Species	Zoomed inner diameter (mm)	Zoomed inner radius (mm)	Zoomed outer diameter (mm)	Zoomed outer radius (mm)	Zoom ratio	Obtained distance (manual cm)	Measured Distance (cm)
<i>Solanum nigrum</i>	<i>Salmonella typhi</i>	199.13	99.565	1624.94	812.47	180.548	0.5515	0.6
	<i>Bacillus subtilis</i>	172.0500	86.0250	1588	794	172.050	0.4875	0.5
	<i>Staphylococcus aureus</i>	288.71	144.355	1600	800	177.778	0.8120	0.8
	<i>Vibrio Cholera</i>	204.500	102.250	1605.20	802.600	178.355	0.5733	0.65
<i>Solanum xanthocarpum</i>	<i>Salmonella typhi</i>	329.83	164.915	1615.32	807.66	179.48	0.9188	1.05
	<i>Bacillus subtilis</i>	186	93	1830.74	915.37	203.415	0.4572	0.45
	<i>Staphylococcus aureus</i>	192	96	1614	807	179.33	0.5353	0.5
	<i>Vibrio cholera</i>	236.96	118.48	1670	835	185.556	0.6385	0.7
<i>Helianthus annuus</i>	<i>Salmonella typhi</i>	330	165	1702	851	189.111	0.8725	0.95
	<i>Bacillus subtilis</i>	174.050	87.0250	1584	792	176	0.4944	0.5
	<i>Staphylococcus aureus</i>	270	135	1710	855	190	0.7105	0.7
	<i>Vibrio cholerae</i>	235.42	117.710	1768	884	196.44	0.5994	0.6

methods for therapeutic applications. *Helianthus annuus* possesses various pharmacological activities. However, it is imperative that more clinical and pharmacological studies should be conducted to investigate the unexploited potential of this plant

The results of the present study showed *Solanum xanthocarpum* exhibits better antibacterial activity by being sensitive factor towards bacterial medium. The present study reveals that active principles present in plant extracts are active against all the tested bacterial strains. Based on earlier reports, phytochemical compounds found in plants like terpenoids, alkaloids, flavanoids represent the main antibacterial agents [2]. So the antibacterial activity shown by methanolic extracts might be due to some antimicrobial substances present in them [15]. *Solanum nigrum* and *Helianthus annuus* exhibit better antifungal activity by being sensitive factor towards fungal medium and the region of inhibition measures a maximum value of 0.5cm in a low concentration of 0.0625ml of both the extracts. They possess better minimum inhibitory concentration values. Antimicrobial properties of extracts against tested microbial strains suggest that the respective crude extracts can be effectively used for common infectious diseases.

Digital image processing techniques were employed and better results were obtained. The color filling tech-

nique following the color coding yields a better image which can be distinguished by its individual color for different regions. It makes the region of inhibition more prominent by its individual color from the surrounding microbe prone area and helps in accurate measurement.

5 Conclusion

In conclusion methanol extracts of dried fruits of *Solanum xanthocarpum*, *Solanum nigrum* and dried seeds of *Helianthus annuus* possess a broad spectrum of activity against a panel of bacterial and fungal strains responsible for common infections. Digital image processing techniques were applied on antimicrobial images and various features extracted were analyzed and studied. The comparative analysis measurements of region of inhibition shows that the automated results were nearly equal to the manual counted ones. These promissory extracts open the possibility of finding new clinically effective antimicrobial compounds.

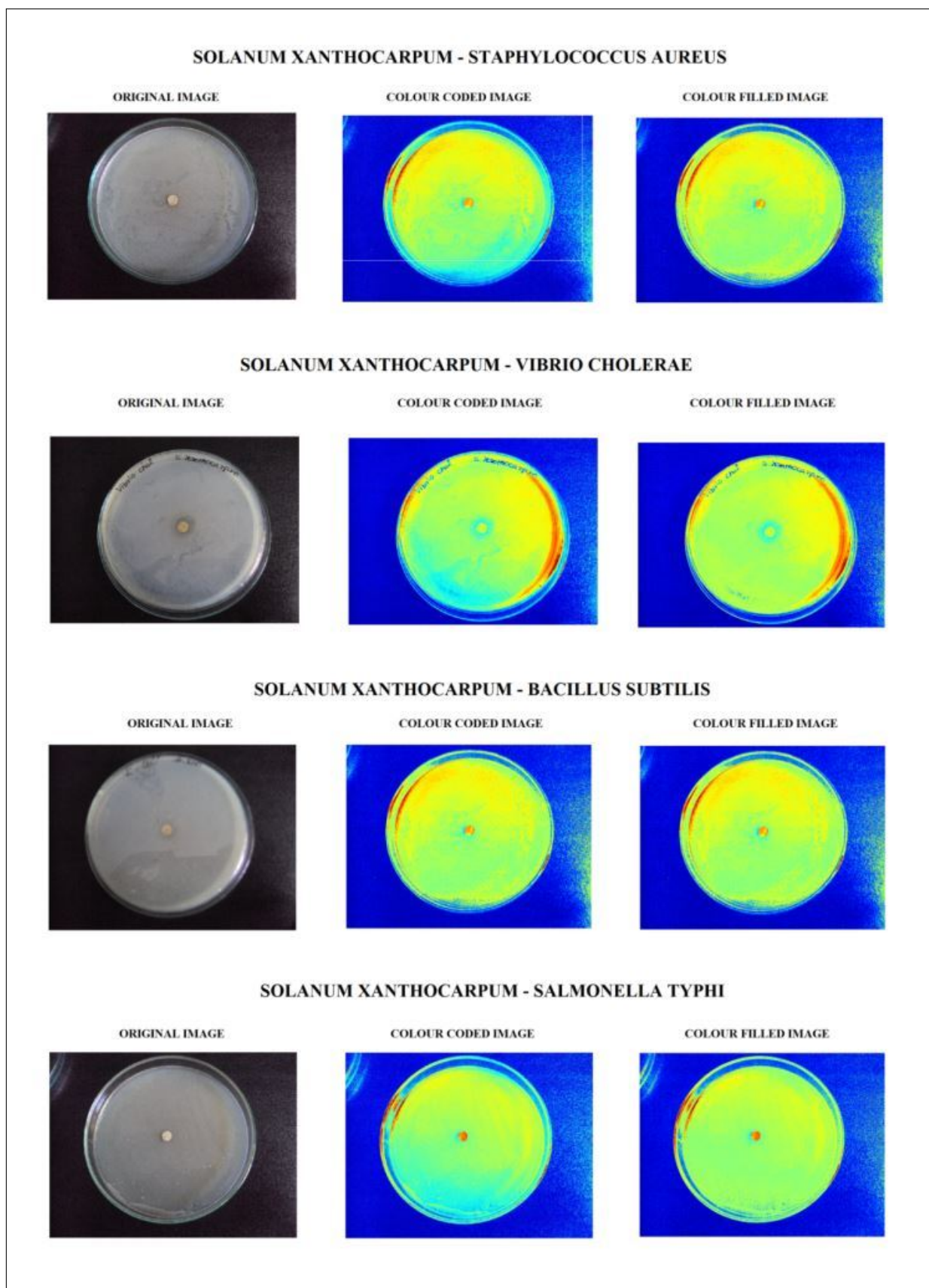
References

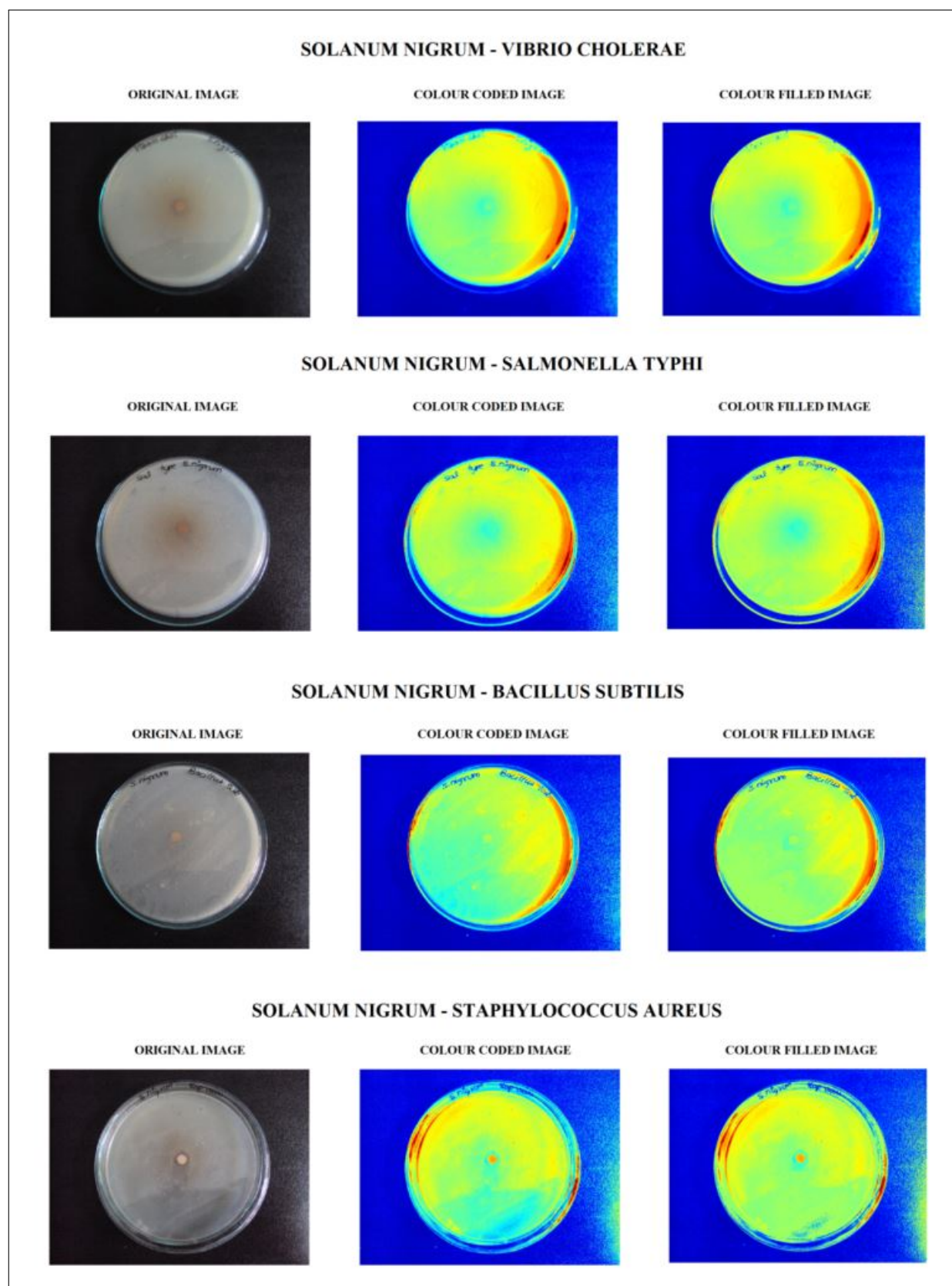
- [1] Alavijeh PK, Sharma D. A study of antimicrobial activity of few medicinal herbs, Asian Journal of Plant Science and Research. 2012. 2 (4):496-502

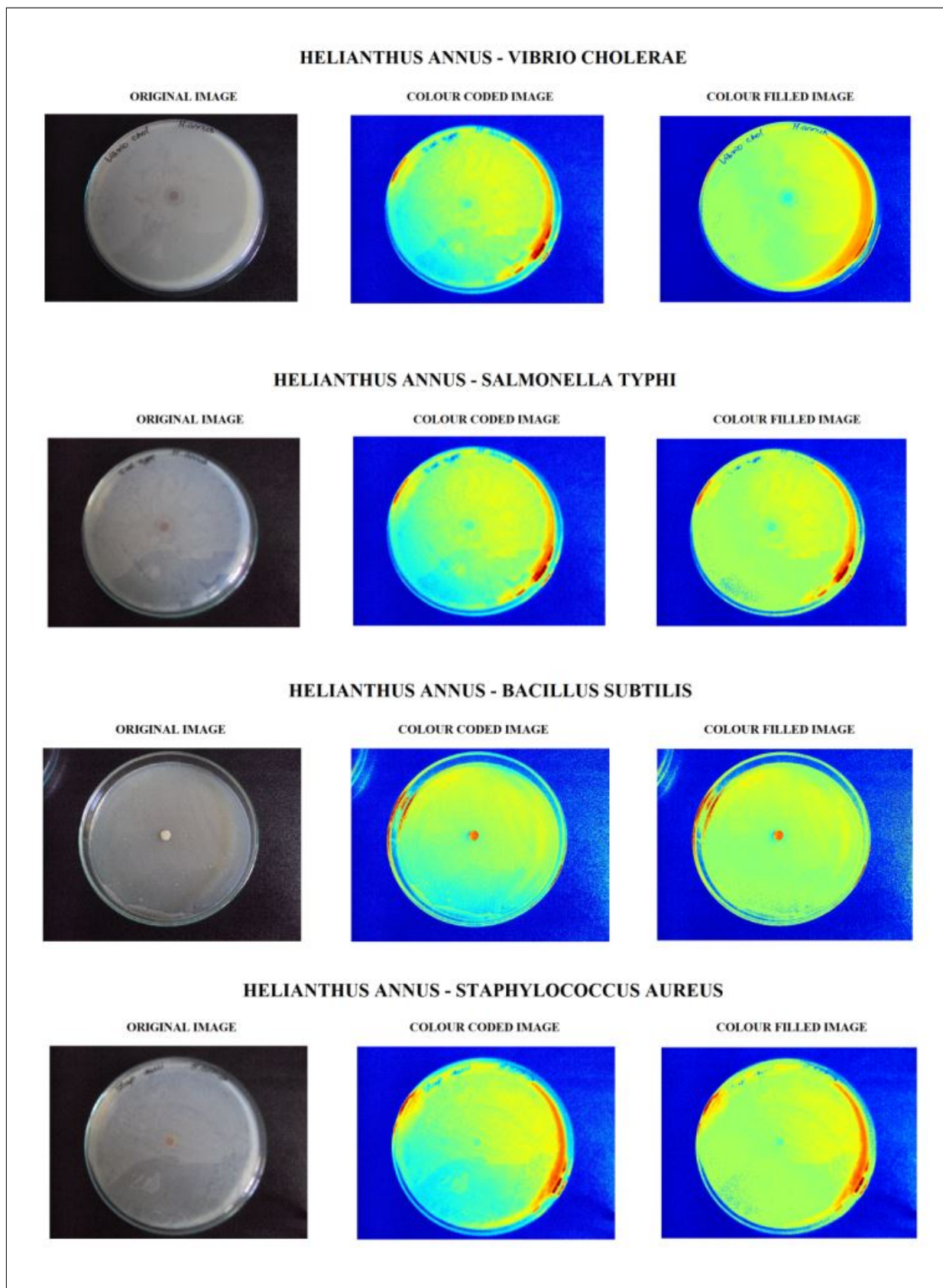
- [2] Udayakumar R, Velmurugan K, Srinivasan D, Krishna RR. Phytochemical and antimicrobial studies of extracts of *Solanum xanthocarpum*. *Anc Sci Life*, 2003, 23(2): 90–94.
- [3] Singh K, Aali NS, Khan MI, Ahirwar V. Effect of *Solanum nigrum* on protein content of liver and kidney of albino rats. *Pharmacie Globale (IJCP)*, 2011, 4 (08): 1-3.
- [4] Iqbal A, Sadaqat HA, Khan AS, Amjad M. Identification of sunflower (*Helianthus annuus*, Asteraceae) hybrids using simple-sequence repeat markers. *Genetics and Molecular Research*. 2010, 10 (1): 102-106.
- [5] Kannabiran K, Mohankumar, Guneseekar V. Evaluation of antimicrobial activity of saponin isolated from *Solanum xanthocarpum* and *Centella asiatica*. *Int J Nat Engg Sci*, 2009, 3: 22-25.
- [6] Saravanan S, Dhasarathan, P. Gastroprotective and Antioxidant Activity of *Solanum nigrum* Linn against Aspirin and Cold Restraint Stress induced Ulcerated Rats, *Research Journal of Immunology*. 2011, 4: 1-11.
- [7] Anjali CH, Dash M, Chandrasekaran N, Mukherjee A. Antibacterial activity of sunflower oil microemulsion. *International Journal of Pharmacy and Pharmaceutical Sciences*. 2010, 2: 123-128.
- [8] Lili NA, Khalid F, Borhan NM. Classification of Herbs Plant Diseases via Hierarchical Dynamic Artificial Neural Network after Image Removal using Kernel Regression Framework. *International Journal on Computer Science and Engineering*, 2011, 3: 15-20.
- [9] Pornpanomchai C, Rimdusit S, Tanasap P, Chaityod C. Thai Herb Leaf Image Recognition System (THLIRS). *Kasetsart Journal of Natural Science*. 2011, 45: 551-562.
- [10] Laurel A, MokaleKognou. Antibacterial and Antioxidant Properties of the Methanolic Extract of the Stem Bark of *Pteleopsis lyodendron* (Combretaceae), *Chemotherapy Research and Practice*, 2011, 1- 7.
- [11] Sidambaram R, Dinesh MG. Antibacterial, antifungal and cytotoxic studies on leaf and seed extracts of *Solanum xanthocarpum* shrub and wendl, *International Journal of Phytopharmacology*, 2011, 2(2):61-65.
- [12] Sanni S, Onyeyili PA. Phytochemical Analysis, Elemental determination and Some in vitro Antibacterial Activity of *Ocimum basilicum* L. Leaf Extracts, *Research Journal of Phytochemistry*, 2008, 2:77-83.
- [13] Sharma D, Lavania AA. In vitro Comparative Screening of Antibacterial and Antifungal Activities of Some Common Plants and Weeds Extracts, *Asian J. Exp. Sci*, 2009, 23, 169-172.
- [14] Cowan, M.M. Plant products as antimicrobial agents, *Clinical Microbiology Reviews*, 1999, 12 (4): 564–582.
- [15] Siddiqui S, Verma S, Rather AA, Jabeen F, Mukesh K. Preliminary phytochemical analysis of some important medicinal and aromatic plants. *Advan. Biol.Res*, 2009, 3 (5-6): 188-195.

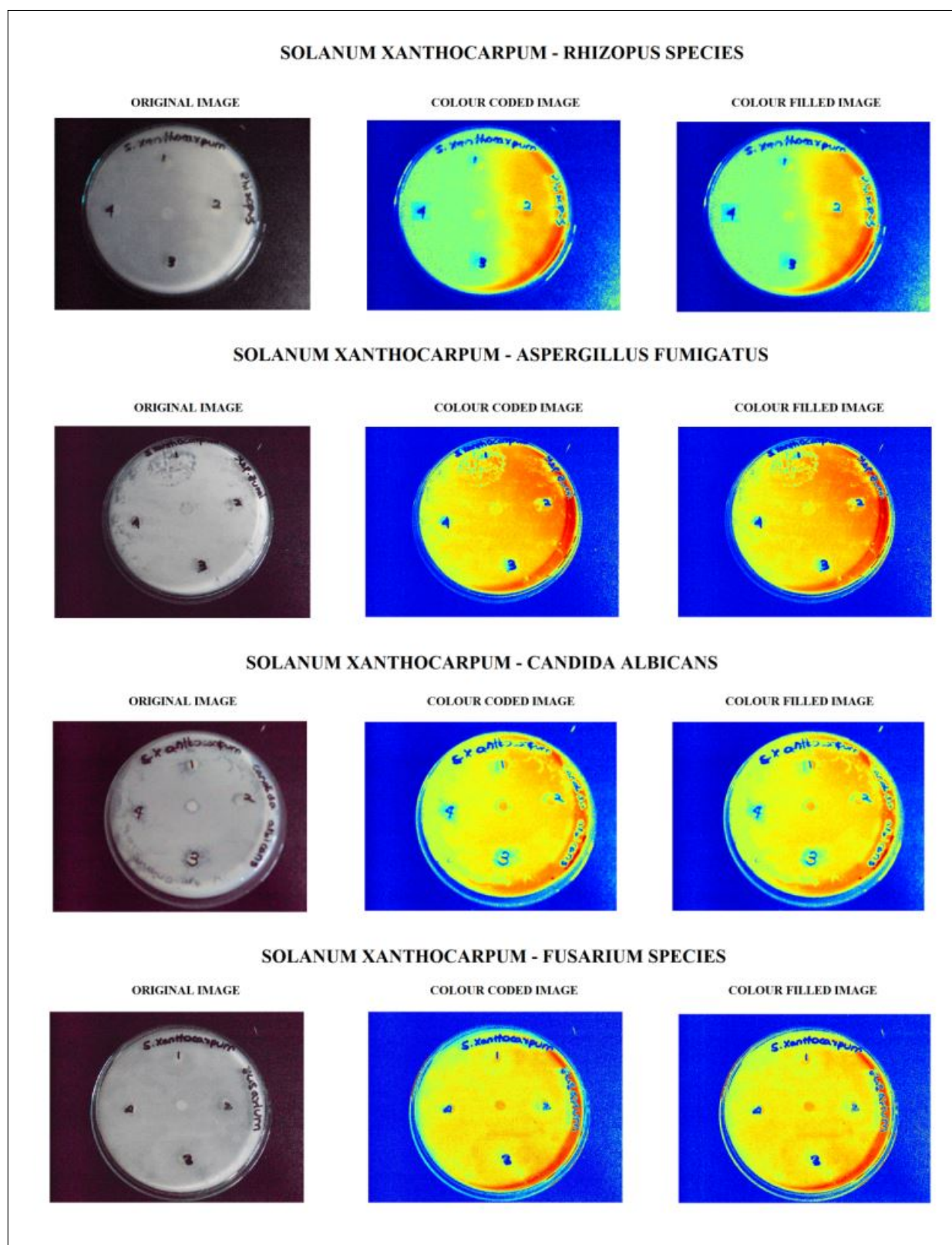
Table 6: Antifungal assay and Comparative analysis of manual and automated measurements of region of inhibition.

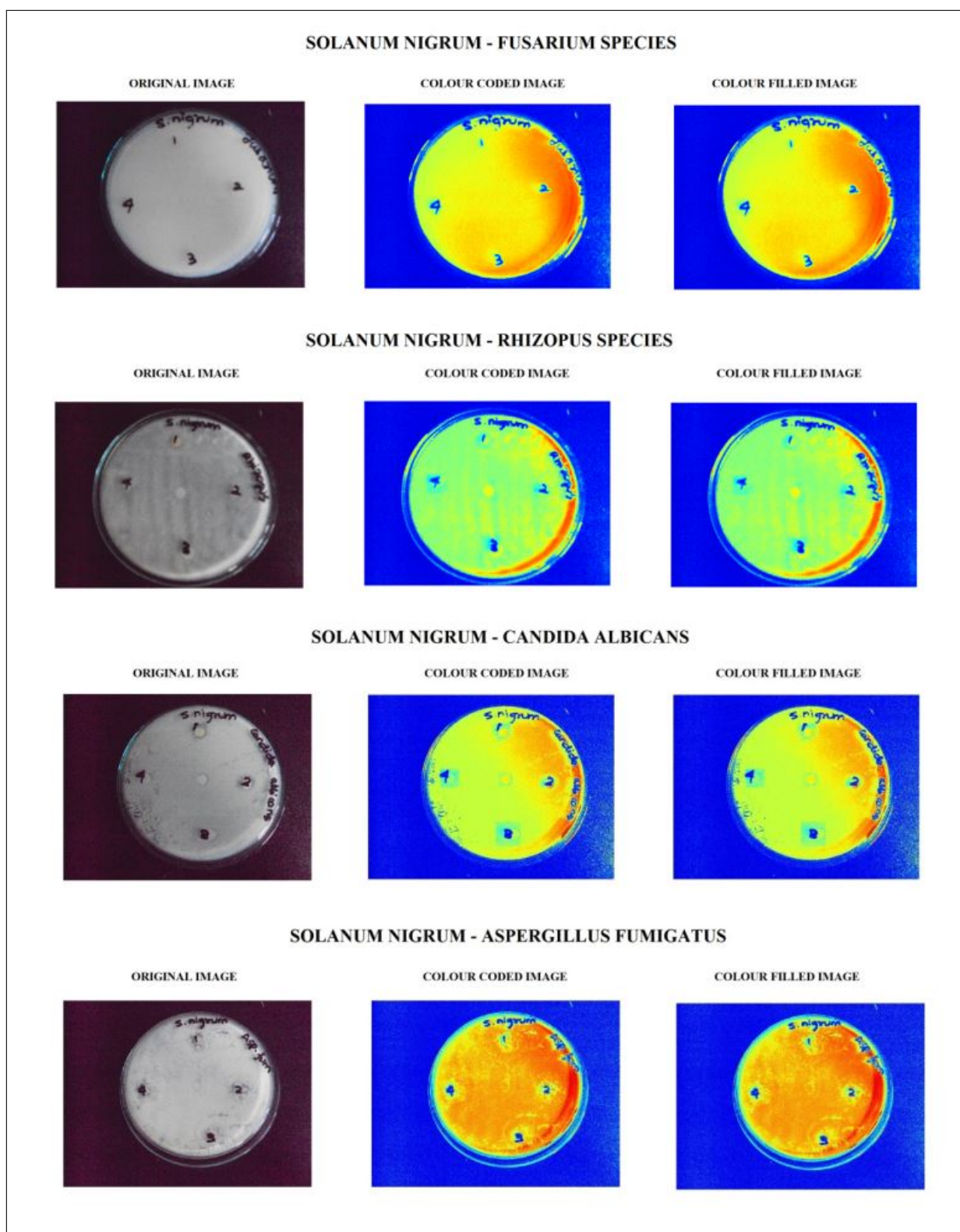
Extract	Name of Species	Zoomed inner diameter (mm)	Zoomed inner radius (mm)	Zoomed outer diameter (mm)	Zoomed outer radius (mm)	Zoom ratio	Obtained distance (manual cm)	Measured Distance (cm)
<i>Solanum nigrum</i>	<i>Fusarium</i>	140.04	70.02	1670.20	835.10	185.55	0.3772	0.4
		136	68	1674	837	186	0.3656	0.4
		123	61.50	1660	830	184.44	0.334	0.3
		126	63	1666	833	185.11	0.340	0.3
		126	63	1666	833	185.11	0.340	0.3
	<i>Rhizopus species</i>	288.71	144.3550	1600	800	177.77	0.8120	0.8
		270	135	1710	855	190	0.7005	0.7
		199.13	99.565	1624.94	812.47	180.54	0.5515	0.6
		172.07	86.03	1586	793	172.03	0.4885	0.5
		123	61.50	1666	833	184.44	0.333	0.3
	<i>Candida albicans</i>	236.96	118.48	1670	835	185.55	0.6585	0.7
		186	93	1830.74	915.37	203.42	0.4672	0.5
		138	69	1672.20	836.10	186.02	0.3782	0.4
		126	63	1668	834	185.16	0.330	0.3
		124	62	1662	831	184.44	0.334	0.3
	<i>Aspergillus fumigatus</i>	270	135	1710	855	190	0.7105	0.7
		172.05	86.02	1588	794	173.05	0.4775	0.5
		186	93	1830.74	915.370	203.42	0.458	0.5
		123	61.50	1668	834	184.48	0.323	0.3
		124	62	1664	832	184.45	0.334	0.3
<i>Solanum xanthocarpum</i>	<i>Fusarium</i>	288.71	144.355	1600	800	177.78	0.8120	0.8
		199.13	99.565	1624.94	812.47	180.54	0.5616	0.6
		172.05	86.025	1588	794	172.05	0.4875	0.5
		123	61.50	1660	830	184.44	0.334	0.3
		130	65	1674	837	187.23	0.322	0.3
	<i>Rhizopus species</i>	270	135	1710	855	190	0.7105	0.7
		204.500	102.250	1605.20	802.600	178.36	0.5733	0.6
		144	72	1670	835	186.55	0.387	0.4
		126	63	1666	833	185.11	0.330	0.3
		124	62	1674	837	187.23	0.332	0.3
	<i>Candida albicans</i>	236.96	118.48	1670	835	185.56	0.638	0.7
		174.050	87.0250	1584	792	176	0.4944	0.5
		186	93	1830.74	915.37	203.42	0.477	0.5
		136	68	1674	837	186	0.376	0.4
		123	61.50	1660	830	184.44	0.334	0.3
	<i>Aspergillus fumigatus</i>	172.050	86.0250	1588	794	172.05	0.4875	0.5
		140	70	1670	835	185.55	0.3772	0.4
		136	68	1674	837	186	0.3666	0.4
		130	65	1674	837	187.23	0.323	0.3
		126	63	1666	833	185.11	0.330	0.3
<i>Helianthus annuus</i>	<i>Fusarium</i>	140	70	1670	835	185.55	0.3777	0.4
		144	72	1670	835	186.55	0.387	0.4
		126	63	1666	833	185.11	0.330	0.3
		123	61.50	1666	833	184.42	0.324	0.3
		124	62	1674	837	187.23	0.332	0.3
	<i>Rhizopus species</i>	288.71	144.3550	1600	800	177.78	0.8120	0.8
		270	135	1710	855	190	0.7105	0.7
		199.13	99.565	1624.94	812.467	180.55	0.5715	0.6
		172.05	86.025	1588	794	172.05	0.4875	0.5
		130	65	1674	837	187.23	0.323	0.3
	<i>Candida albicans</i>	236.96	118.48	1670	835	185.56	0.6385	0.7
		192	96	1614	807	179.33	0.5153	0.5
		140	70	1670	835	185.55	0.3872	0.4
		126	63	1666	833	185.11	0.330	0.3
		124	62	1674	837	187.23	0.331	0.3
	<i>Aspergillus fumigatus</i>	288.71	144.3550	1600	800	177.78	0.8120	0.8
		0.4875	172.050	86.025	1588	794	0.4876	0.5
		186	93	1830.74	915.37	203.42	0.4572	0.5
		123	61.50	1666	833	184.44	0.324	0.3
		130	65	1674	837	187.23	0.323	0.3

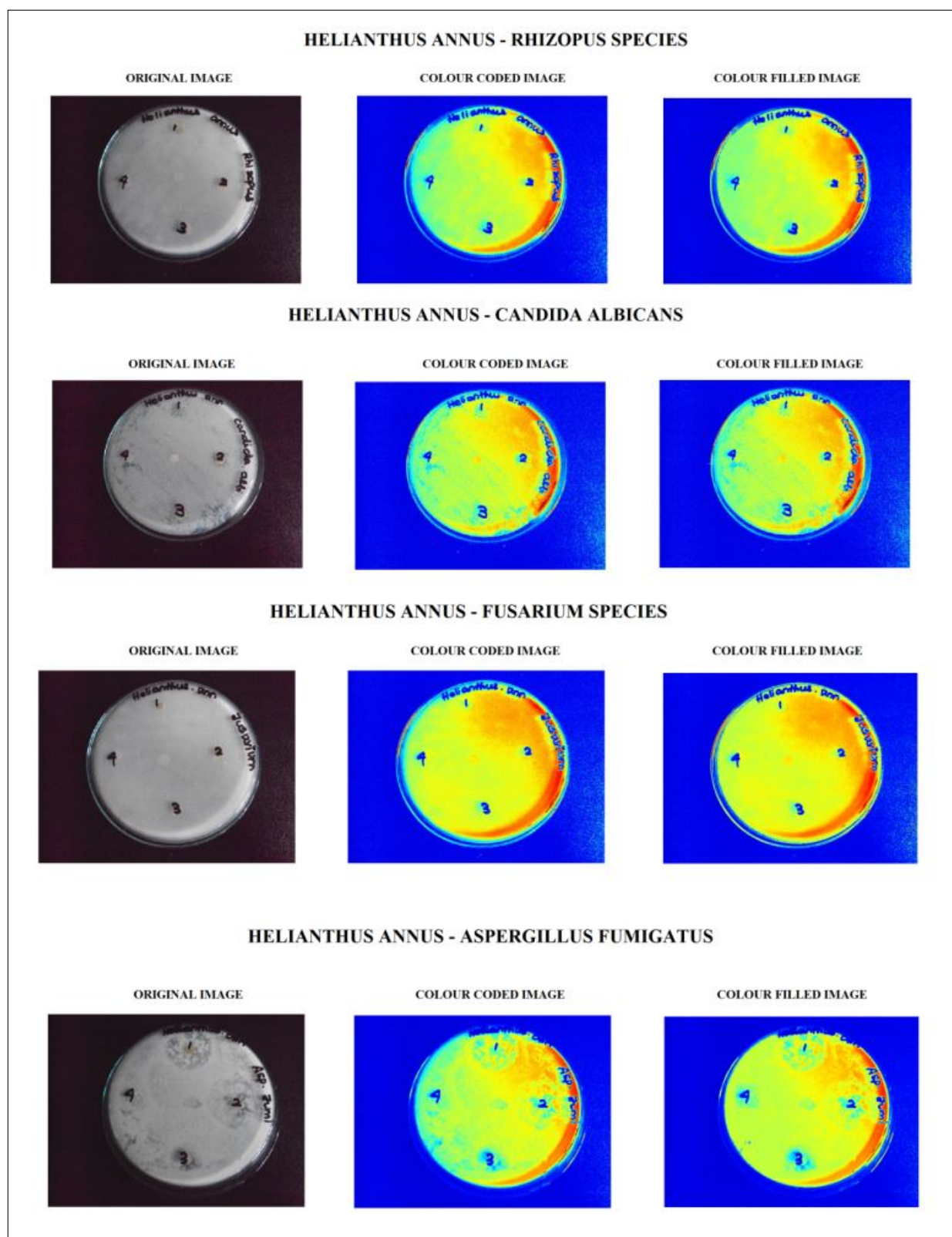
Figure 1: Antibacterial Images of *Solanum xanthocarpum*.

Figure 2: Antibacterial Images of *Solanum nigrum*.

Figure 3: Antibacterial Images of *Helianthus annuus*.

Figure 4: Antifungal Images of *Solanum xanthocarpum*.

Figure 5: Antifungal Images of *Solanum nigrum*.

Figure 6: Antifungal Images of *Helianthus annuus*.

Musculoskeletal Modeling of Hip Joint and Fracture Analysis for Surgical Planning Using FEA

Sathya Ganapathi¹, Shilfa Thoppay Premkumar¹, Thenmozhi Malaikannu¹, Kavitha Anandan¹

¹ Department of Bio-medical Engineering, Sri Sivasubramaniya Nadar College of Engineering, Chennai, India

Abstract

Background: Hip fractures are a major cause for disability in patients. They require immediate attention as they could otherwise cause death. Hip fractures are almost always treated with surgery by implantation. Implants are of various types accounting for the many variations in hip fractures.

Objectives: This paper presents the design and analysis of a hip implant using Finite element analysis. Fracture conditions are determined and the optimal design of the implant is obtained for improving healthcare and patient safety.

Methods: Anthropometric parameters of the human femur bone are collected from a particular age group. These are then used to obtain a CAD model of the bone using CATIA. The standard Charnley hip implant, used in total hip replacement surgery is also modeled. The proposed models are analyzed using ANSYS software by assigning appropriate material properties to the bone and implant. The stress distribution is observed when loads corresponding to normal gait conditions are applied. The load at which fracture occurs is then determined experimentally.

Results: Based on the analysis results of the modeled bone, the implant is optimized by varying the base cross section, the bio-materials used, and the design parameters so that, its stress response mimics that of the actual bone. It is found that the model no 2 as in Table 6 with head diameter 28mm, neck diameter 10mm, neck angle 128 degrees has minimum strain at the neck region with a value of 0.65 and is found to be suitable for implant design. Results show that initiation of fracture in the implant occurs at 2000N and complete fracture occurs at 2400N.

Conclusions: The 3D models are very useful in simulation of bone fractures and internal fixations with implants. In this work, the hip joint and implant model, developed in CATIA software, help to understand how these structures adapt to external forces disturbances [15]. This will help the doctors to choose the optimal implant for a particular patient. This leads to greater accuracy and patient specificity.

Keywords

Finite element modeling, Fracture analysis, Gait cycle, Hip joint, Charnley hip implant model

Correspondence to:

Anandan Kavitha

Department of BME, SSN College of Engineering
Address: Kalavakkam, Chennai – 603110
E-mail: kavithaa@ssn.edu.in

EJBI 2013; 9(2):27–36

received: January 16, 2013

accepted: March 25, 2013

published: August 30, 2013

1 Introduction

The hip joint serves a very important biomechanical function. While supporting the majority of the human body ($\sim 2/3$ of total bodyweight) the joint must simultaneously facilitate smooth articulation of the lower limbs to enable bi-pedal gait. During routine daily activities, forces on the order of 5.5 times bodyweight are transferred between the femur and pelvis [11]. Fracture is the most important aspect of joints. Factors such as abnormal joint geometry, body weight, and prior injury are stated as major cause for hip fracture. Heavy loads on joint are implicated as the significant cause for the hip fracture. In recent years the number of hip fractures continues to increase in elderly population. Worldwide, the total number of hip fractures is expected to overstep 6 mil-

lion by the year 2050 [1]. Approximately one-third of fracture patients went on to receive a hip replacement [2, 3, 4, 5]. There are four different types of fracture patterns (i) Femoral head fracture, involving the femoral head. (ii) Femoral neck fracture (iii) Subtrochanteric fracture involving the shaft of the femur immediately below the lesser trochanter (iv) due to diseases such as Osteoporosis. All of these fractures are treated by strenuous surgical procedures that involve implantation. But total hip replacement surgery is done predominantly in older patients with femoral neck fracture as they would be unable to withstand plates or nails.

The design of the hip prosthesis has been modified continuously to grapple with the advanced technology and patients postulates. Many new approaches have been evidenced in hip joint analysis with better material design

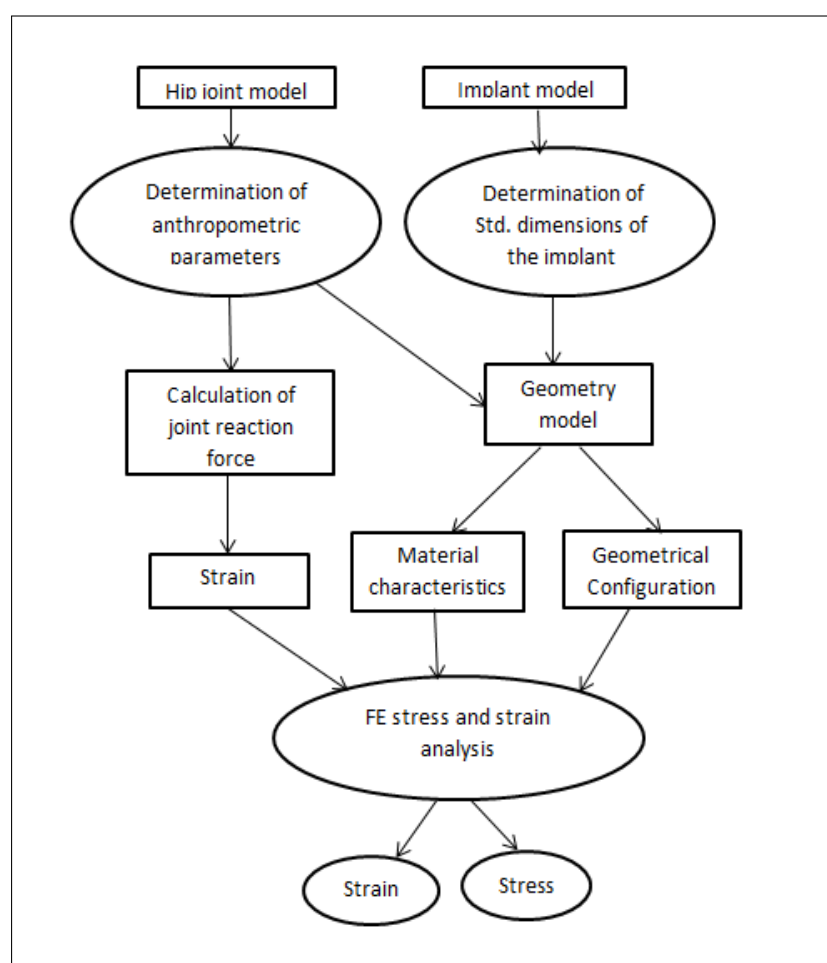


Figure 1: Flowchart for the approach.

and computer technology. Existing implants are not custom made for Indian anatomical specifications and hence cause problems in surgery. Also, choice of implant is a subject of debate. This proves the need for implant optimization.

In this study, three design parameters are chosen to investigate what further modifications can be made in the current implant design, that will increase its efficiency. This is done by observing the stress response of the implant using FEA. By analyzing through the computational protocol, distribution of stress can be depicted and the error and uncertainty for particular body gesture can be assessed [14]. In this work, it is proposed to model the acetabular-femur joint. In the development of modern computational techniques, attention of researchers has now turned toward using combined 3D reconstruction and virtual environment technologies to train clinicians and to help surgeons plan patient-specific, complex procedures like plastic surgery, surgery for trauma from accidents and reconstruction surgery. The 3D models are very useful in simulation of bone fractures and internal fixations with implants. These models are also important to understand how human musculoskeletal structures adapt to external forces disturbances [15, 16, 17].

Due to the usage of software the surgical procedures are avoided and it also helps to design a better implant. The subject-specific models are generated by using biomechanical modeling and analysis of a joint. In the recent scenario successful hip replacement surgery is done with the Charnley model implant in most of the cases.

2 Methods

Owing to the complexity of the work, it was divided into several phases as shown in Fig 1. The process can be broadly classified into Modelling and analysis. The implant and bone model are dealt with separately. The process is as explained below.

For the design of human hip joint three significant anthropometric parameters that vary with age, height, weight of a person are considered [16] and the biomaterial characteristics of the hip joint are also added to improve the accuracy of the study. For the load acting on the joint, theoretical calculation of joint reaction force is done with respect to the gravitational force acting on the hip joint and body weight, for a complete gait cycle. For determining the fracture condition the FEA method is used. The material characteristics of the bone and implant is

summed up during FEA analysis. In the final phase FEA is accomplished and stress and strain distributions were obtained. Accuracy is assessed by comparison of theoretical value with that of experimental results.

Table 1: Measured anthropometric parameters.

Parameters	Obtained values	Mean	Standard deviation
Horizontal offset (in cm)	4.2	3.88	± 0.03
	3.5		
	4.1		
	3.7		
	3.9		
Femoral head diameter (in cm)	4.7	4.24	± 0.552
	3.9		
	4.5		
	3.8		
Neck shaft angle (in degrees)	133	131	± 0.43
	129		
	130		
	128		
	131		

2.1 Modeling

Modeling involves using a set of measured anthropometric parameters to construct a CAD (Computer Aided Design) model of the femur bone. This will be a 3 dimensional computerized model of the actual bone and will serve as an input to the next stage i.e finite element analysis. The implant model can be constructed from standard dimensions.

There are many softwares that can be used for modeling a human joint like CAD, PRO-E, ABACUS, AUTOCAD, SOLIDWORKS etc.[7]. These softwares are programmed for designing perfect machinery and aerospace parts. CATIA provides a unique set of tools that provide benefits like faster design, reduced lead times, quality of surfaces, associative drawings and innovative solutions. Moreover, CATIA has been widely used for modeling biomechanical joints [12]. Thus, it has been chosen.

Selection of Anthropometric Parameters

Modeling the femur bone in CATIA requires that, some parameters that define the basic geometry of the bone be given as input. It has been proven in earlier publications that the following three parameters measured, will prove to be adequate in representing the bone's geometry. The parameters are femoral head diameter, neck shaft angle and horizontal offset. These parameters depend upon demography. Radiographic images (N=5) of the hip joint belonging to five male patients of age ranging from 45 to 55 are obtained from a hospital. The parameters are measured using digital caliper and micrometer. The values are tabulated and mean values are calculated

and used for modeling. Patient demographics are as indicated in Table 1 and the measured parameters are as given in Table 2.

Table 2: Measured Demographic Parameters.

S. No	Age	Height (cm)	Weight (Kg)
1	55	151.25	58
2	43	150.5	55
3	49	156	60
4	45	153	56
5	47	154.5	59

Modeling in CATIA-V5

In CATIA V 5.0 2-D working plane is selected for initial modeling of hip joint. The measured anthropometric parameters are used as input various tools from Sketcher Work Bench, the sketch can be designed. The mean values used are as in Table 3. Various taskbars and menus help to draw a needed shape and dimension. Measured anthropometric parameters are given as input while designing the hip joint in the sketcher toolbox. The final 2-D design is converted into 3-D model by applying constraints to the sketch and creating a pad on exiting the workbench. The constraints mentioned here refer to the geometrical measurements such as length, breadth and angles. These values are implemented using the measured parameters. The hip joint model is as shown in Fig 2.

Table 3: Anthropometric parameters (average) used for modeling the hip joint.

Horizontal offset (in cm)	Femoral head diameter (in cm)	Neck shaft angle (in degrees)
3.88	4.3	131

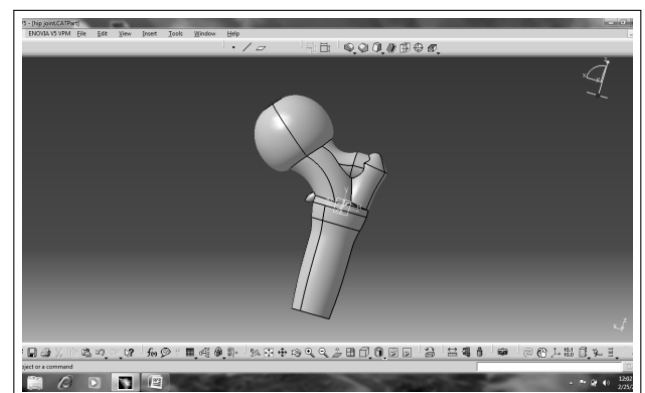


Figure 2: The designed hip joint model.

Charnley Hip Implant

The Charnley implant has 4 major parts- the acetabular cup made up of stainless steel 316L, the acetabular

liner made up of Ultra High Molecular Weight Polyethylene (UHMWPE) that lubricates the joint and the femoral part with head, neck and tail portions which is also made up of stainless steel 316L. The liner fits inside the cup for replacing the function of cartilage in order to enable easy movement of the hip joint [18].

The standard dimensions of the implant are obtained from manufacturers, using which the implant is modeled in CATIA. The implant dimensions used have been tabulated in Table 4. The modeled implant is as shown in Fig 3.

Table 4: Standard Dimensions Of The Implant.

Parameters	Values
Neck shaft angle	128 degrees
Femoral length	162 mm
Head diameter	28 mm
Liner diameter	32 mm
Cup diameter	44 mm
Neck diameter	14 mm

This standard implant is further used for analysis and optimization. Optimization is done by varying the parameters like base cross-section, biomaterials and geometrical dimensions. These design parameters are varied and different models are done in CATIA and analyzed to obtain the most optimal values.

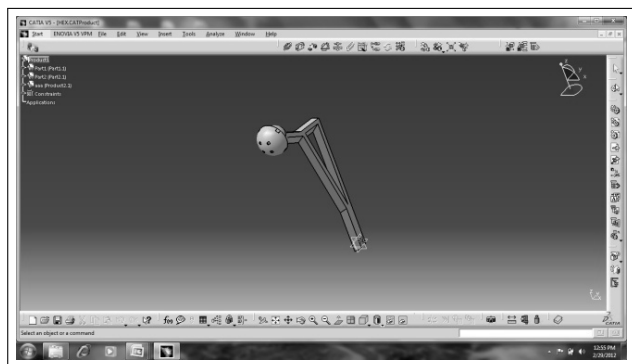


Figure 3: The designed implant model.

2.2 Finite Element Analysis (FEA)

FEA is a computational technique that is used to solve real world problems. Using FEA, it is possible to analyze and assess certain physical properties of objects. For example, FEA computes the strain developed in an object when subjected to a force or stress. The distribution of stress can also be viewed. Such computations are carried out based on the material properties of the specified object. Hence Finite Element Analysis will be of great use in observing the stress response of the hip joint.

ANSYS software is used to perform analysis. It is flexible, innovative, reliable, user friendly and compatible on complex structures like human bone joints.

Table 5: Phases of gait and load response on hip joint (BW = body weight) (1kg = 9.814 N).

Phases of gait	Planes of motion	Degrees of motion	Load applied (in BW)
Heel strike (initial contact)	Flexion	30	0.5BW
Single legged stance condition (loading response)	Flexion	5	2.7BW
	Abduction	4	
Terminal stance	Extension	10	2.5BW
Swing phase (initial swing)	Flexion	20	1BW
Mid swing	Flexion	30	1BW
Terminal swing	Flexion	30	1BW

Assigning Material Properties

The bone is a composite material made up trabecular and cortical bone. These types not only differ in their structures but also in mechanical properties. The hard outer layer of bones is composed of compact bone tissue, so-called due to its minimal gaps and spaces. Its porosity is 5–30% in an adult skeleton. Compact bone may also be referred to as dense bone. Filling the interior of the bone is the trabecular bone tissue (an open cell porous network also called cancellous or spongy bone), which is composed of a network of rod- and plate-like elements that make the overall organ lighter and allow room for blood vessels and marrow. Trabecular bone accounts for the remaining 20% of total bone mass but has nearly ten times the surface area of compact bone [8]. Consideration of this difference during analysis yields better results. However this has not been considered in this work. The primary tissue of bone is made up of osseous tissue, is a relatively hard and lightweight composite material, formed mostly of calcium phosphate also called as calcium hydroxyl apatite which gives strength and rigidity to the bone. It has relatively high compressive strength, of about 170 MPa (1800 kgf/cm²) [6] but poor tensile strength of 104–121 MPa [7] and very low shear stress strength (51.6 MPa), meaning it resists pushing forces well, but not pulling or torsional forces. For the surface of the bone with cortical structure, the appropriate properties are added and also for the region with trabecular bone together with the properties of calcium content [7, 8].

In the case of implants, four types of bio-materials are taken into consideration, depending upon their role as hip implants, such as Stainless steel 316L and UHMWPE, Tantalum, Ni-Ti alloy and Co-Cr alloy. The Metal alloys form the femoral stems, as they provide strength and endurance that allow the replacements, due to their solidity and resistance to wear and tear. Ceramic surfaces also provide a framework for Osseo integration. Polymers like ultra-high molecular weight polyethylene. The characteristic feature of the polymer is their elasticity and firmness

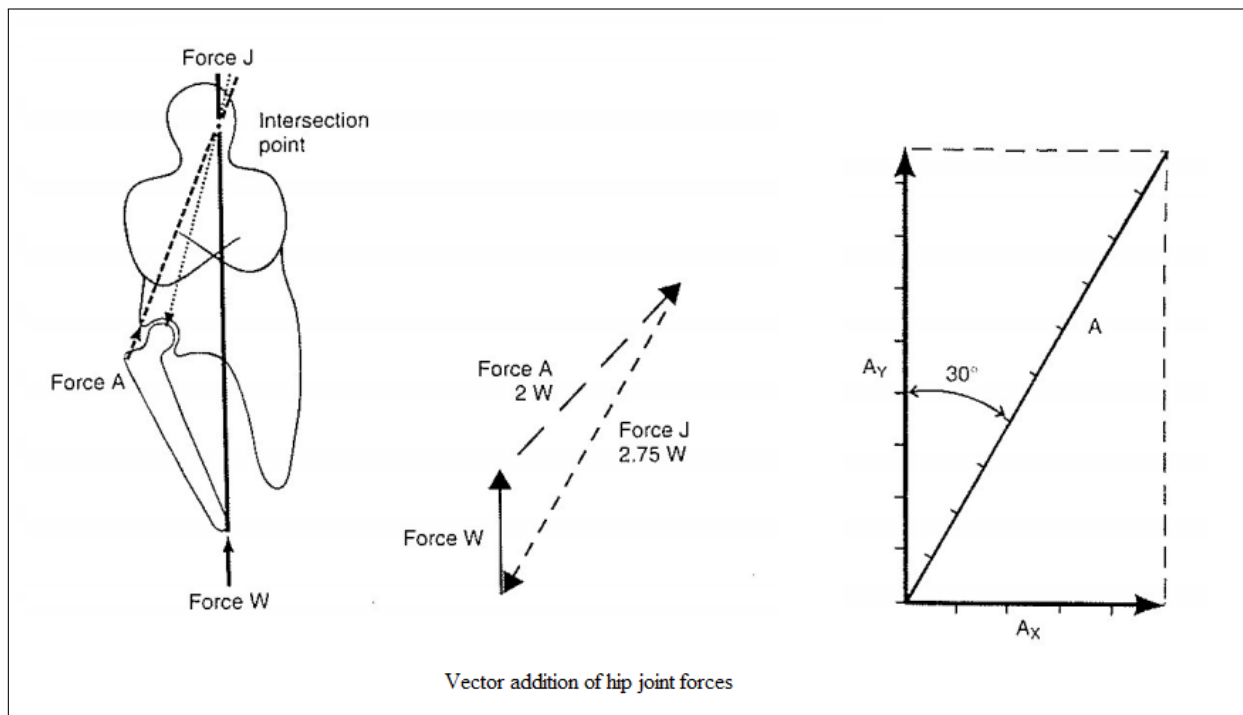


Figure 4: Free body diagram of hip joint during single legged stance condition.

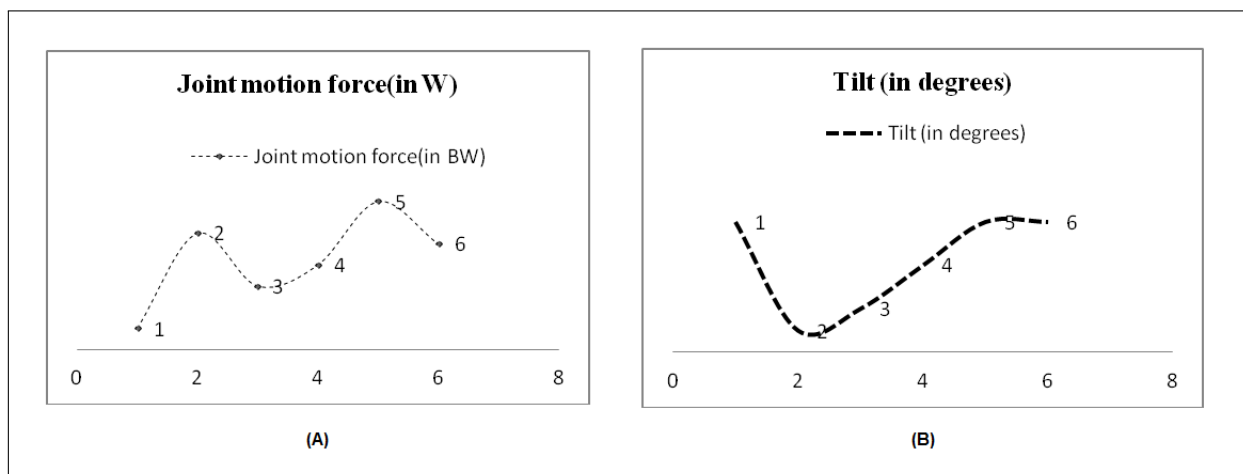


Figure 5: Graph A shows the joint motion force of the hip joint calculated using the free body diagram where BW is body weight and graph B showing the tilt of the joint (in degrees) during gait cycle 1. Heel strike, 2. Single Stance, 3. Terminal stance, 4. Swing phase, 5. Mid swing, 6. Terminal swing.

that offers frictionless joint mobility to hip replacement implants. Tantalum has a special feature and they are shape memory alloys [9]. A distinctive feature common to all these biomaterials is that all are biocompatible, that is they do not cause any inflammatory response and they seem to be natural [7, 8, 9, 10].

Loading Conditions

With every move our body makes, there is an internal force associated. This force is exerted on our limbs and thus cause movement. Hence, the bones in our body are naturally capable of bearing and reacting to these loads.

It is possible to calculate these loads from free body diagrams that depict gait cycles.

Gait cycle is defined as the Series of rhythmical, alternating movements of the trunk and the limbs which results in the forward progression of the center of gravity. Gait cycle has two alternating phases 1) stance phase (60%) 2) swing phase (40%).

Stance phase of the gait begins with the initial heel contact and ends with toe-off. The tasks performed are - weight acceptance (i) initial contact (ii) loading response, - single limb support (i) mid stance (ii) terminal stance and (iii) pre-swing. Swing phase encompasses the entire time the foot is in the air for limb advancement. The task

performed is – limb advancement (i) initial swing (ii) mid swing and (iii) terminal swing.

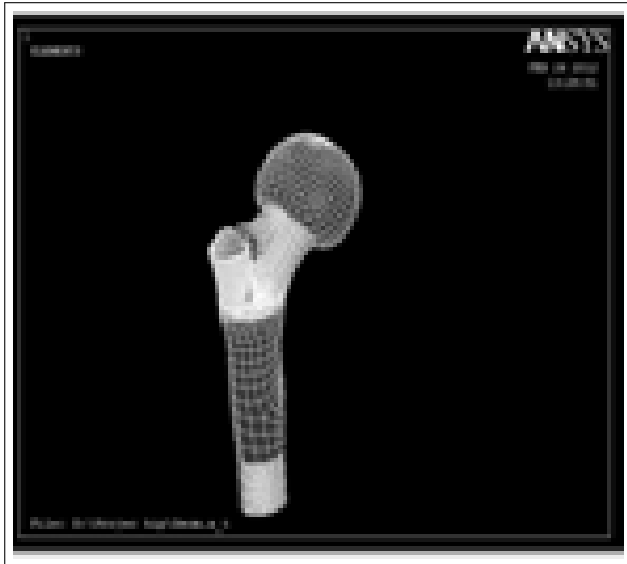


Figure 6: Mesh model of the hip joint.

Using the free body diagram technique as shown in Figure 4 and equilibrium equations, the maximum joint reaction force for each phases of the gait cycle is calculated [15]. The calculated joint motion force of the hip during each gait is shown in Figure 5.

The joint reaction force (J) is defined as the force generated within a joint in response to forces acting on the joint. It is due to the multiple muscles crossing the joint. A is the combined abductor muscle force and W is the body weight. From the free body diagram, the equilibrium equations for single legged stance phase are

$$\begin{aligned} A &= 2W & (1) \\ Ax &= A \sin 30 = 0.5A = W & (2) \\ Ay &= A \cos 30 = 0.8A = 1.7W & (3) \\ J &= Ax + Ay = 2.75W & (4) \end{aligned}$$

The values obtained are as shown in Table 5. Figure 5 (A) shows the plot of the calculated joint motion force for each phase of a gait cycle and Figure 5 (B) shows the degree of tilt for each phase of a gait cycle.

2.3 Numerical Analysis

In order to perform FEA, the model needs to be divided into small regions. This process is known as Meshing and will help the computer to solve the problem efficiently. The element used to build the mesh is a tetrahedron and two or more elements are connected by nodes.

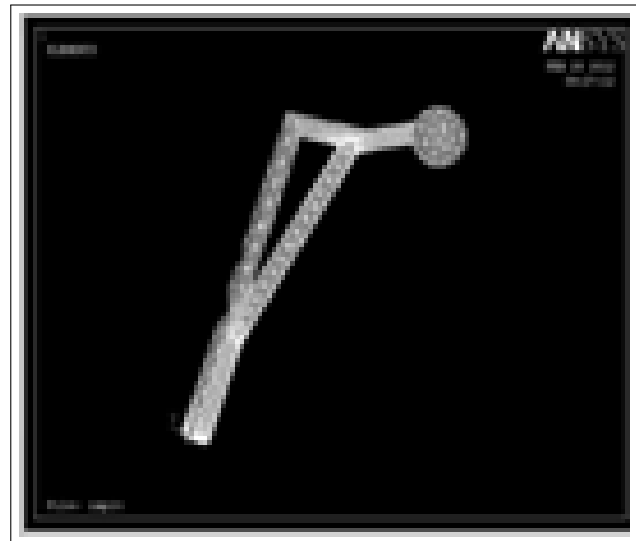


Figure 7: The designed implant model.

Table 6: Variation of design parameters of the implant.

Model no	Head diameter (mm)	Neck diameter (mm)	Neck angle (in degrees)
1	24	10	128
2	28	10	128
3	32	10	128
4	24	14	131
5	28	14	131
6	32	14	131
7	24	18	135
8	28	18	135
9	32	18	135

Various types of meshing modes are available in the software. 20 node 95 mode meshing is used for meshing the implant and free mesh h type mode is used for the modeled hip joint. Material properties are either selected manually or automatically from the ANSYS MATLIB file. The calculated loading conditions for each gait cycle are applied at the center of the femur head and the distribution of stress is observed. As a reaction to stress, strain is invoked. The software solves and determines these strain values invoked at the neck region of the hip joint. The meshed models of the hip joint and the implant are as shown in fig 6 and 7 respectively.

The results are obtained in the form of colour charts and animations. The red colour indicates maximum value of any particular result. Figure 8 shows the analysis of the femur bone during various phases of a gait cycle. It can be seen that the maximum stress is being held at the femoral head and is not being distributed to the shaft. The load is subsequently increased until the point of fracture. The point of fracture is considered to be the load at which the stress begins to penetrate down the length of the bone. This can be observed in Figure 8 (f).

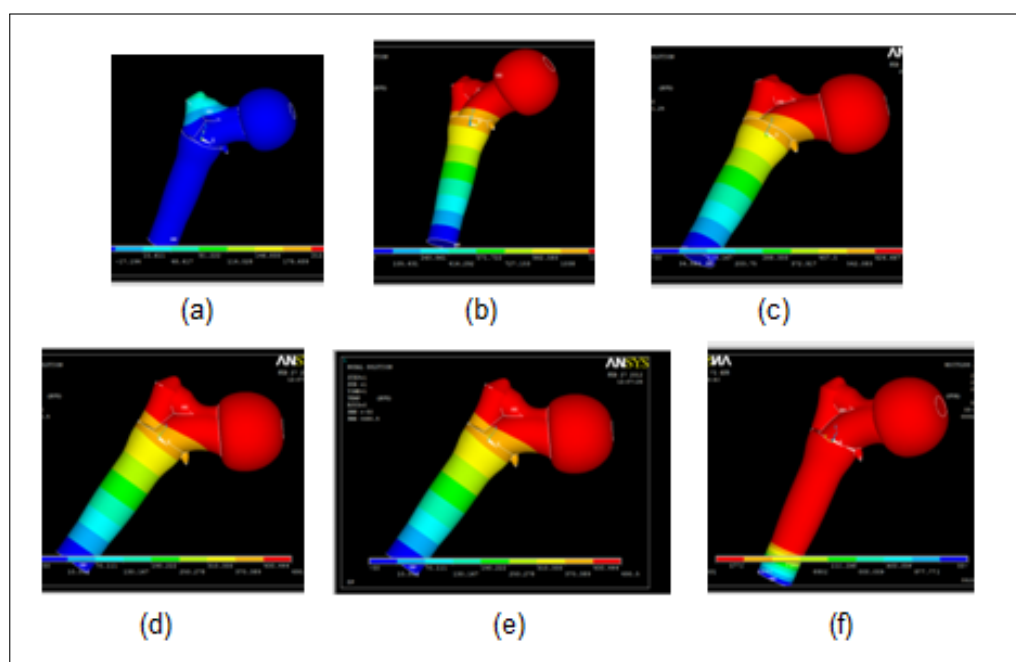


Figure 8: Hip joint analysis during (a). Two legged stance (b). Heel strike (c). Single legged stance (d). Terminal stance (e). Swing phase (f). Load of fracture.

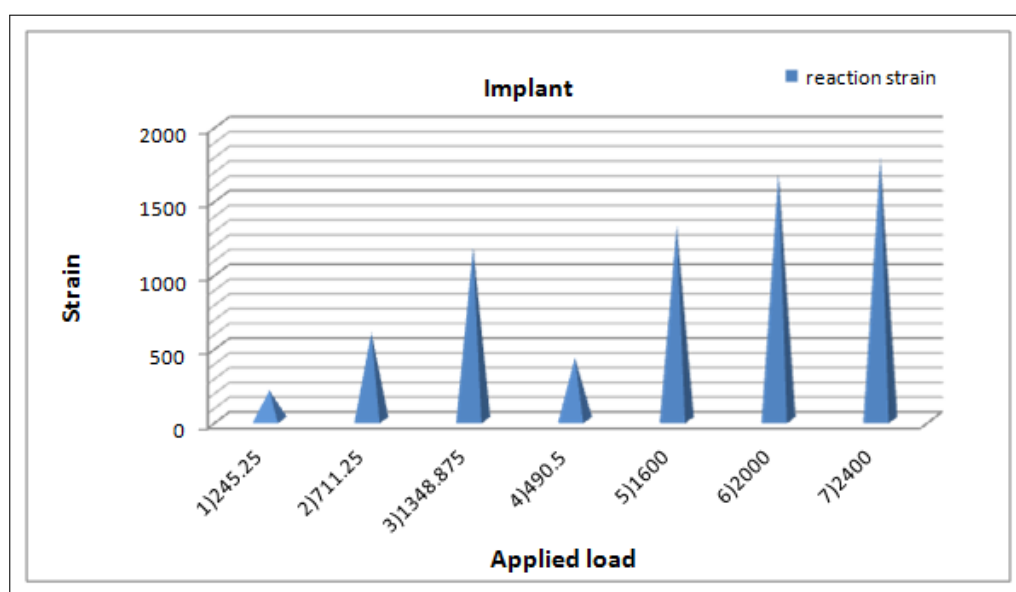


Figure 9: Graph depicting applied load versus reaction strain on hip joint for various gait phases 1. Two legged stance, 2. Terminal stance, 3. Heel strike, 4. Single legged stance, 5. Swing phase, 6. Initiation of fracture, 7. Load of fracture.

Different implant models are analyzed to identify the most optimal design. The first parameter considered, is the base cross section. Hexagon, pentagon, octal, and spherical surfaces are modeled to determine which cross section has a high load bearing capacity i.e. high Ultimate yield strength. Ultimate yield strength is defined as the maximum stress that a material can withstand while being stretched or pulled [13].

The second parameter considered is the bio-material used. Stainless steel 316L and UHMWPE, Ni-Ti alloy, Co-Cr alloy and Tantalum alloy are the chosen materials.

They are analyzed based on the parameter Modulus of Rigidity, which measures the stiffness of the material. It helps to determine how the material deforms elastically and withstands heavy loads. Higher the modulus of rigidity better the implant suitable for implant [13].

The third parameter considered is the geometrical dimension. Head diameter, neck diameter and neck angle of the implant model are varied and the stress distribution is observed. The various dimensions considered have been tabulated in Table 6.

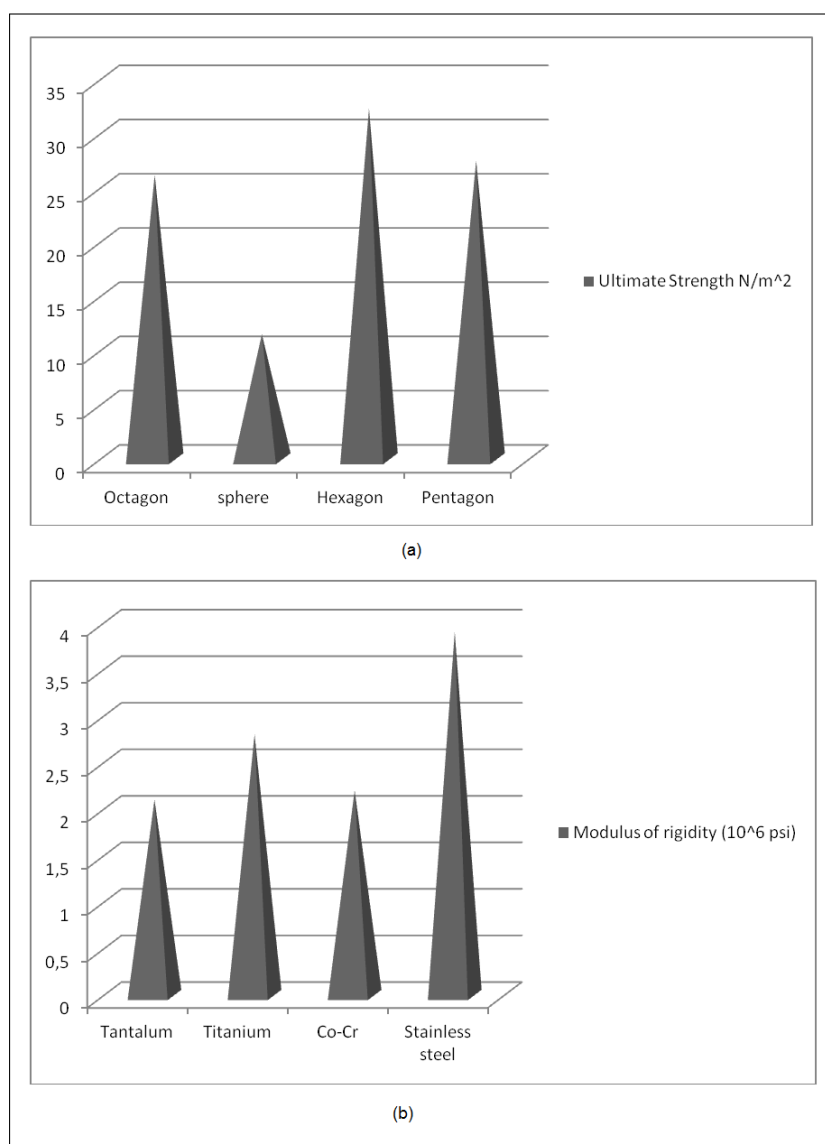


Figure 10: Graph depicting (a) the Ultimate Yield Strength for various base cross section (b) The Modulus Of Rigidity for various bio-materials.

3 Results

The model hip joint designed in CATIA proves to be a good representation of the femur geometry but it is not enough for further analysis. A more accurate method of modeling would be to reconstruct the femur bone from Computed Tomography scan data. The stress response can then be observed by actually inserting the implant into the bone as done during surgery.

According to analysis results shown in Figure 9, it is found that the initiation of fracture occurs at a load of 1600N and complete fracture occurs at 1600N and complete fracture occurs at 2000N. All other values are normal.

By analyzing the implants with above mentioned cross sections, it is found that hexagonal base cross section has better load bearing capacity with high Ultimate Yield Strength according to Figure 10(a). It has also been found

that stainless steel together with UHMWPE has the highest modulus of rigidity according to Figure 10(b).

Since it is known to be bio compatible, it is considered to be optimal.

While analysing the models with variant dimensions, it is found that the model no 2 as in Table 6 with head diameter 28mm, neck diameter 10mm, neck angle 128 degrees has minimum strain at the neck region with a value of 0.65 and found to be suitable for implant design.

The final optimized implant model that implements the above mentioned results is shown in Figure 13.

Analysis is performed on the optimized implant for the same gait phases to comparatively analyze it's strength with that of the femur. The results of this are shown in Figure 11.

From Figure 12, it is found that initiation of fracture in the implant occurs at 2000N and complete fracture occurs at 2400N.

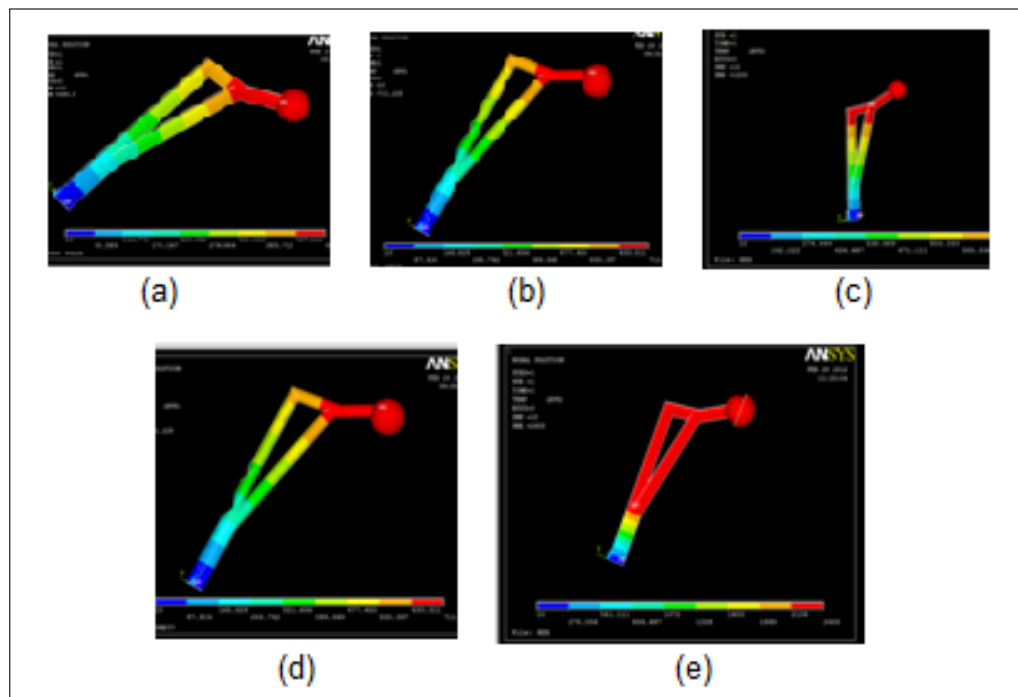


Figure 11: Depicts implant analysis for gait cycle phases (a) Two legged stance, (b) Heel strike, (c) single legged stance, (d) Swing phase, (e) Load of fracture.

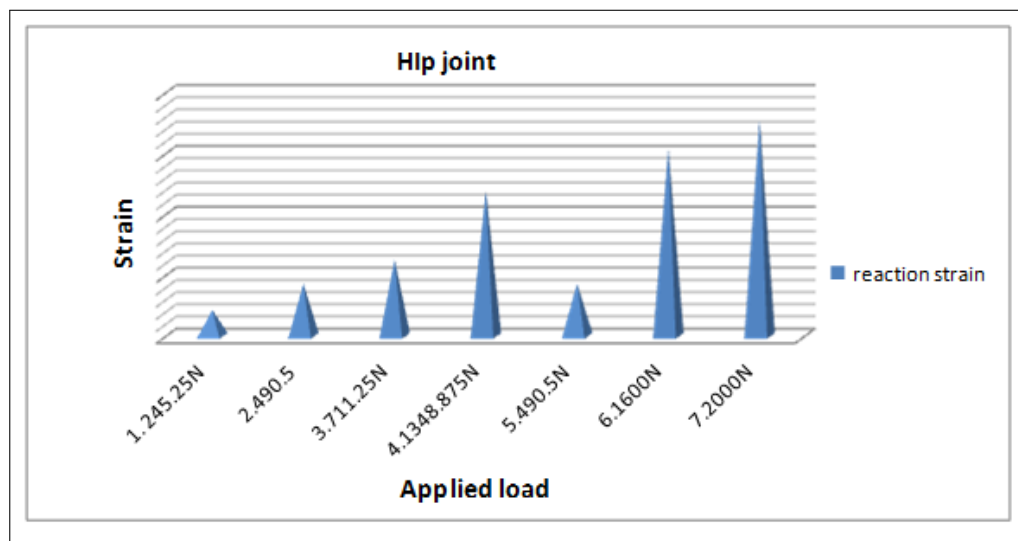


Figure 12: Graph depicting applied load versus reaction strain on the implant for various gait phase. 1. Two legged stance, 2. Terminal stance, 3. Heel strike, 4. Single legged stance, 5. Swing phase, 6. Initiation of fracture, 7. Load of fracture.

4 Conclusion and Discussion

It is found that the initiation of fracture occurs at a load of 1600N and complete fracture occurs at 2000N for the hip joint model, whereas for the optimized implant the fracture begins at 2000N and complete fracture occurs at 2400N. Hence the designed implant withstands better stress/load compared to the natural human hip joint. Distribution of stress and strain for various phases of gait is studied in both implant and the hip joint. It is found that most of the stress applied is withheld at the neck region

of the implant without distributing it to the entire stem portion of the implant.

The multi-disciplinary approach presented in this paper is found to be suitable for the evaluation of stress-strain behavior of both the hip joint and the prosthetic hip implant components. The results were in accordance with some previous data.

However, better results can be obtained if the bone is modeled directly from imaging modalities such as CT or MRI. Such models will be a better representation of the real human hip joint. This study provides a non destruc-

tive approach towards implant designing, but the actual effectiveness can be determined only through laboratory testing and clinical trials. Computer Analysis can also be improved by using accurate values when considering material properties. For example, the trabecular and cortical bone regions have not been considered separately. Also, by obtaining material properties from gray level values, patient specific analysis can be done. Considerations like frictional forces, anatomy of the joint and other surface properties have not been considered in this analysis.

Considering the drastic increase in hip fractures over the last few years, it is important to produce patient specific implants as hip fractures cause both loss of finances and loss of life.

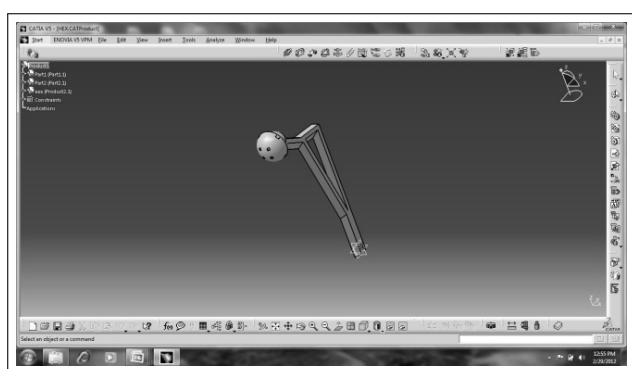


Figure 13: Optimized implant.

The 3D models are very useful in simulation of bone fractures and internal fixations with implants. In this work, the hip joint and implant model, developed in CATIA software, help to understand how these structures adapt to external forces disturbances²⁵. This will help the doctors to choose the optimal implant for a particular patient.

References

- [1] Andrew Edward Anderson, Computational Modeling Of Hip Joint Mechanics, The University of Utah, 2007.
- [2] Anthony L., TarunGowsami, Hip implants VII: Finite element analysis and Optimization of cross-sections, J. Materials and Design 29:1438–1446, 2008.
- [3] Alhassan S, Gowsami T, Wear rate model using UHMWPE in total hip and knee arthroplasty Mater. J. Materials and Design 29:289–96, 2010.
- [4] Bauer T.W, Schils J , The pathology of total joint arthroplasty and Mechanics of implant failure Skeletal Radiol, Skeletal Radiol. 28(9):483-97, 1999.
- [5] Blake Latham, GowsamiT, Effect of geometric parameters in the design of hip implants paper IV, J. Materials and Design 25:715–722, 2008.
- [6] WillmannGerd , Coating of Implants with Hydroxyapatite – Material Connections between Bone and Metal, Advanced Engineering Materials 1(2):5–105, 2007.
- [7] Kannus P, Parkkari J, Sievänen H, Epidemiology of hip fractures, The Johns Hopkins University School of Hygiene and Public Health, Cambridge University Press 19:244-48, 1997.
- [8] La Velle D G, Fractures of hip In: Campbell's Operative Orthopaedics, Mosby, Philadelphia 10:2873, 2003.
- [9] Huddleston J M, Whitford K J, Medical care of elderly patients with hip fractures, Mayo Clin Proc 76:295, 2001.
- [10] Mankin H J, The Reaction of Articular Cartilage to Injury and Osteoarthritis (Second of Two Parts), N Engl J Med 291:1335-40, 1974.
- [11] Jonathan Wickert, Kemper E. Lewis ,An Introduction to Mechanical Engineering, 345-401, 2000.
- [12] Dennis Jarvis ,Software Engineering And Manufacturing Systems For Case Tools, Chapman and Hall 28-29:302-307,1999.
- [13] SaeedMoaveni, Finite element analysis: theory and application with ANSYS, 3:105-117, 2007.
- [14] PaletiSrinivas, Sambana Krishna ChaitanyaDatti Rajesh Kumar, Finite Element Analysis Using Ansys 11.0, PHI Learning Pvt Limited 1:230-239, 2005.
- [15] Margareta Nordin, Victor Hirsch Frankel, Basic biomechanics of the musculoskeletal system, Lippincott William Wilkins 3:430-505, 2000.
- [16] BR Rawal, Rahul Ribeiro, Rajesh Malhotra, NareshBhatnagar, Anthropometric measurements to design best-fit femoral stem for the Indian population, Indian J Orthopedics46(1): 46-53, 2005.
- [17] SudeshSivasasu, Pearline Beulah, Lazar Mathew, Optimization Of Skeletal Hip Implant Cross-Sections, VIT University, 2008.
- [18] Bhatt Himanshu ,Finite Element Optimization Of Hip Implant Geometrical Parameters, North Gujarat University, 2006.

Computer Aided Segmentation and Classification of Mass in Mammographic Images using ANFIS

K. Yuvaraj¹, U.S. Ragupathy¹

¹ Department of Electronics and Instrumentation Engineering, Kongu Engineering College, Perundurai, Erode, Tamil Nadu, India

Abstract

Background: Breast cancer is one of the leading cancers in woman worldwide both in developed and developing nations as per the records from World Health Organization. Many studies have shown that mammography is very effective tool for the breast cancer diagnosis. Mass segmentation plays an important step for the cancer detection.

Objective: The objective of the proposed method is to segment the mass and to classify the mass with high accuracy.

Methods: The segmentation includes two main steps. First, a rough initial segmentation through iterative thresholding, and second, an active contour based segmentation.

The relevant statistical features are extracted and the classification is done by using Adaptive Neuro Fuzzy Inference System (ANFIS).

Results: The proposed mass detection scheme achieves sensitivity of 87.5% and specificity of 100% for a set of twenty two images. The overall segmentation accuracy obtained is 91.30%.

Conclusions: This work appears to be of high clinical significance since the mass detection plays an important role in diagnosis of breast cancer.

Keywords

ANFIS, classification, mammography, mass, segmentation

Correspondence to:

K. Yuvaraj

Department of Electronics and Instrumentation Engineering,
Kongu Engineering College,
Address: Perundurai, Erode, Tamil Nadu, India
E-mail: yuvarajkumarasamy@gmail.com

EJBI 2013; 9(2):37–41

received: January 16, 2013

accepted: April 4, 2013

published: August 30, 2013

1 Introduction

Over the past two decades, cancer has been one of the biggest threats to human life and it is expected to become the leading cause of death over the next few decades. A mammogram is an X-ray of the breast. One can diagnose at very early stage and hence there is a chance for healthy survival. Breast cancer can be traced from mammogram before it can be felt. When mammography is combined with clinical breast exam the chances for finding cancer are even greater. For women with dense breast tissue, digital mammography may be more accurate than standard mammography.

There are many other breast imaging tests that can provide valuable information [1], however, these find difficult to tell the difference between dense breast tissue, benign (non-cancerous) lumps and cancer. And, sometimes they miss tiny calcium deposits that are the earliest sign of a tumour. Thus mammogram plays as a vital tool in breast cancer detection and identification [2]. Mass is defined as space occupying lesion that is described by their shape and marginal properties. A benign is characterized by smooth margination, whereas a malignancy is

characterized by an indistinct border that becomes more spiculated with time.

Many researches were done to segment the mass in the mammograms [3, 4, 5]. Of which Active contour based segmentation provides the best way to segment the images whose background and foreground that are statistically different and homogeneous [6]. The contour based segmentation retains the original information of region, edge and shape of the mass [5] and [7].

The region based active contour [8] and [9] model holds good than the edge based contour model [10]. Considering all the above advantages of the region based active contour, the segmentation technique combines the classical segmentation technique with the region based active contour.

The rest of the paper is organized as follows. Section 2 details about the proposed method of mass segmentation. Section 3 discusses about the statistical features extraction and classification from the segmented images. Result and discussion are drawn in Section 4. Conclusion is produced in Section 5.

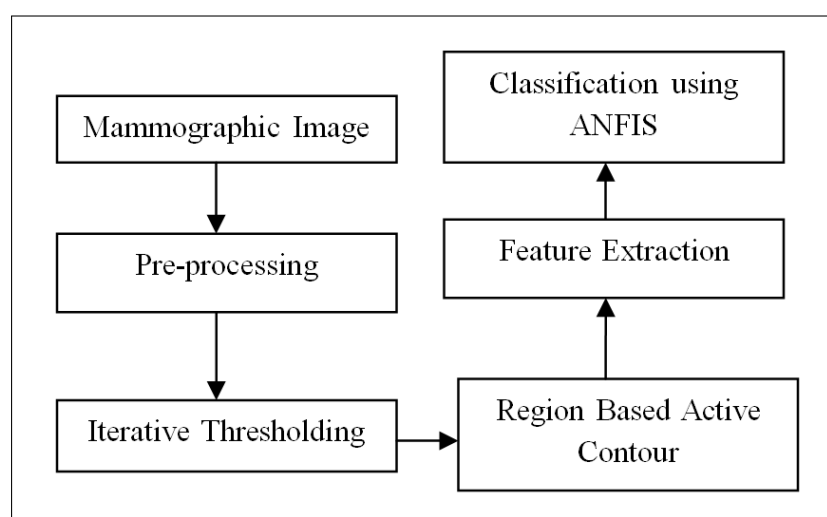


Figure 1: Block Diagram of the Proposed Mass Segmentation and Classification.

2 Proposed Method of Mass Segmentation

Mammographic images are collected from the Imaging centre, Coimbatore and from Mammographic Image Analysis Society (MIAS). The images are subjected to pre-processing which includes cropping (256 X 256) and enhanced by performing histogram equalization. Then the pre-processed image is subjected to iterative active contour based segmentation [11]. From the segmented image Gray Level Co-occurrence Matrix (GLCM) are formulated. Features are extracted from GLCM. These features are fed to the ANFIS for classification.

The block diagram of the proposed iterative active contour based segmentation and classification is shown in Figure 1. The result obtained in various stages of pre-processing are depicted in Figure 2.

The pre-processed image and the iterative thresholded image are shown in Figure 3 (a) and (b) respectively. The

average value of the maximum pixel and minimum pixel value of the pre-processed image is set as initial threshold value (T1). The value above T1 is set as foreground and the value below T1 as background. The total number of pixels in the foreground and the sum of all gray values of foreground is calculated. The total sum divided by the number of pixels gives the average value of foreground.

The above procedure is repeated for background. Then the average value of the foreground and the background is calculated (T2). If the value of T1 is equal to T2, then T2 is the final threshold value. If T1 is not equal to T2, then T1 is assigned with T2.

The segmentation technique involves initialization of the mask. The square mask of the size 111 x 111 is defined within the mass. This mask is allowed to deform until the minimum energy is encountered. Then, the binary segmented image is obtained.

Figure 4 shows the results obtained in various stages of segmentation. This is mapped with the gray scale pre-

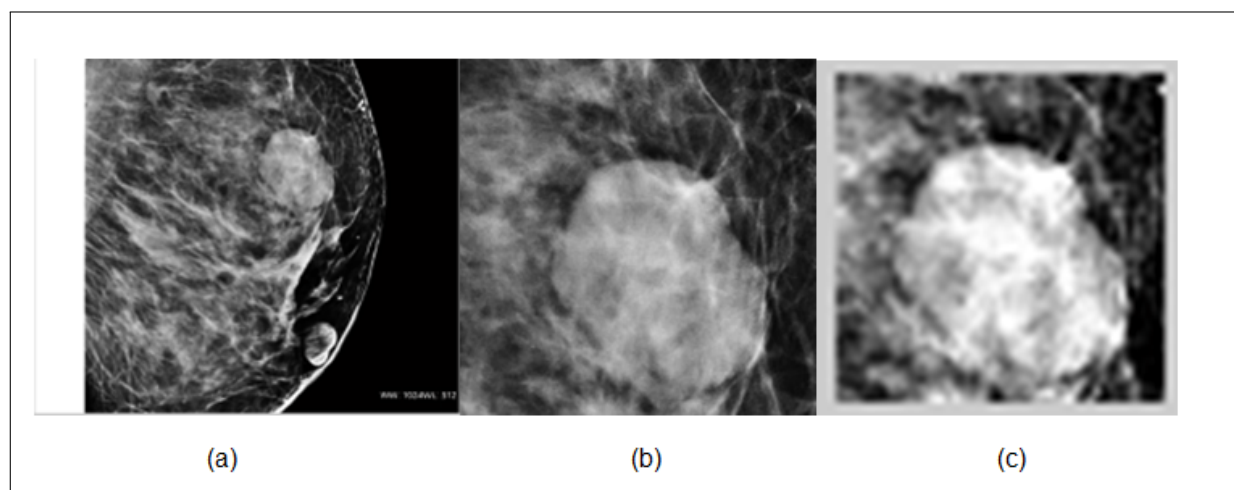


Figure 2: (a) Original Image, (b) Cropped Image and (c) Histogram Equalized Image.

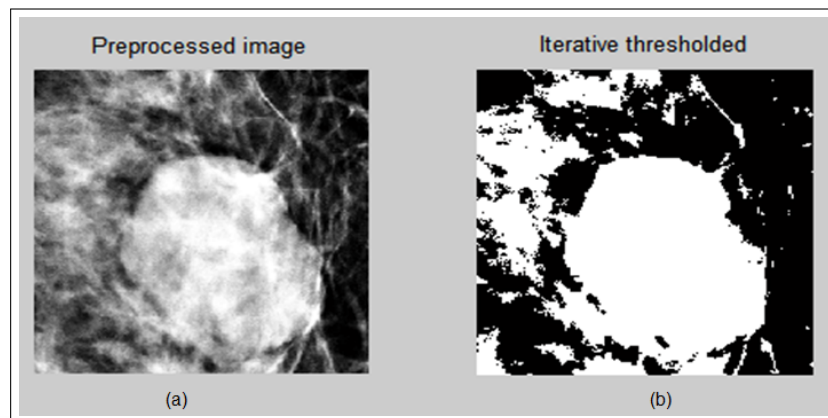


Figure 3: (a) Preprocessed Image and (b) Iterative Thresholded Image.

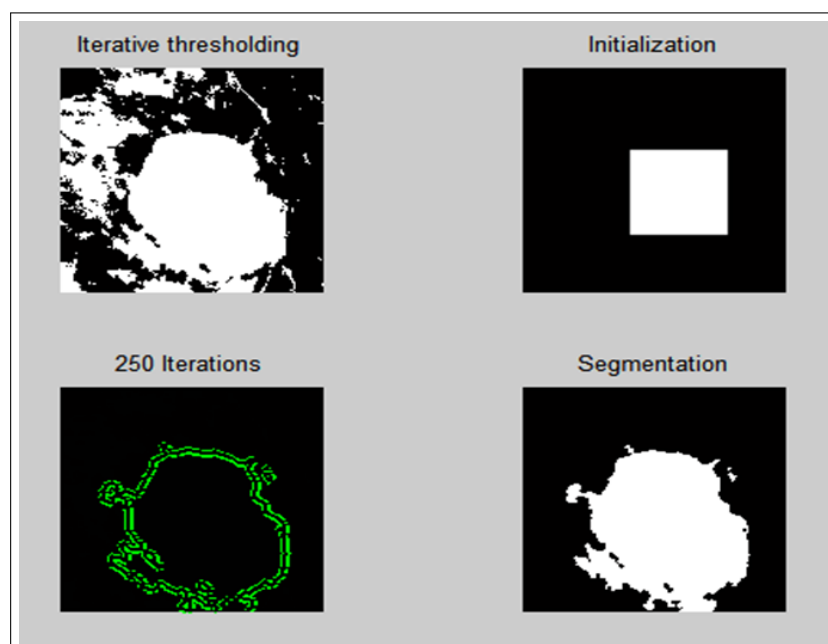


Figure 4: Image Results Obtained in Various Stages of Mass Segmentation.

processed image, and thus the gray level segmented image is obtained as shown in Figure 5.

This method of segmentation is preferred as it holds good when compared to the existing techniques like Fuzzy C Means based segmentation and Level set based segmentation [11].

3 Feature Extraction

From the gray level segmented image as shown in Figure 5 (b), GLCM are formulated. Initially four GLCM matrices are formulated for 0° , 45° , 90° and 135° orientations. The average of the above four matrix is formulated as resultant mean GLCM. From the formulated resultant mean GLCM sixteen statistical features are extracted and are listed in Table 1. From these sixteen features the optimal features are obtained by calculating the variance and the features with higher value of variance are selected and

are shown in Table 2. These include Contrast, Dissimilarity, Sum average, Sum variance and Auto correlation [12]. For the remaining eleven features since the variance is much lower (approximately equal to zero) and these features are neglected.

4 Result and Discussion

The statistical features are extracted from 61 images. Table 3 illustrates the number of images considered for training and testing ANFIS classifier. Number of training samples considered are 39. For testing 22 samples are considered. The membership functions are used to convert the input values into fuzzy values. Various types of membership function is used which includes triangular, trapezoidal, generalised bell, gaussian and gaussian2. Among which the testing error for the triangular membership function is 0.4603 which is lesser when compared with

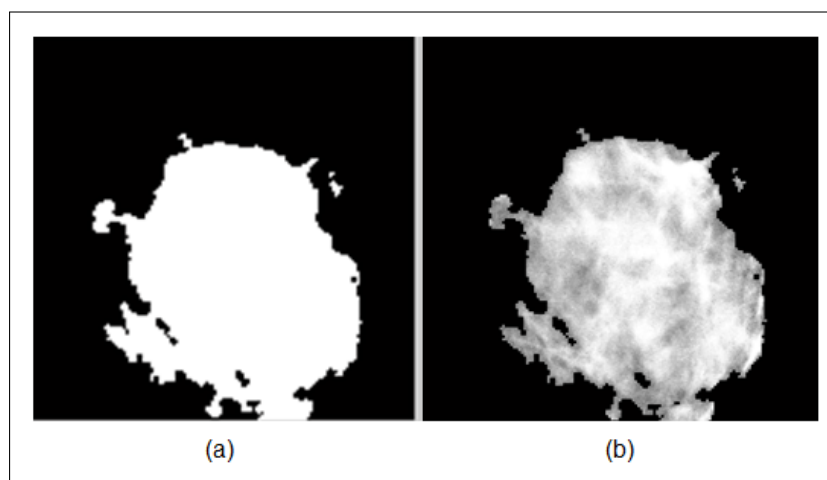


Figure 5: (a) Binary Segmented Image and (b) Gray Level Segmented Image.

other membership functions (0.5701-trapezoidal, 1.1941-gbell, 0.8864-gaussian, and 1.483-gaussian2).

Table 2: Sample Features Extracted.

Features Image Category	Normal mdb047	Benign mdb025	Malignant mdb264
Contrast	0.3658	0.3125	0.7847
Dissimilarity	0.0550	0.0446	0.1202
Sum average	7.4156	7.0528	7.1306
Sum variance	97.8043	93.1580	92.7942
Auto correlation	34.1819	32.5812	32.6761

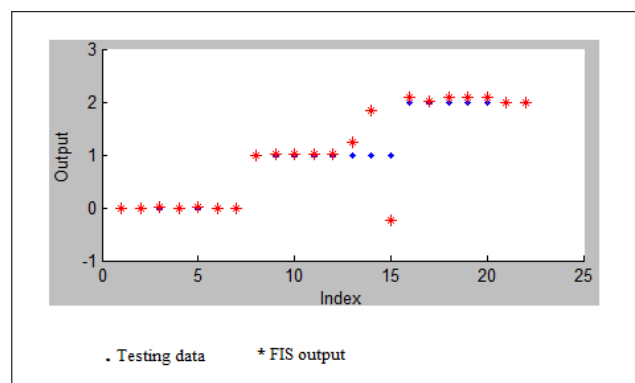


Figure 6: ANFIS-Classification Plot.

Table 1: Feature Selection from GLCM.

Feature Reduction Feature Extracted from GLCM	Normal mdb123 (x)	Benign mdb69 (y)	Malignant mdb267 (z)	Mean $M = (x + y + z)/3$	Variance $ ((M - x) + (M - y) + (M - z))/3 $
Contrast	0.3806	0.4526	0.0732	0.2988	0.18
Correlation	-1.3026	-1.2566	-1.2613	-1.2735	0.0194
Dissimilarity	0.0568	0.0709	1.0459	0.3904	0.4378
Energy	0.5347	0.4869	0.4844	0.502	0.01228
Entropy	-0.4232	-0.3958	-0.3939	-0.4043	0.0117
Homogeneity	0.9922	0.9894	0.9869	0.9895	0.0054
Maximum Probability	0.6438	0.4977	0.5036	0.5483	0.0636
Sum average	9.0698	6.9194	7.1435	7.7109	1.0859
Sum variance	120.6634	90.7037	93.4084	101.5918	12.7143
Sum entropy	0.3298	0.4143	0.4213	0.3884	0.039
Difference variance	0.3806	0.4526	0.6032	0.4758	0.0789
Difference entropy	0.0618	0.0866	0.0990	0.0824	0.0138
Information measure of correlation	0.9844	0.9868	0.9867	0.9859	0.0010
Inverse difference normalized	0.9961	0.9950	0.9936	0.9949	0.0008
Inverse difference moment normalized	0.9966	0.9959	0.9945	0.9956	0.0005
Auto correlation	41.6196	31.8959	32.8250	35.4478	4.1145

Hence triangular membership function is chosen. For each input three triangular membership functions are used. Total number of rules framed is 729. The classification result obtained through ANFIS is shown in the Figure 6.

Table 3: Mass classification Result by ANFIS.

Image Category	No. of training images	No. of testing images	Error
Normal	16	7	0
Benign	13	8	2
Malignant	10	7	0

With the information available from Table 3, sensitivity, specificity and overall accuracy of the proposed classification system are calculated by using the equations (1), (2) and (3) respectively. These are used as performance metrics for the classification. The values are tabulated in Table 4.

$$\text{Sensitivity} = \frac{\text{Number of true positive decisions}}{\text{Number of actual positive cases}} \times 100 \quad (1)$$

$$\text{Specificity} = \frac{\text{Number of true negative decisions}}{\text{Number of actual negative cases}} \times 100 \quad (2)$$

$$\text{Accuracy} = \frac{\text{Number of correct decisions}}{\text{Total number of cases}} \times 100 \quad (3)$$

Table 4: Performance Metrics of the Classifier.

Metrics	Value (%)
Sensitivity	87.5
Specificity	100
Accuracy (Overall)	91.30

The sensitivity obtained is 87.5%, the specificity obtained is 100% and the overall classification accuracy obtained through ANFIS is 91.30%.

5 Conclusion

In this paper a new computer aided mass segmentation and classification scheme is proposed. Five statistical features were selected for the classification of mass. The classification is done by using ANFIS. The implementation of the proposed method was carried out using MATLAB. Result shows that the suggested features can give acceptable accuracy for the classification of mass. The result

shows that the overall accuracy is 91.30%. With increase in the number of test samples the accuracy may still be improved to a great extent.

References

- [1] Kuo H C, Giger M, Reiser I, Boone J, Lindfors K, Yang K. Handbook of Breast Imaging. 2012; 697-704.
- [2] Samir Kumar Bandyopadhyay. Survey on Segmentation Methods for Locating Masses in a Mammogram Image. An International Journal of Computer Applications, Article 6. 2011; 9(11):25-28.
- [3] Sahiner B, Petrick N, Chan H P, Hadjiiski LM, Paramagul C, Helvie MA, Gurcan MN. Computer-Aided Characterization of Mammographic Masses: Accuracy of Mass Segmentation and its Effects on Characterization. IEEE Transaction on Medical Imaging. 2001; 20(12): 1275-1284.
- [4] Sahiner B, Chan H P, Petrick N, Helvie M A, Hadjiiski LM. Improvement of Mammographic Mass Characterization using Spiculation Measures and Morphological Features. Medical Physics. 2010; 18(7): 1455-1465.
- [5] Jun Liu, Jianxun Chen, Xiaoming Liu, Lei Chun2, Jinshan Tang1, Youping Deng. Mass Segmentation using a Combined Method for Cancer Detection. An International Conference on Bioinformatics and Computational Biology. 2010; 5(3):S6.
- [6] Peyman Rahmati A, Andy Adler A, Ghassan Hamarneh B. Mammography Segmentation with Maximum Likelihood Active Contours. An International Journal on Medical Image Analysis. 2012; 16(6): 1164-1186.
- [7] Thiruvankadam, Acharyya, Neeba, Jhunjhunwala, Ranjan S. A Region Based Active Contour Method for Extraction of Breast Skin line in Mammograms. An International Conference on Medical Imaging: from Nano to Macro. 2010;189-192.
- [8] Bhagwati Charan Patel, Sinha GR. Energy and Region based Detection and Segmentation of Breast Cancer Mammographic Images. An International Journal of Image, Graphics and Signal Processing. 2012; 6(2): 44-51.
- [9] Alierza Vard, Kamal Jamshidi, Naser Movahhedinia. Small Object Detection in Clustered Image using Correlation based Active Contour Model. Journal on Pattern Recognition Letters. 2012; 33(5): 543-553.
- [10] Yu Zhang, Noriko Tomuro, Jacob Furst, Daniela Stan Raicu. Image Enhancement and Edge-based Mass Segmentation in Mammogram. Proceedings of Medical Imaging 2010: Image Processing. 2010; 7623:76234P-76234P-8
- [11] Yuvaraj K, Ragupathy U S. Mammographic Mass Segmentation based on Iterative Active Contours. Proceedings of Biomedical Systems, Signals and Images (BSSI 2012) 2012.
- [12] Andrew F. Laine, Sergio Schuler, Jian Fan and Walter Huda. Mammographic Feature Enhancement by Multiscale Analysis. An International Conference on Medical Imaging. 1994; 13(4):725-740.

Comparison of Intelligent Computing Techniques for Classification of Clinical EEG Signals

D. Najumnissa¹, T.R.Rangaswamy¹

¹ Department of Electronics and Instrumentation Engineering B.S.Abdur Rahman University, India

Abstract

Objective: The objective of this work is to develop efficient classification systems using intelligent computing techniques for classification of normal and abnormal EEG signals.

Methods: In this work, EEG recordings were carried out on volunteers (N=170). The features for classification of clinical EEG signals were extracted using wavelet transform and the feature selection was carried out using Principal Component Analysis. Intelligent techniques like Back Propagation Network (BPN), Adaptive Neuro-Fuzzy Inference System (ANFIS), Particle Swarm Optimization Neural network (PSO) and Radial Basis function Neural network (RBFNN) were trained for diagnosing seizures. Further, the performance of the developed classifiers was compared.

Results: Results demonstrate that RBFNN classifies normal and abnormal EEG signals better than the other methods. It appears that the RBFNN is able to detect Generalized Tonic-Clonic Seizure (GTCS) more efficiently than the Complex Partial Seizures (CPS). Positive predictive value was better in PSO and ANFIS than BPN method.

Conclusions: It appears that the combination of Wavelet transform method and PCA derived features along with RBFNN classifier is efficient for automated EEG signal classification.

Keywords

Epileptic seizure, wavelet transform, intelligent classification systems

Correspondence to:

D. Najumnissa

B.S.Abdur Rahman University

Address: GST, Road, Vandalur, Chennai 600048, India

E-mail: najumnissa.d@bsauniv.ac.in

EJBI 2013; 9(2):42–51

received: January 16, 2013

accepted: March 29, 2013

published: August 30, 2013

1 Introduction

Infections are important cause of epilepsy in developing countries, the frequency of which may differ widely in different locations. Viral, bacterial, fungal and parasitic infections can result in epilepsy [1, 2]. For example, the cytomegalovirus produces typical encephalitis with fever, headache and seizures. Cytomegalovirus can cause seizures in 4% to 11% of HIV patients. Herpes simplex virus is a DNA virus that causes the most common form of sporadic fatal encephalitis in children older than six months and adults worldwide [1]. A seizure complication of infection can consist of a single seizure or can go on to become chronic epilepsy. Epilepsy is a neurological disorder characterised by recurring seizures. Like many other neurological disorders epilepsy can be assessed by electroencephalograms (EEG) [3]. EEG signals are difficult to characterise since they are non-stationary and highly non-linear. Since seizures occur irregularly and unpredictably, automatic seizure detection in EEG recordings is highly required [4].

Significant diagnostic information can be obtained from the frequency distribution of epileptic EEG. A

method such as the wavelet transforms (WT) is powerful for extraction of diagnostic information from clinical EEG signals [5]. WT is also appropriate for analysis of non-stationary signals, and hence it is suitable for locating transient events. The features extracted using WT can be used to analyze various transient events in biological signals. Recently, work on time-frequency analysis of EEG signals for detecting seizures using WT has been reported [5, 6, 7, 8, 9]. Principal component analysis, or PCA, is a technique that is widely used for applications such as dimensionality reduction, lossy data compression, feature extraction, and data visualization. PCA is a statistical method used to transform the input space into a new lower dimensional space. PCA technique has been investigated before by researchers for signal and image processing [10].

Neural networks are routinely employed in signal classification systems [11, 12, 13]. Fuzzy sets have attracted the growing attention and interest in modern information technology, production technique, decision making, pattern recognition, diagnostics, data analysis, etc. [14, 15]. In recent years, the integration of neural networks and fuzzy logic has given birth to new research into Neuro-

fuzzy systems. As a result, those systems can utilize linguistic information from the human expert as well as measured data during modeling. Such applications have been developed for signal processing, automatic control, information retrieval, database management and data classification [16, 17, 18, 19, 20, 21]. Successful implementations of ANFIS in biomedical engineering have been reported, for classification [10, 16, 18], for modeling and controlling real systems [21] and data analysis [22]. Particle swarm optimization (PSO) is an evolutionary optimization technique motivated by the simulation of social behavior [23].

Radial basis function (RBF) neural networks are good at modeling nonlinear data and can be trained in one stage rather than using an iterative process as in multilayer perceptron and also learn the given application quickly. Enrico [24] surveyed the different interpretations of radial basis function neural networks in order to emphasize their relevant properties and concluded that medical applications usually used radial basis function neural networks. Recently, there is a growing interest in the use of RBFNN for its short training time and being guaranteed to reach the global minimum of error surface during training [25]. There are several reports regarding the use of RBFNN for solving classification problems [26, 27, 28, 29]. Additionally, this network is inherently well suited for classification, because it naturally uses unsupervised learning to cluster the input data [30, 31].

This paper aims to extract features from EEG signals using WT and feature selection is performed using PCA. Further, classification systems for diagnosis of normal and abnormal EEG signals have been developed using ANFIS, PSONN and RBFNN techniques.

2 Methodology

This paper will focus on an automatic diagnosis system to classify the normal and epileptic seizure EEG signals. This system consists of two stages. The first stage is the feature extraction from EEG signals and the second stage is the classification of EEG signals based on the computed features. Figure 1 shows the block diagram of the proposed methodology.

In this work, EEG recordings are carried out on volunteers (N=170). This dataset includes 60 subjects diagnosed as normal, 60 subjects diagnosed with generalized tonic clonic seizures and 50 subjects diagnosed with com-

plex partial seizures. The typical normal and abnormal EEG signals are shown in Figures 2, 3 and 4.

2.1 Subjects and Data Recording

Subjects within the age group of 21 to 40 were selected for this study. The EEG was collected using Nihon Kohden digital EEG system comprising of a data acquisition system, signal processor and a personal computer from Sri Ramachandra Medical University and Research Institute, Chennai. The 10 second scalp EEG data used in this study was sampled at a rate of 500 Hz after filtering between 1 and 70 Hz. A bipolar electrode montage of 16 channels was used in the analysis. The EEGs were recorded with Ag/AgCl electrodes placed at the F₄, C₄, P₄, O₂, F₃, C₃, P₃, O₁, Fp₂, F₈, T₄, T₆, Fp₁, F₇, T₃, and T₅, loci of the 10–20 International System. Impedance was kept below 5 k Ω to avoid polarization effects. All data were stored for off-line processing. All EEGs with artifact, electrode movement and bursts of alpha waves were discarded.

2.2 Visual Inspection and Validation

Two EEG technologists with experience in the clinical seizure EEG signals separately inspected every recording included in this study to score clinical seizure and normal signals. The two experts revised the signals together to solve disagreements and set up the training set for the development of the classification systems. They also examined each recording completely for epileptic seizures. This validated set provided the reference evaluation to estimate the performance of the classifiers.

2.3 Wavelet Analysis and Feature Extraction

2.3.1 Artifact Removal from EEG Signals

The presence of artifacts in the signals is one of the major difficulties in analysis of EEG signals. This nature of disturbance is a serious obstructing factor that prohibits further processing to identify useful diagnostic features. Artifacts in EEG are commonly handled by discarding the affected segments of EEG. The simplest approach is to discard a fixed length segment, perhaps one second, from

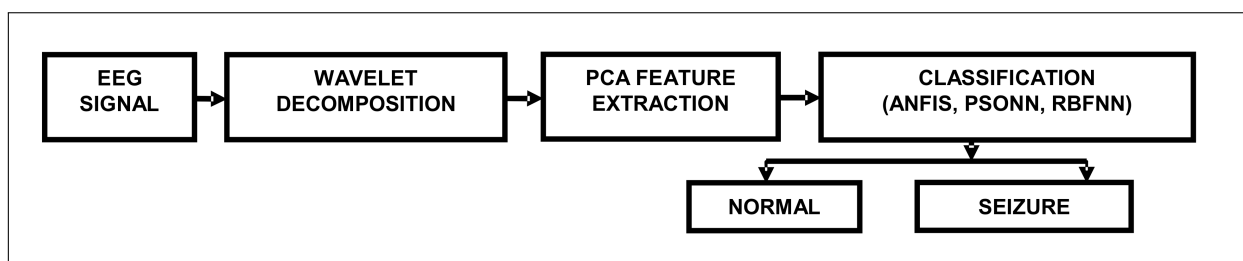


Figure 1: Schematic of the EEG signal classification system.

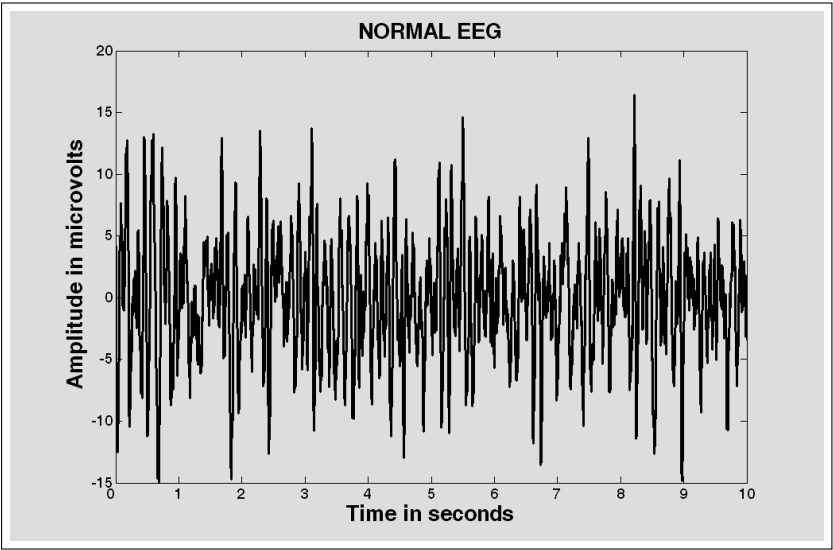


Figure 2: Normal EEG signal.

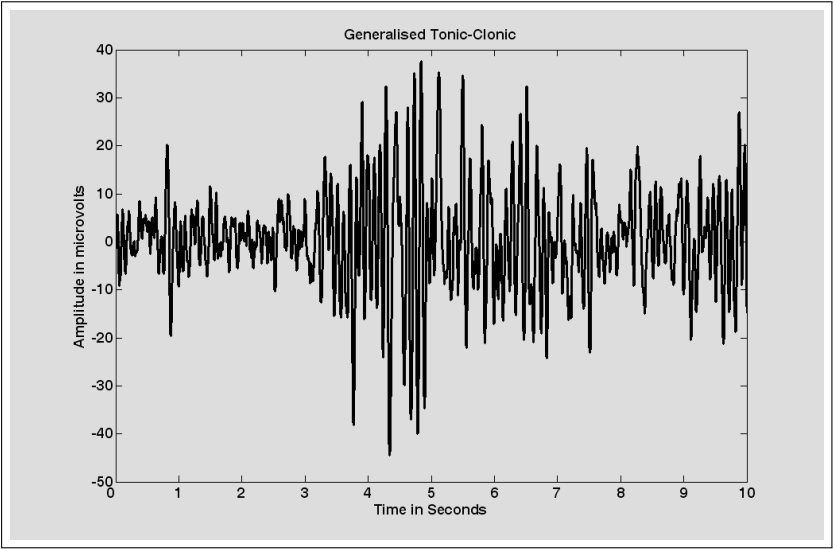


Figure 3: Generalised tonic-clonic seizure EEG signal.

the time an artifact is detected. Discarding segments of EEG data with artifacts can greatly decrease the amount of data available for analysis. Since the frequency bands of these noises may overlap with the seizure signal, conventional method of using filters was not suitable for removal of noise. In this work, DWT based denoising technique, namely wavelet shrinkage denoising was used [31].

2.3.2 Multiresolution Decomposition of EEG Signals

The Discrete Wavelet Transform (DWT) is a versatile signal processing tool that analyzes the signal at different frequency bands, with different resolutions by decomposing the signal into a coarse approximation and detail information [32]. We visually inspect the data first, and if the data is discontinuous, Haar or other sharp wavelet functions are applied [33] or else a smoother wavelet can

be employed. Usually, tests are performed with different types of wavelets and the one which gives maximum efficiency is selected for the particular application.

Table 1: Frequencies corresponding to different levels of decomposition.

Decomposed signal	Frequency range (Hz)
D1	125 – 250
D2	62.5 – 125
D3	31.25 – 62.5
D4	15.625 – 31.25
D5	7.8125 – 15.625
D6	3.9063 – 7.8125
D7	1.9531 – 3.9063
D8	0.9766 – 1.9531
A8	0 – 0.9766

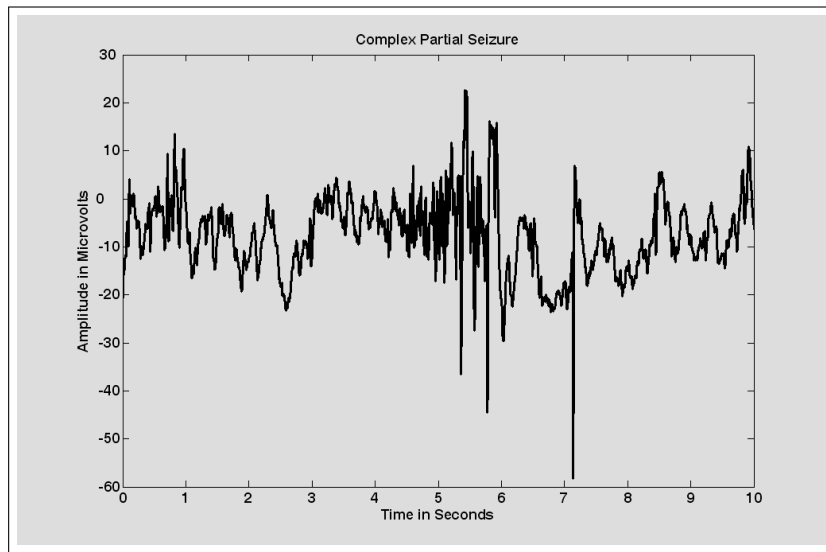


Figure 4: Complex partial seizure EEG signal.

In this study Quadratic spline wavelet is chosen. The levels are chosen such that those parts of the signal that correlate well with the frequencies required for classification of the signal are retained in the wavelet coefficients. Since the EEG signals do not have any useful frequency components above 30 Hz, the number of levels was chosen to be 8. Thus the signal is decomposed into the details D1–D8 and one final approximation, A8 [27]. The ranges of various frequency bands are shown in Table 1.

2.3.3 Feature Extraction

The extracted wavelet coefficients provide a compact representation that shows the energy distribution of the signal in time and frequency. It is anticipated that the coefficients of the seizure frequency spectrum ranges from 0.5 to 30 Hz. So the coefficients corresponding to the frequency bands, D1–D3 were discarded, thus reducing the number of feature vectors representing the signal. In order to further reduce the dimensionality of the extracted feature vectors, Gotman [34] features and some statistical features are used from the wavelet coefficients. These feature vectors, calculated for the frequency bands D4–D8 and A8, is used for classification of the EEG signals.

2.4 Intelligent Computing Techniques

2.4.1 Adaptive Neuro-Fuzzy Inference system (ANFIS)

ANFIS was first introduced by Jang in 1993 [20]. It is a model that maps inputs through input membership functions (MFs) and associated parameters, and then through output MFs to outputs. We consider one degree of Sugeno's function [18] that is adopted to depict the fuzzy rule. Hence, the rule base will contain two fuzzy if-then rules as shown in equations (1) and (2):

$$\text{Rule 1 : if } x \text{ is } A_1 \text{ and } y \text{ is } B_1 \text{ then } f = p_1x + q_1y + r_1. \quad (1)$$

$$\text{Rule 2 : if } x \text{ is } A_2 \text{ and } y \text{ is } B_2 \text{ then } f = p_2x + q_2y + r_2. \quad (2)$$

where x and y are the inputs, A_i and B_i are the fuzzy sets, f_i are the outputs within the fuzzy region specified by the fuzzy rule, p_i , q_i and r_i are the design parameters that are determined during the training process.

2.4.2 Particle Swarm Optimization Neural Network (PSO NN)

The PSO algorithm is a population based search algorithm based on social behavior of birds within a flock. A swarm consists of a set of 'N' particles where each particle represents a potential solution. Particles are then flown through the hyperspace, where the position of each particle is changed according to its own experience and that of its neighbors.

In the original formulation of PSO [23], each particle is defined as a potential solution to the problem in a D-dimensional space and each particle maintains a memory of its previous best position. The particle position with the highest fitness value for the entire run is called the global best.

At each of the iteration the velocity vector (V_i) of particle is adjusted based on its best solution and the best solution of its neighbors. The position (x_i) of the velocity adjustment made by the particle's previous best position is called the cognition component and the position of the velocity adjustments using the global best is called the social component. The PSO equations described in [21] are

$$V_i(t+1) = wV_i(t) + c_1r_1(\dots) * (p_i d(t) - x_i d(t)) + c_2r_2(\dots) * (pgd(t) - x_i d(t)) \quad (3)$$

$$x_i d(t+1) = x_i d(t) + V_i d(t) \quad (4)$$

where w is the inertia weight, c_1 and c_2 are positive acceleration constants. The velocity vector drives the optimization process and reflects socially exchanged information.

2.4.3 Radial Basis Function Neural Network (RBFNN)

The radial basis function network (RBFN) is a multilayer feed forward neural network, which consists of an input layer of source nodes, a layer of non linear hidden units that operate as kernel nodes and an output layer of linear weights. In response to an input vector, the outputs of the hidden layer are linearly combined to form the network response that is processed with a desired response to the output layer. The weights are trained in a supervised fashion using an appropriate linear method [35]. An activation function for a hidden layer node is a locally radial symmetric function.

2.5 Performance Analysis

The performance of the developed classifiers was estimated using False Positive (FP), False Negative (FN), True Positive (TP) and True Negative (TN) values [10]. Classification of a normal data as abnormal is considered

as FP and classification of abnormal data as normal is considered FN. TP and TN are the cases where the abnormal is classified as abnormal and normal is classified as normal respectively. The accuracy, sensitivity, specificity, positive predictive value and negative predictive value were estimated using the following relations as shown in equations:

$$\text{Accuracy} = (TP + TN) / (TP + FP + TN + FN) \quad (5)$$

$$\text{Sensitivity} = TP / (TP + FN) \quad (6)$$

$$\text{Specificity} = TN / (TN + FP) \quad (7)$$

$$\text{False Positive Rate} = FP / (TN + FP) \quad (8)$$

$$\text{Positive Predictive Value} = TP / (TP + FP) \quad (9)$$

$$\text{Negative Predictive Value} = TN / (TN + FN) \quad (10)$$

Accuracy is the representation of classifier performance in global sense. Sensitivity and specificity are the proportions of abnormal data classified as abnormal, normal data classified as normal respectively.

3 Results and Discussion

The EEG signals were decomposed into details D1–D8 and one final approximation A8 using wavelet transforms. The features like energy, entropy, Hurst exponent, Largest

Table 2: Descriptive statistics of the decomposition level 6.

Sl. No	D6 Feature	Normal (60)	GTC (60)	CPS (50)	p-value
		Mean \pm SD	Mean \pm SD	Mean \pm SD	
1	Energy	0.13 \pm 0.08	0.07 \pm 0.001	0.06 \pm 0.01	0.0006
2	Max	0.15 \pm 0.06	0.17 \pm 0.107	0.16 \pm 0.14	0.0001
3	Min	0.50 \pm 0.19	0.30 \pm 0.209	0.17 \pm 0.16	0.0195
4	Mean	-0.15 \pm 0.001	0.03 \pm 0.03	0.02 \pm 0.001	0.0032
5	Standard deviation	0.35 \pm 0.12	0.19 \pm 0.11	0.17 \pm 0.13	0.0055
6	Variance	0.14 \pm 0.09	0.07 \pm 0.009	0.06 \pm 0.009	0.0008
7	Hurst	0.94 \pm 0.02	0.94 \pm 0.02	0.91 \pm 0.03	0.0198
8	Entropy	0.13 \pm 0.02	0.08 \pm 0.012	0.095 \pm 0.014	0.0003
9	Pyy	0.24 \pm 0.21	0.05 \pm 0.02	0.03 \pm 0.004	0.0056
10	Freq At Pyy	0.71 \pm 0.13	0.70 \pm 0.11	0.70 \pm 0.11	0.0011
11	LLE	0.93 \pm 0.02	0.91 \pm 0.03	0.90 \pm 0.04	0.0102

Table 3: Descriptive statistics of the decomposition level 7.

Sl. No	D7 Feature	Normal (60)	GTC (60)	CPS (50)	p-value
		Mean \pm SD	Mean \pm SD	Mean \pm SD	
1	Energy	0.07 \pm 0.06	0.05 \pm 0.01	0.05 \pm 0.002	0.0136
2	Max	0.14 \pm 0.07	0.16 \pm 0.12	0.10 \pm 0.08	0.0171
3	Min	0.43 \pm 0.22	0.31 \pm 0.26	0.18 \pm 0.17	0.0107
4	Mean	-0.08 \pm 0.03	0.01 \pm 0.01	0.04 \pm 0.02	0.0013
5	Standard deviation	0.23 \pm 0.09	0.14 \pm 0.09	0.14 \pm 0.11	0.0013
6	Variance	0.07 \pm 0.07	0.07 \pm 0.01	0.05 \pm 0.004	0.0001
7	Hurst	0.95 \pm 0.01	0.96 \pm 0.01	0.95 \pm 0.02	0.0059
8	Entropy	-0.04 \pm 0.02	0.05 \pm 0.009	0.106 \pm 0.015	0.0019
9	Pyy	0.10 \pm 0.10	0.05 \pm 0.03	0.03 \pm 0.001	0.0005
10	Freq At Pyy	0.79 \pm 0.15	0.80 \pm 0.16	0.81 \pm 0.16	0.0008
11	LLE	0.89 \pm 0.03	0.88 \pm 0.04	0.78 \pm 0.04	0.0507

Lyapunov exponent (LLE), maximum power of the spectrum, frequency at which maximum power exists and statistical features like mean, standard deviation, maximum and minimum of the coefficients and variance were extracted. Totally 55 features were extracted for each subject. The statistical analysis on the extracted features such as mean and standard deviation for level D6 and D7 is shown in Table 2 and Table 3.

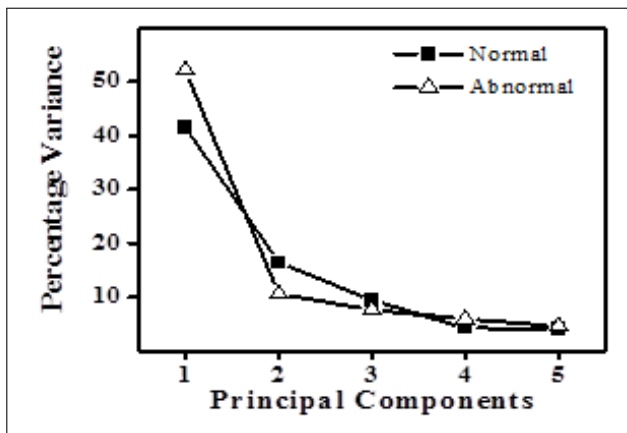


Figure 5: Percentage variance for normal and abnormal subjects for Quadratic Spline Wavelet.

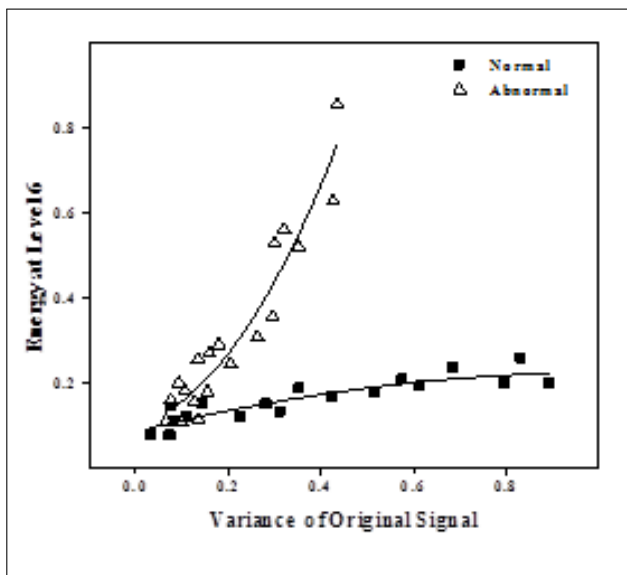


Figure 6: Variation in Energy for both normal and abnormal EEG at D6.

PCA based choice of wavelets and feature extraction: PCA was applied for selection of wavelet and feature reduction. The original feature space consists of 55 EEG features which included frequency domain features, the statistical features and the nonlinear features obtained from normal and clinical seizure subjects from the different types of wavelets like Haar, db2, db4, db5 and quadratic spline. Some of the methods like Correlation-based Feature Selection [36], Chi-square Feature Evaluation [36] does not perform feature selection but only feature ranking, and they are usually combined with another

method when one needs to find out the appropriate number of attributes. PCA is used to make a classifier system more effective, having less computational complexity, and less time consumption. Hence the dataset obtained from the EEG containing 55 parameters for five types of wavelets were subjected to PCA. The Principal Components obtained from PCA were analyzed for ranking the most significant wavelet and features. When PCA was applied, it was observed that the features derived out of quadratic spline wavelet had the maximum variance than the other wavelets used. The percentage variance of the extracted features of normal and abnormal subjects for the quadratic spline wavelet is plotted in Figure 5. Hence quadratic spline wavelet features were considered for further analysis.

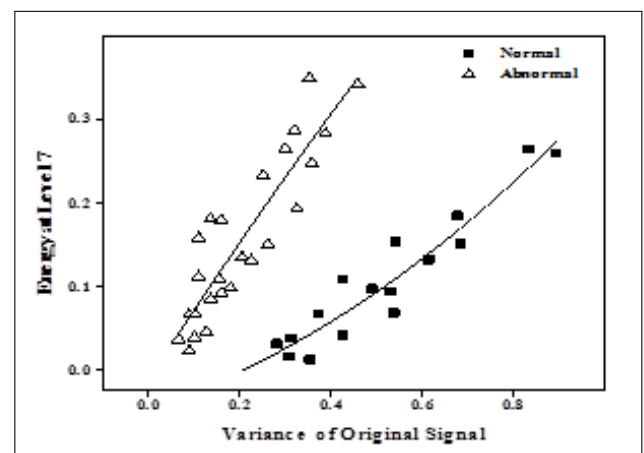


Figure 7: Variation in Energy for both normal and abnormal EEG at D7.

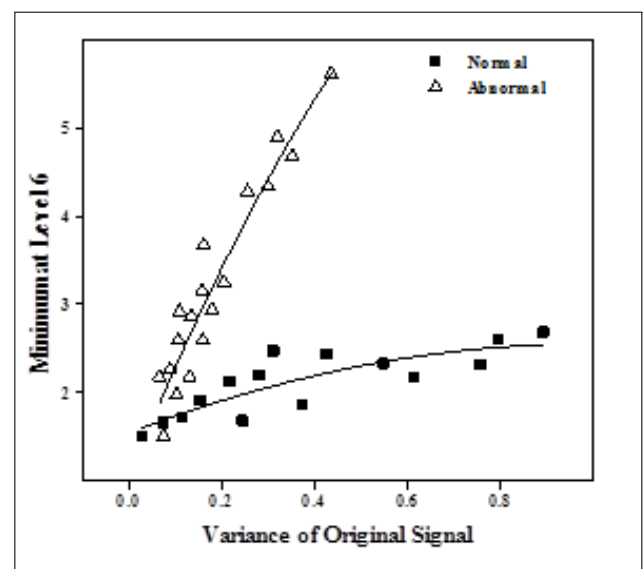


Figure 8: Variation in Minimum for both normal and abnormal EEG at D6.

Qualitative assessment of features: One of the simplest linear statistics that may be used for investigating the dynamics underlying the clinical EEG is the variance

of the signal calculated in consecutive non overlapping windows. The various features obtained from the wavelet decomposition were correlated with the variance of the original signal. It was observed from Table 4 that at level D4, D5 and at D8, there were poor correlation values for normal and abnormal features. In level D6 and D7 the correlation of certain features with variance was higher than the other levels of decomposition. The Features like energy, minimum, standard deviation and the entropy of DWT coefficients have very high correlation with high significance ($p < 0.001$).

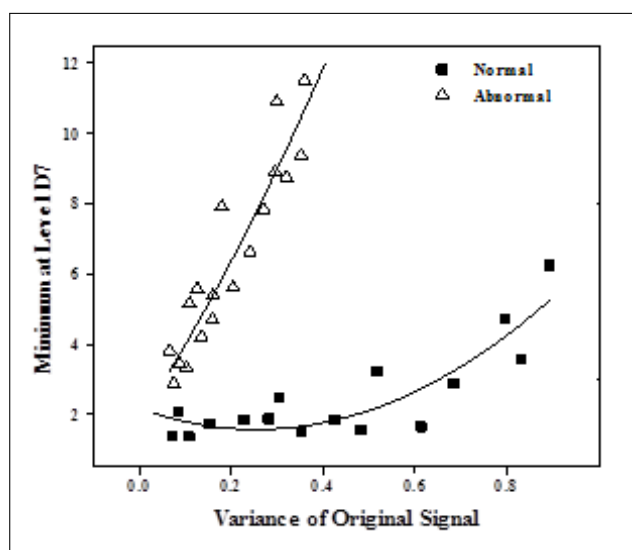


Figure 9: Variation in Minimum for both normal and abnormal EEG at D7.

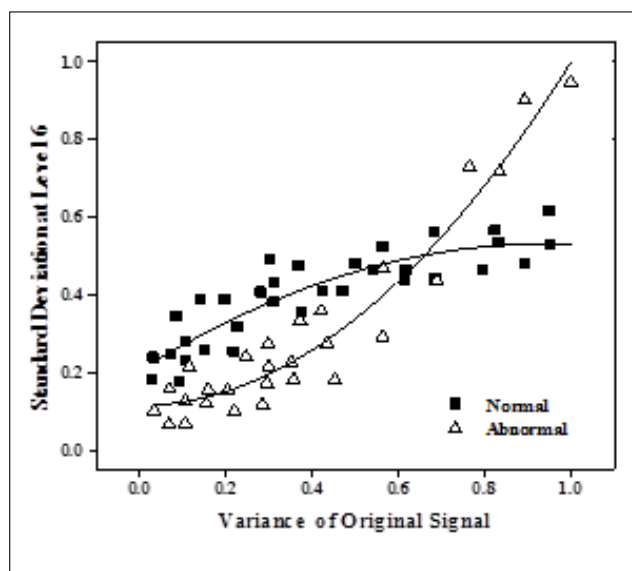


Figure 10: Variation in standard deviation at D6.

Figures 6 and 7 shows the variation in energy with the variance of the original signal for normal and abnormal subjects in levels D6 and D7 respectively. It was observed that the energy correlates well with the variance in level D6 and D7. A high degree of correlation ($R=0.95$)

is found for abnormal subjects in level D6. Figure 8 and 9 show the variation in minimum value with the variance of the original signal for normal and abnormal subjects respectively. A high degree of correlation ($R=0.95$) was found for abnormal subjects in level D6. It was found that correlation of minimum value with variance was more in abnormal than normals. The variation in measured Standard deviation values of decomposed wavelet coefficient with values of variance for normal and abnormal subjects is shown in Figures 10 and 11 respectively. A high degree of correlation ($R=0.97$) was found for abnormal subjects in level D7. It was found that correlation of standard deviation value with variance is more in abnormal subjects than normal subjects.

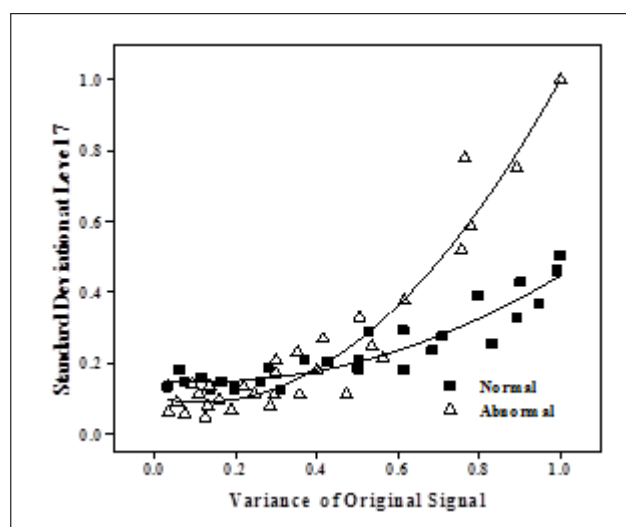


Figure 11: Variation in standard deviation at D7.

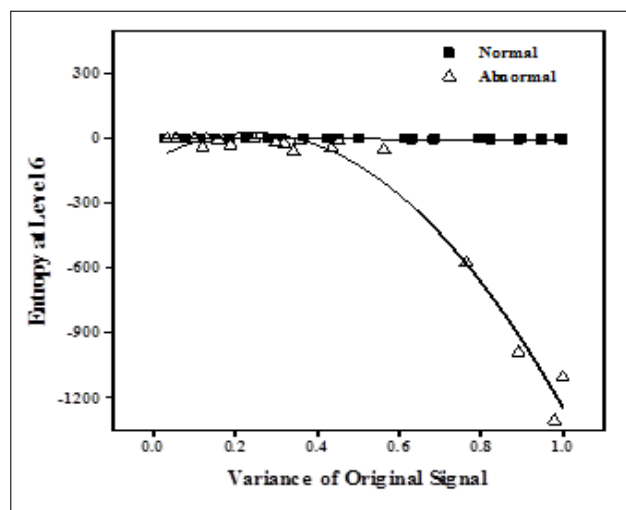


Figure 12: Variation in Entropy for both normal and abnormal EEG at D6.

The variation in Entropy values of wavelet coefficient with values of variance for normal and abnormal subjects is shown in Figures 12 and 13 respectively. Entropy is a measure of the disorder present in a system. The negative value of the entropy of the Abnormal EEG shows

that there is a move towards ordered state. From Figures 12 and 13, it is seen that the correlation between entropy and variance for normal subjects is lower ($R=0.88, 0.91$) stating that the signals are deterministic and for abnormal subjects the correlation values were found to be ($R=0.98, 0.96$) higher. Among the entire parameters mean, Hurst exponent, frequency at maximum power of the spectrum and largest Lyapunov exponent show poor degrees of correlation. Thus the parameters Energy, minimum, standard deviation and entropy derived from approximated coefficients seems to be useful parameters to differentiate normal and abnormal.

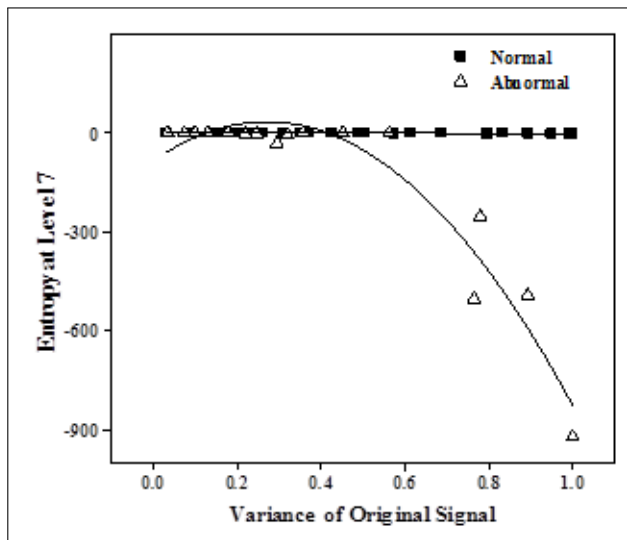


Figure 13: Variation in Entropy for both normal and abnormal EEG at D7.

The percentage variances between the various quadratic spline wavelet features were estimated for the normal and abnormal subjects. The Principal Components that explain the maximum percentage variance were chosen and the corresponding component magnitudes were analyzed. The parameters with highest magnitudes in the loadings of the Principal Components were chosen for further classification and are shown in Table 5.

Performance of the intelligent computing techniques Tables 6 and 7 show the performance comparison of all the methods without PCA and with PCA based features. It was found that RBFNN classifies EEG signals better than the other methods for all features and PCA based features. Positive predictive value was better in PSONN and ANFIS than BPN method. It is clearly seen that RBFNN has better accuracy when compared with the other classifiers. These results indicate that the proposed RBFNN model has a potential in clinical seizure detection. Table 8 shows the comparison of classification accuracy with PCA based features for normal EEG and different types of seizure EEG signals.

4 Conclusions

In this study, normal and seizure EEG features were extracted using quadratic spline wavelet. The appropriate feature components were delineated and the corresponding statistical parameters were computed. In this work, clinical EEG signals were classified into normal and abnormal, using intelligent computing techniques. The performance of the developed classifiers was assessed and compared using sensitivity, specificity, positive predictive and negative predictive values. The conclusions were drawn after meticulous experimentation on best architecture, number of hidden neurons required and performance goal. It was observed that the RBFNN has better classification accuracy when compared to BPN, ANFIS and PSONN. The value of specificity shows that RBFNN classifies abnormal data more accurately than ANFIS and back propagation network. The positive predictive value suggests that the classification of EEG signals into normal is higher in the RBFNN than that of the other classifiers used in this study. The negative predictive value indicates that the back propagation network diagnoses the abnormal data more correctly than the normal data. It was found that the RBFNN classifies Generalized Tonic Clonic seizure better than the complex partial seizure and normal EEG

Table 4: The correlation coefficient of variance and wavelet derived features for level D4 – D8.

Features	D4			D5			D6			D7			D8		
	N	A	p	N	A	p	N	A	p	N	A	p	N	A	p
Energy	0.84	0.85	0.0096	0.87	0.84	0.0101	0.89	0.95	0.0039	0.85	0.89	0.0027	0.75	0.88	0.2788
Maximum	0.89	0.84	0.0206	0.93	0.57	0.1777	0.83	0.93	0.6657	0.93	0.94	0.5877	0.83	0.92	0.8744
Minimum	0.96	0.84	0.0025	0.97	0.76	0.3654	0.84	0.95	0.0011	0.88	0.93	0.0001	0.39	0.76	0.0004
Mean	0.38	0.16	0.0091	0.21	0.38	0.4621	0.43	0.57	0.9849	0.93	0.93	0.7396	0.92	0.65	0.2231
Std	0.83	0.96	0.0002	0.87	0.86	0.0001	0.88	0.96	0.0021	0.93	0.97	0.0001	0.48	0.95	0.2992
Variance	0.93	0.97	0.0046	0.90	0.85	0.0001	0.81	0.93	0.0031	0.66	0.73	0.0008	0.61	0.65	0.0001
Hurst	0.39	0.19	0.5256	0.85	0.43	0.5646	0.46	0.74	0.0030	0.39	0.67	0.0001	0.93	0.86	0.3333
Entropy	0.85	0.96	0.6977	0.82	0.87	0.0001	0.88	0.98	0.0086	0.91	0.96	0.0167	0.87	0.73	0.0179
Pyy	0.64	0.42	0.5088	0.89	0.69	0.1416	0.89	0.99	0.1388	0.97	0.41	0.0046	0.91	0.28	0.0048
Freq at Pyy	0.30	0.04	0.0001	0.79	0.18	0.3092	0.88	0.77	0.0249	0.28	0.42	0.7906	0.99	0.11	0.3215
LLE	0.30	0.06	0.0239	0.64	0.19	0.9153	0.91	0.72	0.0870	0.76	0.85	0.0081	0.76	0.33	0.0897

N=Normal, A=Abnormal, p=pvalue D4 – D8 decomposed levels of wavelet transform

Table 5: Component Magnitudes in PC1 and the corresponding features for Normal and seizure EEG.

Component	Magnitude	Sub-band	Corresponding features in the dataset
PC(13)	0.199	D6,D7	Minimum of absolute value
PC(32)	0.196	D6,D7	Energy
PC(18)	0.195	D6,D7	Entropy
PC(35)	0.193	D6,D7	Standard deviation

Table 6: Comparison of Performance of the methods with all features.

Indices	BPN (%)	ANFIS (%)	PSOINN (%)	RBFNN (%)
Accuracy	73	79	81	85
Sensitivity (True positive rate)	66	74	80	76
Specificity	83	87	83	100
False positive rate (1-specificity)	17	13	17	0
Positive Predictive Value	90	90	89	100
Negative Predictive Value	60	67	71	71

Table 7: Comparison of classification performance with PCA based features.

Indices	BPN (%)	ANFIS (%)	PSOINN (%)	RBFNN (%)
Accuracy	89	93	94	99
Sensitivity (True positive rate)	96	90	92	98
Specificity	80	97	97	100
False positive rate (1-specificity)	20	3	3	0
Positive Predictive Value	86	98	98	100
Negative Predictive Value	93	85	88	97

signals. The proposed methodology makes it possible as a real-time detector, which will improve the clinical service of Electroencephalographic recording. Hence the combination of Wavelet transform method and PCA derived features pertaining to normal and seizure EEG along with RBFNN based classification appears to be efficient for automated EEG signal classification.

Table 8: Comparison of classification accuracy with PCA based features for normal EEG and different types of seizure EEG signals.

Algorithm	NORMAL	GTCS	CPS
BPN	93.3	86.7	85
RBFNN	100	96.7	100
ANFIS	96.7	90	90
PSOINN	96.7	93.3	90

Acknowledgements

We would like to thank the EEG experts and the team of technicians for their technical support especially for the data acquisition and handling, from the department of Neurology, Sri Ramachandra University, Chennai.

References

- [1] Sunil P, Ramakant Y, Seizures and epilepsy in central nervous system infections. *Neurology Asia*. 2004; 9 (1): 4 -9.
- [2] Singhi P, Infectious causes of seizures and epilepsy in the developing world. *Dev Med Child Neurol*. 2011; 53 (7) : 600-609
- [3] Rajendra Acharya U, Filippo M, Vinitha S, Sree, Subhagata Chattopadhyay, Kwan-Hoong Ng, Jasjit S Suri, Automated diagnosis of epileptic EEG using entropies, *Journal of Biomedical Signal Processing and Control*, 2012; 7(4):401-408.
- [4] Ling Guo , Daniel Rivero, Alejandro Pazos, Epileptic seizure detection using multiwavelet transform based approximate entropy and artificial neural networks, *Journal of Neuroscience Methods*, 2010;193:156-163.
- [5] Abdulhamit Subasi , EEG signal classification using wavelet feature extraction and a mixture of expert model *Expert Systems with Applications*, 2007; 32(4):1084-1093.
- [6] Abdulhamit Subasi , Application of adaptive neuro-fuzzy inference system for epileptic seizure detection using wavelet feature extraction, *Computers in Biology and Medicine*, 2007; 37(2): 227-244.
- [7] Abdulhamit Subasi , Automatic detection of epileptic seizure using dynamic fuzzy neural networks, *Expert Systems with Applications*, 2006; 31(2) : 320-328.
- [8] Hasan Ocak, Automatic detection of epileptic seizures in EEG using discrete wavelet transform and approximate entropy *Expert Systems with Applications* , 2009; 36:2027-2036.
- [9] Najumnisssa.D, Rangaswamy,TR., Detection and Classification of Epileptic Seizures using Wavelet feature extraction and Adaptive Neuro-Fuzzy Inference System, *International Journal of Computational Engineering Research*, 2012; 2(3): 755-761.
- [10] Kavitha A, Sujatha CM and Ramakrishnan S, Evaluation of Flow-Volume Spirometric test using Neural Network based prediction and Principal Component Analysis. *Journal of Medical Systems*, 2009; 35(1):127 -133

- [11] Guler, NF, Ubeyli, ED, Gulaer, I. Recurrent neural networks employing Lyapunov exponents for EEG signals classification. *J. Expert Systems with Applications*.2005; 29:506–514.
- [12] Sujatha CM, Mahesh V and Swaminathan Ramakrishnan, Comparison of Two ANN Methods for Classification of Spirometer Data. *Measurement Science Review*. 2008; 8(3): 53 – 57.
- [13] Yaunanghi, N, Najumnis, D and Shenbagadevi, S, Feature extraction and detection of epileptic seizure', *Proceedings of the National Conference on Signals, Systems and Communication*, 2006; 8–12.
- [14] Pena-Reyes CA, Siper M. A fuzzy-genetic approach to breast cancer diagnosis. *Artif. Intell. Med*.1999; 17: 131–155.
- [15] Nauck D, Kruse R, Obtaining interpretable fuzzy classification rules from medical data. *Artif. Intell. Med*.1999; 16: 149 –169.
- [16] Guler I, Ubeyli ED. Automatic detection of ophthalmic artery stenosis using the adaptive neuro-fuzzy inference system. *Eng. Appl. Artif. Intell*.2005; 18: 413–422.
- [17] Ubeyli ED, Guler I, Automatic detection of erythmato-squamous diseases using adaptive neuro-fuzzy inference systems, *Comput. Biol. Med*.2005; 35:421–433.
- [18] Guler I, Ubeyli ED , Application of adaptive neuro-fuzzy inference system for detection of electrocardiographic changes in patients with partial epilepsy using feature extraction. *Expert Syst. Appl*.2004; 27: 323–330.
- [19] Ubeyli ED, Guler I, Adaptive neuro-fuzzy inference systems for analysis of internal carotid arterial Doppler signals, *Comput. Biol. Med*. 2005; 35:687–702.
- [20] Jang JSR, ANFIS: adaptive network based fuzzy inference system, *IEEE Trans. Syst., Man Cybern*. 1993; 23 (3): 665–683.
- [21] Vieira J, Dias FM, Mota A, Artificial neural networks and neuro-fuzzy systems for modelling and controlling real systems: a comparative study, *Eng. Appl. Artif. Intell*.2004; 17:265–273.
- [22] Virant-Klun,I, Virant J, Fuzzy logic alternative for analysis in the biomedical sciences, *Comput. Biomed. Res*. 1999; 32 :305–321.
- [23] James Kennedy and Russell Eberhart , Particle Swarm Optimization, *Proc. IEEE International Conf. on Neural Networks*, 1995; 4: 1942-1948.
- [24] Enrico B. Theoretical interpretations and applications of Radial Basis Function Networks, *Elsevier Science*.2003: 3: 1-39.
- [25] Liu HX, Zhang RS, Yao XJ,Liu MC, Hu ZD, Fan BT, Prediction of electrophoretic mobility of substituted aromatic acids in different aqueous-alcoholic solvents by capillary zone electrophoresis based on support vector machine. *Analytica Chimica Acta*, 2004;525(1): 31-41.
- [26] Sujatha CM , Ramakrishnan S, Prediction of Forced Expiratory Volume in Pulmonary function test using Radial basis Neural Networks and k-means Clustering, *Journal of Medical Systems*, 2009; 33: 347-351.
- [27] Samanwoy GD, Hojjat A. Nahid D, Principal component analysis – enhanced cosine radial basis function neural network for robust epilepsy and seizure detection, *IEEE Transactions on Biomedical Engineering*.2008; 50: 512-518.
- [28] Korurek M, Dogan B. ECG beat classification using particle swarm optimization and radial basis function neural network, In: *Journal of Expert Systems with Applications* , 2010; 7563-7569 .
- [29] Zhang Y, Lu Z, Li J : Fabric defect classification using radial basis function network, In: *journal of Pattern Recognition Letters* ,2010; 2033-2042.
- [30] Maqsood I , Ajith Abraham, Weather analysis using ensemble of connectionist learning paradigms, *Applied soft computing*, 2007; 7: 995-1004.
- [31] Kandaswamy A., Kumar CS, Ramanathan RP, Jayaraman S, Malmurugan N, Neural classification of lung sounds using wavelet coefficients, *Comput. Biol. Med*.2006; 34 (6): 523–537.
- [32] Quian Quiroga R and Schürmann M, Functions and sources of event-related EEG alpha oscillations studied with the Wavelet Transform. *Clin. Neurophysiol.*,1999; 110: 643-655.
- [33] Akay M,Wavelet applications in medicine, *IEEE Spect*.1997; 34 (5) : 50–56.
- [34] Gotman J, Gloor P, Schaul, N. Comparison of traditional reading of the EEG and automatic recognition of interictal epileptic activity. *Electroencephography clinical. Neurophysiol*. 1978; 44: 48 – 60.
- [35] Joon L, Stefanie B, Mike JC, David JK, Glenn B, Tom C., A radial basis classifier for the automatic detection of aspiration in children. *J.NeuroEng. Rehabil*. 2006; 3:1-17.
- [36] Hall M A, and Smith L A, Practical feature subset selection for machine learning, In *Proceedings of the 21st Australian Computer Science Conference*, 1998; 181–191.

A Rapid and Reproducible Report on the Morphological and Functional Characteristics of Spermatozoa Using Digital Image Processing Technique

Joseph Pushpa Innocent D ¹, Suseela M.R ¹, Priya Lakshmi N ², Jesuchristopher J ²

¹ Department of Microbiology, Rajah Muthiah Medical College, Annamalai University, Chidambaram, India

² Department of Human Biology, Faculty of Health Sciences, University of Cape Town, South Africa

Abstract

Background and Objectives: Semen analysis plays a vital role in understanding the healthy state of the sperm in men. The computer aided semen quantification technique quantifies the quality of the sperm from the semen sample which is digitally sampled and processed using digital image processing technique.

Methods: The semen samples were collected from 402 infertile men aged between 25-50 years. Similarly 25 samples were collected from the age matched healthy fertile men (control group) as per the diagnostic report from the physician. A total of 427 samples used in this study were analyzed using traditional manual method (ground truth) and the proposed automated method based on the image processing algorithm.

Results: Conventional semen analysis procedure was performed manually after liquefaction of the samples.

The parameters such as morphology, sperm count and motility types were determined and compared between manual and automated methods. We have achieved a significant repeatability and reproducibility of the results using the automated method. Automated method has demonstrated to be computationally efficient and it required less amount of time to process any given field of view. It is also less susceptible to any rater bias for the analyzed field of view and the results were comparable with the manual method.

Conclusions: In this article we describe the developmental stages involved in the semen analysis, custom built automated image analysis protocol and the report generation based on the parameters involving sperm count and motility types.

Keywords

Semen analysis, sperm count, sperm motility, image processing

Correspondence to:

Joseph Pushpa Innocent Danislas

Department of Microbiology, Rajah Muthiah Medical College, Annamalai University, Chidambaram, India

Address:

E-mail: josephmary2k9@gmail.com

EJBI 2013; 9(2):52-57

received: January 16, 2013

accepted: March 27, 2013

published: August 30, 2013

1 Introduction

The responsibility of infertility falls on both male and female factors, a single and major male factor involved in infertility associated with spermatozoa [1]. Evaluation of sperm count, morphology and its motility are very useful factors in the diagnosis of male infertility. Manual method of semen analysis is rather subjective technique, time consuming and often show large inter-laboratory variations [2]. Computer based sperm analysis methods are classical ways to determine the potential fertility of boars [3]. The four major factors which have to be considered during the evaluation of boar are sperm quality, concentration, moti-

lity and acrosome integrity [4]. Image processing techniques were used for a rapid and reproducible report on the structural and functional evaluation of spermatozoa by fully automated methods. Computer-Assisted sperm analysis systems provide a rapid and automated assessment of the sperm characteristics, together with improved standardization and quality control [5].

In this work, the spermatozoa and its motility were captured using high resolution digital video camera. The captured video was converted in to image frames and was subjected to object tracking image processing algorithms to study the sperm structural and functional characteristics [1]. Sperm motility was studied according to

the guidelines from World Health Organization (WHO) [6]. The specific morphological characteristics such as, the count and the percentage of motility of the individual spermatozoa were assessed. The procedure was repeated with different samples and the results were recorded. Aliquots of the same semen samples were analyzed simultaneously by manual method. The results were recorded for both manual and the computer assisted method for further validation.

2 Materials and Methods

The samples were collected freshly after 3 days of abstinence period by strictly following standards of the World Health Organization. These samples were collected from infertility clinic (Rajah Muthiah Medical College Hospital) between the periods from February 2008 till March 2010. A total 427 samples were collected, among them 402 were infertile and 25 are healthy controls with the mean age of 37.5 ± 12.5 .

2.1 Conventional Semen Analysis

It was clearly explained to the individuals concern, about cleaning the hands, external genitalia and the collection procedure of semen. The samples were collected by masturbation after passing the urine. The ejaculated semen was collected in a sterile wide mouth container and the time of collection was recorded. Manual semen analysis was carried out with diluted semen in saline in the proportion of 1:20 (0.02 mL specimen mixed with 0.38 mL of saline), after liquefaction at a temperature of 37°C for 30 minutes. The morphology, motility, and parameters such as the percentage of actively motile, sluggishly motile and non-motile were observed using a wet mount preparation using high power objective. The total sperm count was recorded using Neu baur Chamber after appropriate dilution with semen diluting fluid.

2.2 Computerised Semen Analysis

The same samples were analyzed using computer based semen analysis tool developed in-house for this project. A wet mount was made using a drop of semen and focused with high power objective of a trinocular microscope. The video image of the sperms was captured using high resolution (8MP) digital camera with a frame rate of 25fps PAL format fitted on the trinocular head of the microscope. Using the video mode, the motility of the spermatozoa was recorded. The illumination and brightness of the field of view were kept uniform, to minimize the segmentation error. The recorded video was processed sequentially and each frame is considered as a single digital image. The digital images were fed to the object tracking algorithm (based on image indexing method) developed in MATLAB environment. For each frame the segmentation of the sperms were done as the initial step. Debris in the frame

was removed easily since the signal intensity of the debris was not in the range of sperm. The Matlab based image indexing method was used to separate different objects (sperm, debris and background) in the image according to their intensity distribution. The indexing method clusters the image intensities according to the number of input clusters given to the algorithm. These indexed sperms were segmented and tracked on the neighboring frames around a particular block of neighborhood. The distance travelled by a particular sperm over the number of frames enable to determine their types of motility. The Euclidean distance was used to measure the distance travelled by the sperm between the first and the last frame and their velocity (distance*time (number of frames in this case)) had been estimated to classify the sperm types. The parameters such as number of sperms in a frame, motility (active motile, sluggish, non-motile), total count and their percentage were calculated for each field of view. The ratio of number of sperms to the distance travelled aided to classify the indexed sperm into actively motile, sluggishly motile and non-motile sperm. The intermediate group between the motile and non-motile is referred as sluggishly motile.

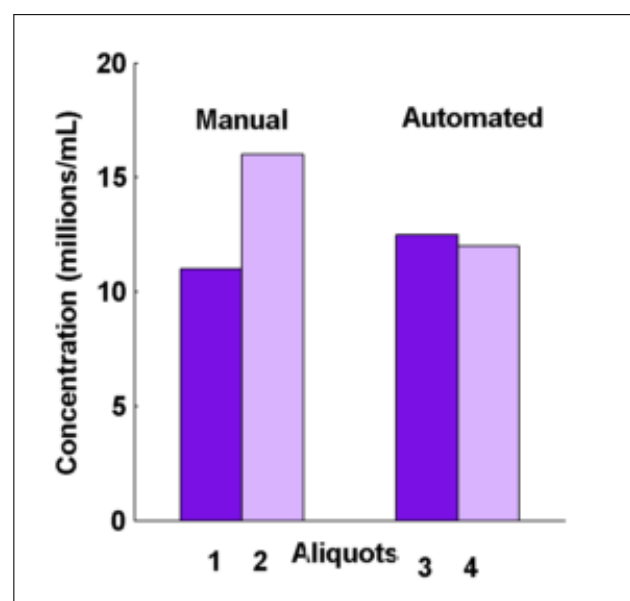


Figure 1: Comparison of total sperm count in Oligospermic semen between manual and automated methods.

3 Results

High resolution image of the spermatozoa in the selected field of view helps to reduce the background and to extract the clear boundary of the sperm. The sperms present on each frame were segmented from the given field of view initially and each of the frames was processed sequentially, which enabled to track the motion of individual sperms from frame to frame. By calculating the distance travelled by each sperm over a large dataset of frames for a definite period of time we were able to determine the

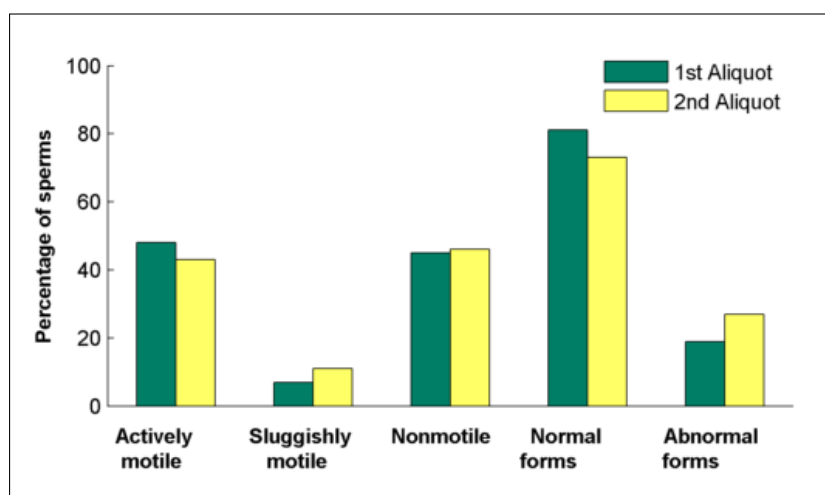


Figure 2: Percentage of sperms classified with respect to their type of motility using manual method for Oligospermic semen analysis.

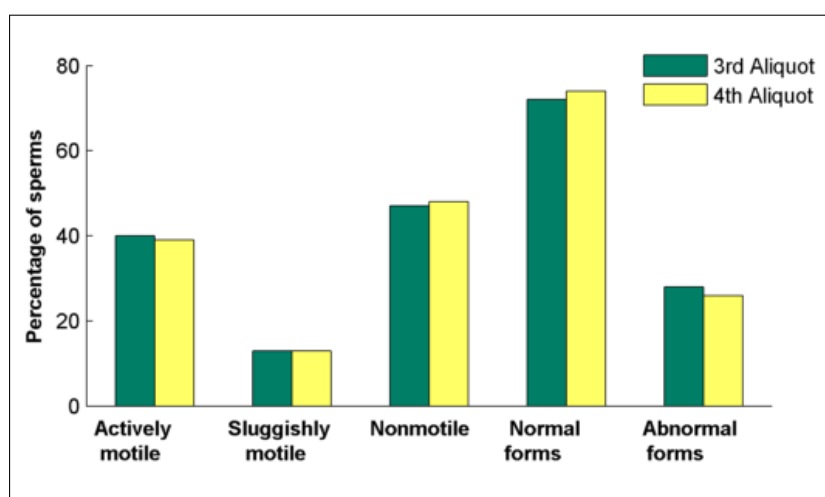


Figure 3: Percentage of sperms classified with respect to their type of motility using proposed automated method for Oligospermic semen analysis.

motility associated with each sperm. Based on the derived parameters an exact quantification of sperm count, and their motility characteristics were determined. The ratio of motile sperms to the total number of sperms in the given field of view for the dataset enables to classify the dataset into Azospermic, Oligospermic and Normospermic and compared with the manual methods.

The results of Oligospermic semen analysis using the automated method is comparable to the results obtained by manual method. We have observed larger difference in the total sperm count in 1st and 2nd aliquot using the manual method. In automated method we observe that the results were reproducible, the difference in the 3rd and the 4th aliquot is significantly lesser than the difference obtained in manual method. The difference observed in the automated method might be contributed by artifacts occurred during the video acquisition. However with second aliquot the values of various parameters observed in the manual method were not consistent with the 1st aliquot

(Figure 2), whereas the automated analysis yielded almost a similar result both in the 3rd and 4th aliquot (Figure 3). The variations in the total sperm count in Oligospermic semen analysis are illustrated in Figure 1 for manual and automated methods. Similarly Figure 2 and 3 explain the intra assay differences of additional parameters such as motility and abnormal forms in the manual and automated methods respectively.

The difference exhibited with respect to the number of sperms is clearly illustrated in Figure 4 for both manual and automated methods. The results of Normospermic semen analysis proved that the automated method of sperm count is comparable with the manual method (Table: 1, aliquots 1 and 3). While comparing the 2 aliquots of manual method we could observe the variability of the parameter between the aliquots. This variation between the aliquots (Table: 1 3rd and 4th aliquot) is not highly pronounced in the automated method.

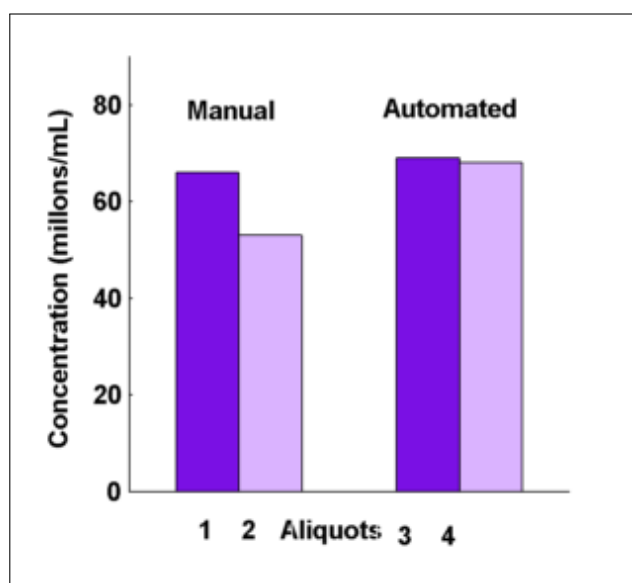


Figure 4: Comparison of total sperm count in Normospermic semen between manual and automated methods.

Similarly Figure 5 and 6 explain the intra assay differences of additional parameters such as motility and abnormal forms in the manual and computerized methods respectively. It was observed both in primary and in repeated analysis of the same Normospermic semen by computerized method showed almost consistent results, whereas in the manual method have large variations and are highly subjective.

In-house custom build software along with graphical user interface (GUI) was designed specifically for this application in Matlab shown in Figure 7. The GUI interface contains the provision for loading the Image and running the object tracking algorithm to calculate the motility of the sperm and displaying the end results which can be useful in day today routine clinical practice.

4 Discussion

The 427 study sample was divided into four equal aliquots. After incubation for liquefaction, aliquots of the same sample were simultaneously subjected to both conventional and automated semen analysis procedure.

Aliquots one and three were analyzed by conventional and automated method respectively. The same procedure was repeated again for second and fourth aliquots to test for reproducibility.

It was reported by Fereidoon et al., that the results by human are prone to minimal errors and proved to be a time consuming in a conventional sperm analysis performed by a specialist under light microscope [1]. Slow moving cells other than the motile sperms, image of certain debris and immotile sperms from which the sperms must be differentiated which is not possible in manual method causing these errors [7]. It is also difficult for the specialist to keep track of all the moving objects and the stationary debris at the same instant and it leads to significant stress in the eyes of an observer. Therefore manual method is rather subjective technique, time consuming and often contributes to large inter- laboratory variations [6] leading to difficulties in achieving the desired reliability.

High quality input images are vital for the image processing algorithm developed in MATLAB 6.5.1 software in windows XP operating system on a Pentium IV personal computer. With the above conditions being ideal, one could estimate and quantify the sperm count, the structural variations, and type of motility using automated methods. In this work the image of spermatozoa and its movement along with other parameters were analyzed using high resolution video camera fitted with microscope. Parameters such as sperm motility, type of motility, normal and abnormal forms of the above two methods were compared. Results of semen analysis by manual method were consistently difficult to maintain the reproducibility.

Normal and abnormal classifications were made based on the results of the semen samples and the samples were classified as Azospermia, Oligospermia and Normospermia. On analysis of the repeated results on the parameters of above three classes, we could able to observe a consistent results both in Oligospermic and in Normospermic semen using automated method. The values of the parameters estimated by manual method were inconsistent. Preliminary study results illustrates that the use of automated semen analysis is more objective and reproducible than technician based motility assessment. In future we are aiming to capture the structural pattern and morpho-

Table 1: Normospermic semen analysis between manual and automated method.

Parameters analyzed	Manual method		Computerized method	
	1st aliquot	2nd aliquot	3rd aliquot	4th aliquot
Total sperm count	66 millions/ml	53 millions/ml	69 millions/ml	68 millions/ml
Actively motile (%)	70	61	78	77
Sluggishly motile (%)	12	19	10	12
Non motile (%)	18	20	12	14
Normal forms (%)	83	81	78	80
Abnormal forms (%)	17	19	22	20

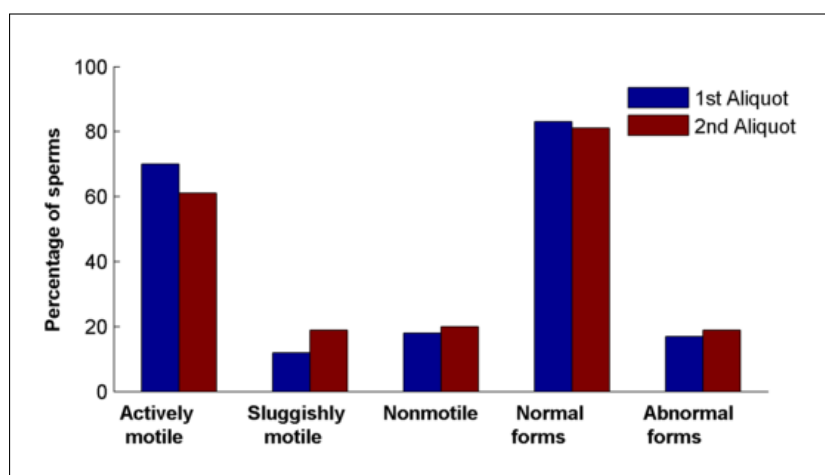


Figure 5: Percentage of sperm classified with respect to their motility using manual method for Normospermic semen analysis.

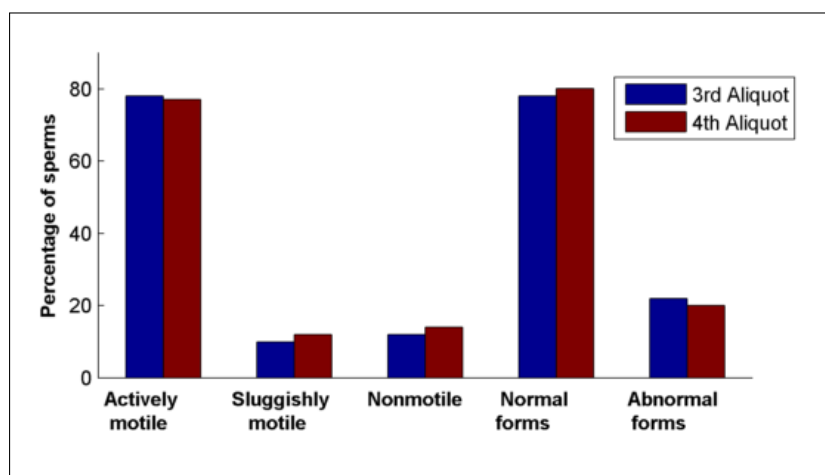


Figure 6: Percentage of sperm classified with respect to their motility using automated method for Normospermic semen analysis.

logy of the sperm and estimate a feature space to segment all types of sperm which can provides a better insight of the structural and functional characteristics of the sperm.

5 Conclusion

In conclusion automated semen analysis provides objective results in minutes along with the report and its user interface allow performing a complex operation in a simpler way.

The physicians reviewed about its convenience to handle multiple datasets in a given instant and its easier way of generating the reports. On repetition of the experiment on different samples the results were obtained with acceptable variations.

Results were encouraging in Oligospermic and Normospermic samples. When the count was more than 80 million/ml (study under process results not given) a dilution technique was needed to reduce the overcrowding of spermatozoa to get reproducible results. We propose to further develop and enhance the features of this user-

friendly sperm analysis method with increasing the number of parameters like morphology, velocity of the sperm in different concentrations, which will give a better understanding of the underlying principles of motility.

References

- [1] Fereidoon N.R., Mohammed H.M and Vahid R.N. A Multi Steps Algorithm For Sperm Segmentation In Microscopic Image. Proceedings of the World Academy of Science, Engineering and Technology. 2005; 12: 43-45.
- [2] Jorgensen N., Auger J., Giwercman A., Irvine D.S., Jensen T.K., Jouannet P., Keiding N., Le Bon C., MacDonald E., Pekuri A.M., Scheike T., Simonsen M., Suominen J., and Skakkeboek N.E. Semen Analysis Performed By Different Laboratory Teams: An Intervariation Study. Int.J.Anrol. 1997; 20(4): 201-208.
- [3] Sanchez L., Petkov N., and Alegre E. Statistical Approach To Boar Semen Evaluation Using Intracellular Intensity Distribution Of Head Images. Cellular and Molecular biology. 2007; 52(6): 38-43.

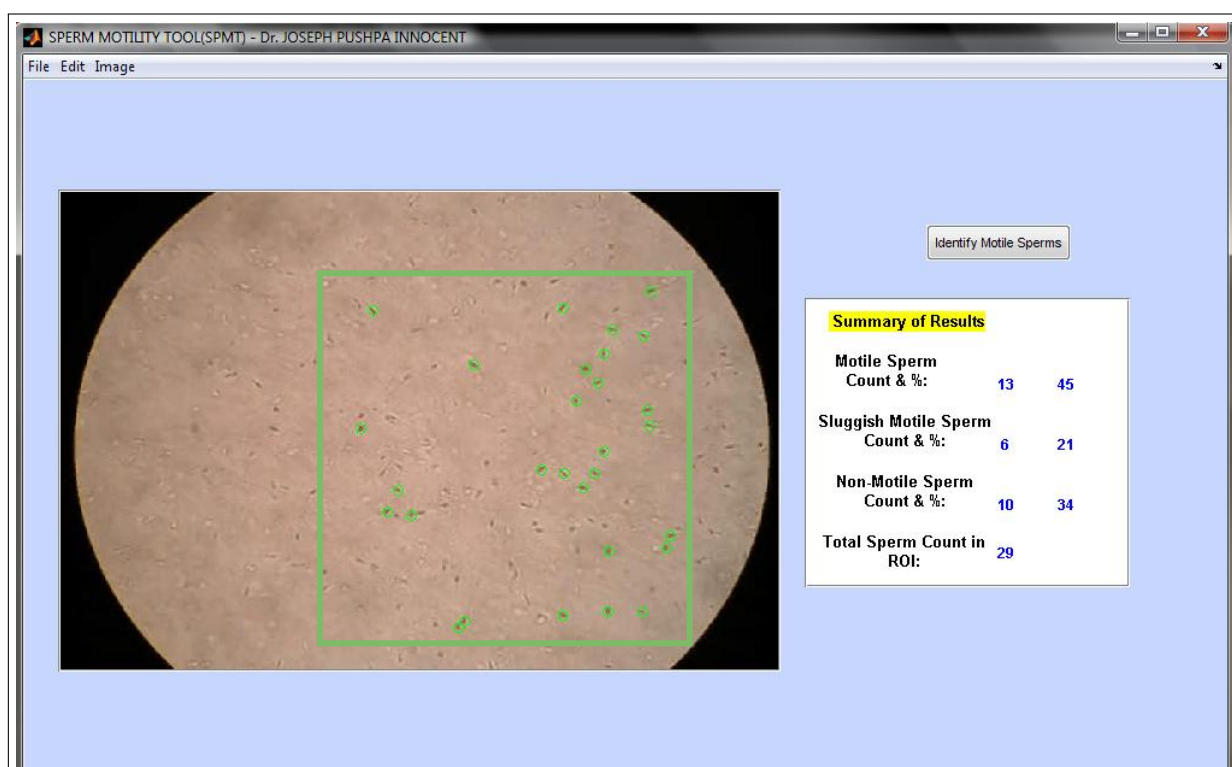


Figure 7: Graphical user interface for Sperm motility analysis. (Region of Interest to be analysed is manually marked by rectangle box in light green by the user on one frame to perform the automated segmentation in all the remaining frames; the identified sperms are marked in dark green).

- [4] Thurston L.M., Holt W.V., and Watson P.F. POST-Thaw Function Status Of Boar Spermatozoa Cryopreserved Using Three Controlled Rate Freezers: A Comparison. *Theriogenology*. 2003; 60(1): 101-113.
- [5] Vahid R.N., Mohammad H.M., and Mohammad H.N. Sperm Identification Using Elliptic Model and Tail Detection. *Proceedings of the World Academy of Science, Engineering and Technology*. 2005; 6:205-208.
- [6] Lene L., Thomas S., Tina K.J., Jens P.B., Erik E., Niels H.H., Yue Z., and Niels E.S. Computer-Assisted Semen Analysis Parameters As Predictors For Fertility Of Men From The General Population. *Human Reproduction*. 2000; 15(7): 1562- 1567.
- [7] Jens P.B., Erik E., Tina K.J., Niels H.H., Henrik K., Thomas S., Aleksander G. and Niels E.S. Relation Between Semen Quality And Fertility: A Population Based Follow-Up Study Of 430 First Pregnancy Planners. *The Lancet*. 1998; 352: 1172-1177.

An Image Based Microtiter Plate Reader System for 96-well Format Fluorescence Assays

Durai Arun P¹, Sankaran K², Muttan S¹

¹ Dept. Of Electronics and Communication Engineering, College of Engineering, Anna University, Chennai

² Centre for Biotechnology, Alagappa College of Technology, Anna University, Chennai

Abstract

Background: 96-well microtiter plate assay are becoming popular analytical procedures in laboratory and clinical practices generating a demand for microtiter plate readers. The present colorimetric and fluorimetric based microtiter plate reader are efficient in general applications such as measuring reflectance, absorbance, and optical density of reaction mixtures. However, a dedicated system incorporating automation and computational techniques in specific microtiter plate readers for Drug discovery and Microbial viability, provides portability and compatibility with high-throughput analysis at affordable cost.

Objective: To develop image-based reader system for semi-quantitative measurements of transport assay performed in microtiter plate. In this work, we focus on deduction of illumination source and classification of fluorescence emitted by transport assay using this microtiter plate reader.

Method: We have taken the images of 96-well fluorescence efflux assay and developed an appropriate image analysis system to read the individual well images and categorize the results as fast efflux and slow efflux by the classifier. The images exhibited non-uniform illumination due to UV transilluminator, which then replaced by the circuit of blue LED after performing a study on its classification performance.

Statistical descriptive features extracted from the image are classified using k-means clustering technique. The proposed system can be adapted to read any kind of microtiter plate assay.

Results: For uniform illumination of the source, of both UV transilluminator and blue LED, the color profile varied in accord to reaction mixture concentration. For classification performance of the source, out of four different images at various intensities of illumination from blue LED circuit controlled by potentiometer, the classification of efflux assay for image with maximum intensity gave high accuracy than the rest. For classification performance of the classifier, out of 1920-sub-images, the classifier misclassifies none.

Conclusion: For the microtiter plate reader, which classifies the liquid transport assay as fast efflux or slow efflux, the usage of UV transilluminator as illumination source is limited due to its non-uniform illumination and blue LED is apt for this application due its uniformity. The k-means clustering technique had been effective for this application when fed with statistical features describing the clusters.

Keywords

Microtiter plate reader, microtiter plate, fluorescence assay

Correspondence to:

S. Muttan

Department of Electronics and Communication Engineering

Address: College of Engineering, Guindy, Chennai – 600 025

E-mail: muthan_s@annauniv.edu

EJBI 2013; 9(2):58–68

received: January 31, 2013

accepted: April 17, 2013

published: August 30, 2013

1 Introduction

Fluorescence is becoming a popular optical method of chemical and biochemical analyses. Research laboratory and Clinical laboratory procedures increasingly make use of such methods. In this scenario, 96-well and 384-well based high-throughput assays are useful in drug discovery, microbial viability etc. The commercially popular readers that depends on the individual well reading during X-Y scanning is expensive and seriously limits the use of

this method for peripheral clinical facilities. Hence, there is a need to develop instrumentation for microtiter plate reader.

In a typical microtiter plate based fluorescence assays in use, the reaction mixture is excited with a wavelength which is in the far UV or Visible region and the emission is measured in the visible range. In recent times, both excitation and emission are preferred in the visible range to reduce cost drastically, as LED sources have become very cheap. Scanning mode in commercial machines is the

one where the machine performs X-Y scan on each well of the microtiter plate and profile the fluorescence, absorbance, optical density, and other methods of the assay either by the pre-defined protocols or user-defined protocols. Hence, imaging mode would provide further advantage of cost and high throughput, than scanning mode of reading. There are several image analysis techniques used as in microscopy and gel documentation, but using that along with specific image acquisition for fluorescence or colorimetric assays in 96-well microtiter plate is the new venture. The available image acquisition system can be readily adapted for the microtiter plate imaging, but one has to develop appropriate statistical and computational methodologies for analyzing the data and convert the signal into useful outcome like concentration of an analyte or rate of reactions or positive or negative. The requirements for image acquisition hardware and image analysis systems could differ according to the need of application [1].

The goal of the proposed reader system is to group the samples in the image of 96-well microtiter plate assay in any one of the two categories, based on the assay performed. Gonzalez [2] and Shalkoff [3] have described in detail identifying a pattern recognition problem and providing the solution to it, which in this case, is a two-class pattern recognition problem. Statistical classification [4] can classify a two-class pattern recognition problem efficiently when apt features form the feature space. The challenge lies in finding the features, which shows the discrimination of classes. The computational technique [5] of extracting the useful features of the image helps in the process of feature selection.

The proposed system has a wide area of application for the assays performed in the 96-well microtiter plate when the developed algorithm is adapted for requirements of various assays. This enables the feasibility of a reader system being fast, accurate, and adaptive to various environments.

2 System Architecture

The Image analysis system developed to read the 96-well microtiter plate has sub-systems as any computer vision system [6] such as image acquisition, image pre-processing, image segmentation, feature extraction, and classifier. Here, the assay will provide the fluorescence difference when illuminated by UV-light or by any blue source in accord to the transport efflux. Wells' fluorescence is classified either fast or slow efflux individually by the classifier. As in [7], the architecture of the proposed reader has image acquisition hardware and image analysis software. The system architecture had underwent changes with respect to the changes evolved in the requirements of both in hardware and software. The system as in [7] had the hardware wherein there was no optic system for the magnification whereas an optic system is included for this proposed imaging hardware. Moreover, usage of UV trans-

illuminator contributed non-uniform illumination over a single microtiter plate, which led to the idea of altering the source. In addition, we changed the number of classes from four to two for the classification, due to the incorporated changes in assay. The assay now focuses only to find, whether the sample shows a fast or slow efflux. The image acquisition hardware [8] consists of the source and the lens system to bring actual size of plate to the corresponding image size in the acquired image. The image of the microtiter plate acquired by the digital camera, led to limited usage of the image pre-processing, for now. The image segmentation sub-system's goal is to segment the single microtiter plate image into 96 sub-images. The feature extraction sub-system extracts the radiometric and densitometric features [9] of the fluorescence sub-images. The classification and the decision-making subsystem used is k-means clustering technique.

3 Methodology

3.1 Image Acquisition and Segmentation

The image acquisition hardware used here is to acquire the image of 96-well microtiter plate consists of a source and three-lens system [8]. The source excites the samples in the well when incident from below. The excitation wavelength to read the fluorescence of the samples in assay used by fluorometer is 485 nm. The source wavelength needed to excite the fluorescence assay lies in the blue region of visible spectrum. Hence, the image acquisition hardware of this system needs a UV transilluminator or Dark reader transilluminator or blue light emitting diode (LED) [10] as a source. The three-lens system used here is to bring the actual size of the object, here the microtiter plate, to the image size of the object in the image. The three-lens arrangement is plano-convex lens, plano-convex lens, and plano-concave lens. From the plano-concave lens, a digital camera acquires the input image. An offline transfer of image was done from camera to computer for further processing.

The image segmentation in this application needs to be highly accurate since the region of interest is all over the spatial area of the image. For feature extraction and classification, the system has to segment 96 individual wells from the single microtiter plate image. The image of 96 well plate assay acquired by any source shows the order of arrangement of wells having 8 rows and each row having 12 wells in it. The wells are cropped by finding the center pixel of the respective wells and index of each wells are assigned to the subscripts of 8 rows - 12 columns matrix dimension. Figure 1 shows the UV excited plate and blue light emitting diode excited plate along with its segmented images respectively.

The UV transilluminator provides UV light as excitation source and for blue light, a circuit was built with commercially available blue light emitting diode (LED) such as SMD 3528, which emits a narrow band of blue light

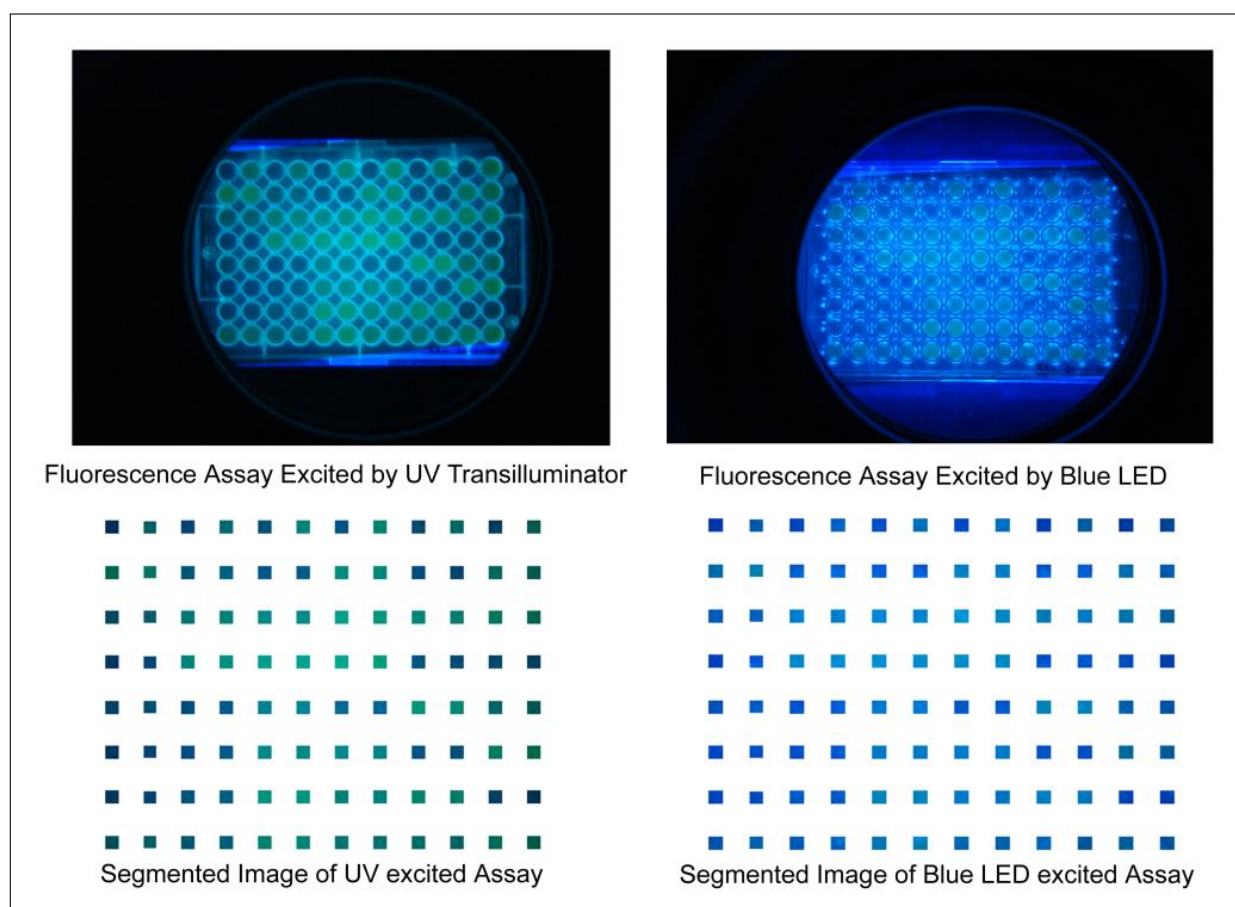


Figure 1: Original and Segmented Images of Fluorescence Assay excited by UV Transilluminator and Blue LED.

from 445 nm to 495 nm with center wavelength 470 nm. With the viewing angle of 120 degrees, the maximum luminous intensity range of 3528 blue LED is 600mcd and the maximum forward voltage range is 3.6V. The designed circuit delivers the maximum luminosity emitted per LED. Six LEDs per length and three LEDs per breadth are connected, making the arrangement that two lengthier sides have six LEDs each and two shorter sides have three LEDs each. Hence, the total luminance provided by this source is 100cd/m². Figure 2 shows the 3528 SMD blue light emitting diode source circuit designed for the 96-well microtiter plate to read the fluorescence assay.

Analysis of the illumination uniformity provided by the source over all wells of a plate shows its suitability for this application. An assay of fluorescein samples of concentration ranging from 100nM to 5000nM is prepared. The variation in the concentration of the fluorescein dye simulates the fluorescence emitted by the living microorganism samples. The lower the concentration the more blue the image will be and the higher the concentration the more green the image will be. The fluorescence assay is prepared in an arrangement such that every row and column has samples of different fluorescein concentration. This arrangement paved the way for the analysis of color definition of different concentration to different position of wells. Figure 3 shows the green component profile of plate

bearing different concentration irrespective of the position of wells excited by UV and blue LED.

The characterization of the fluorescein sample is to show higher green component for higher concentration and should decrease as the fluorescein concentration lowers. On comparing the profiles of UV excitation and blue LED excitation as shown in Figure 3, only the blue LED excitation depicts the needed characterization. The variation in the green component profile of UV excited plate is due to the arrangement of the quartz tubes present in the UV transilluminator [11]. The blue LED source unlike the transilluminator provided a uniform illumination across the area beneath the plate and excites all wells with it; hence, the color definition did vary in accord to the fluorescein concentration of the samples, irrespective to the position of the wells. Therefore, the 3528 blue LED is the suitable source than UV transilluminator for this fluorescence reading application.

3.2 Feature Extraction

Feature extraction is the process of extracting the information, which forms the input vector for the classification engine. Nevertheless, this process is pre-poned by Feature selection, an analytic process that provides the suitability of a data as an element of the input vector.

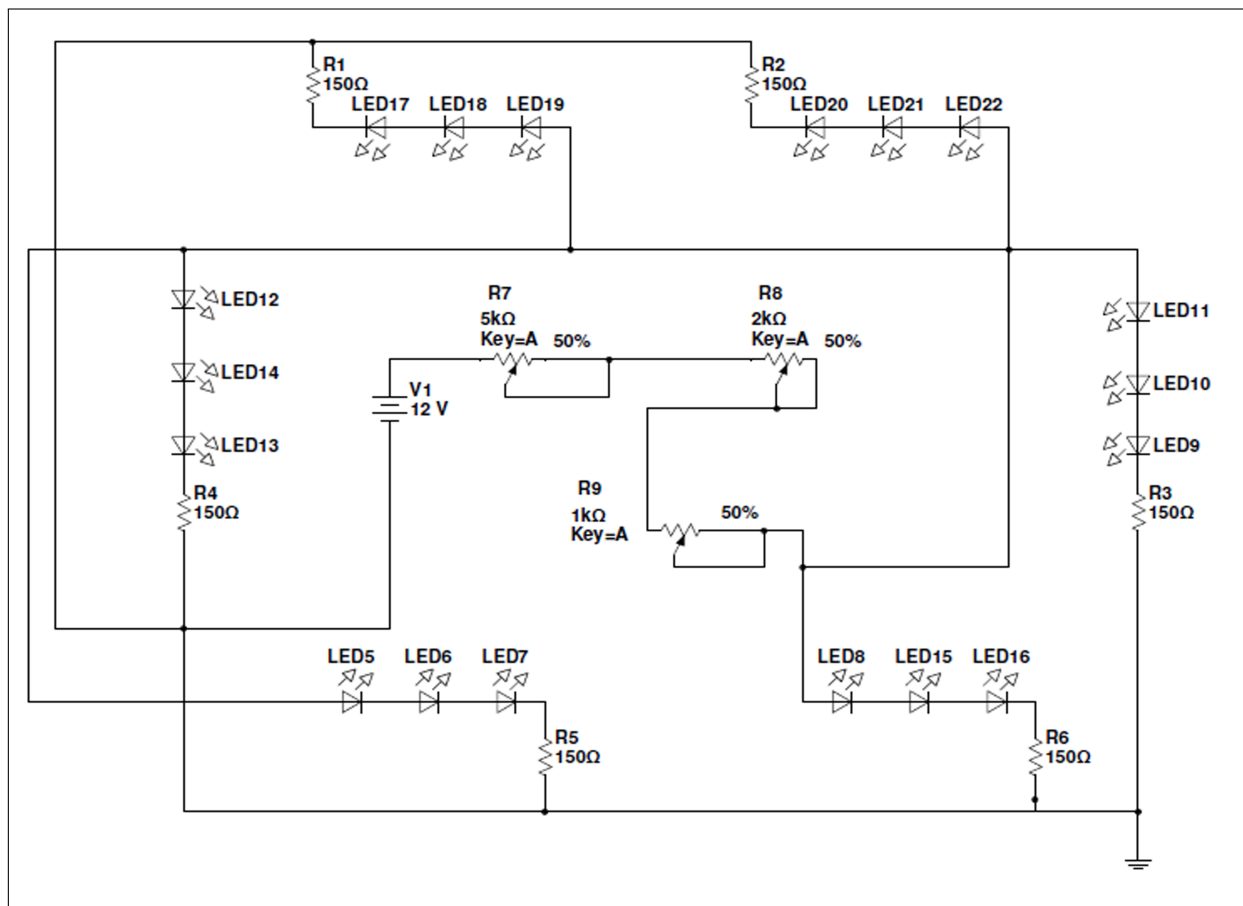


Figure 2: Schematic of Circuit designed with SMD3528 LED as Source for the Reader System.

Metin et al [9] have discussed the possible features which could be extracted from a fluorescence emitting images. The Chromatin specific features are the area of objects, integrated optical density, mean optical density, number of regions, compactness, distance, and center of mass. The radiometric and densitometric features are image bands, intensity, optical density, and mean optical hue. Statistical descriptive features, such as mean, median, mode, maximum, and minimum from the optical intensity of the pixels within the boundary pixels of the sub-images representing wells are extracted. Before performing the feature extraction and classification, in accord to the assay, segmented sub-images are re-assigned. The assay performed in the 96-well plate, from Test 1 to Test 6 forms six groups of samples, grouped as six different datasets for classification. The numbering inside the fields is the indexing of the wells of a 96-well plate in accord to the test performed. Table 1 shows the indices of segmented sub-images re-assigned as in the assay template for feature extraction and classification. After finding the suitable features for this application, the classifier classifies the generated feature vector.

The color variation is the most important event in this application and any variability in intensity will affect the system's performance. The acquired image and segmented sub-images are RGB color space based image.

The RGB color space is a three dimensional space, which has highly correlated Red (R), Green (G) and Blue (B) color vectors. The high correlation here means that if the intensity changes, all three-color vector components will change accordingly, known as 'Brightness Effect' [12]. For feature vectors, the red, green, blue components are less suitable, since visual enhancement is the focus of RGB color space than image analysis. The measurement of a color in RGB space does not represent color differences in a uniform scale, which reduces the possibility of evaluating the similarity of two colors from their distance in RGB space. The transformation of sub-images from RGB color space to HSV color space [12], converts the high correlative data to less correlative data. The HSV color space is also a variant of HSI (Hue-Saturation-Intensity) color space system.

The HSV color space system separates the color information and the intensity information from the image where, Hue and Saturation describes the Color Information and Value describes the Brightness Information. Hue represents the basic colors and Saturation is the measure of purity of color, which signifies the amount of white light mixed with the Hue. The Hue in HSV modeled from the Hue Color Wheel, defines any color in accord to its angle in the wheel. The angle range for Green and Blue in the Hue Color Wheel is 70 to 160 degrees and 165 to 240 de-

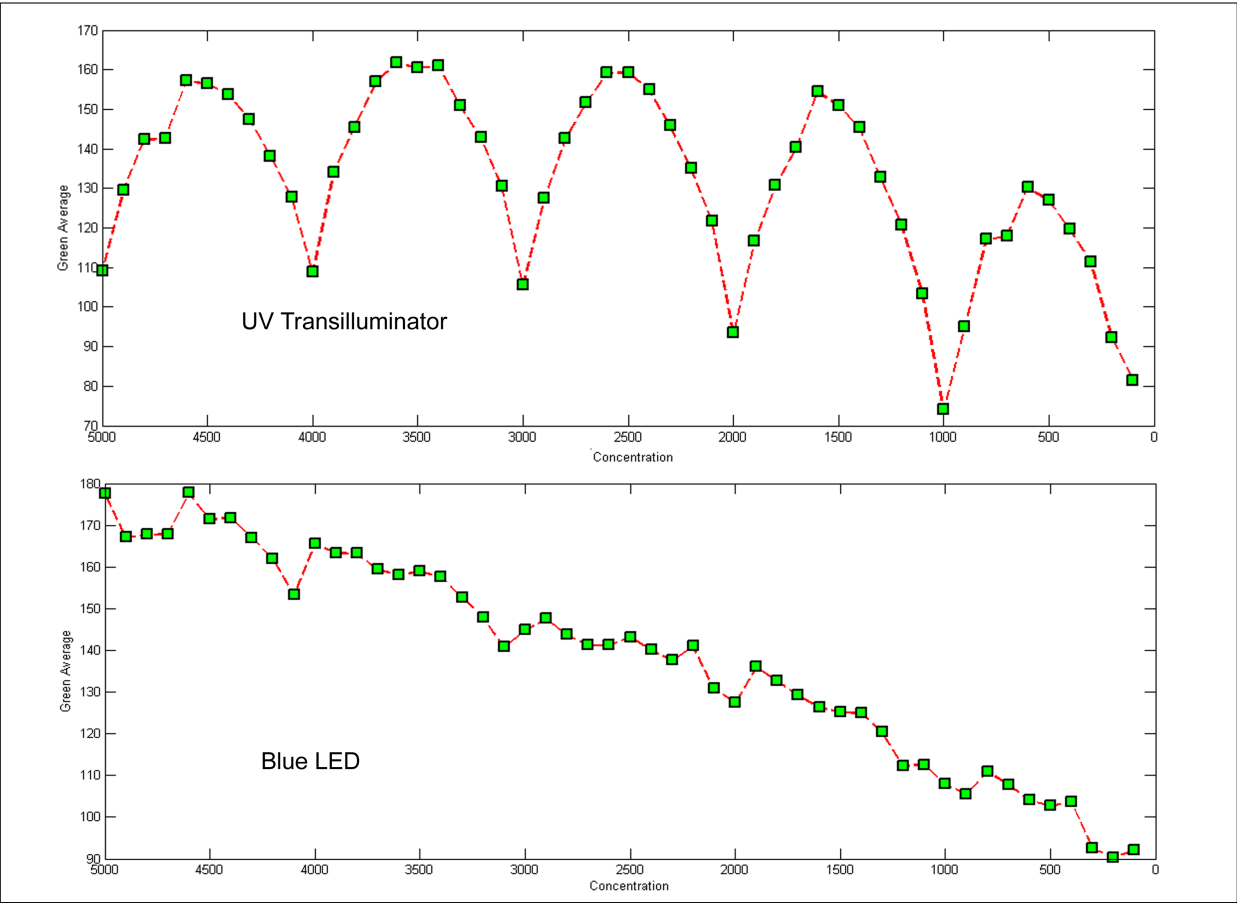


Figure 3: Green Component Profile for different concentration and positions excited by UV Transilluminator and Blue LED.

greens respectively. In HSV color space, the Hue range of Green and Blue is 0.2 to 0.4 and 0.45 to 0.7 respectively.

A fluorescein dye concentration simulates the color variation depicted by the fluorescent transport liquid assay. Assays of fluorescein concentrations 100 nM, 500 nM, 1000 nM, 2500 nM, and 5000 nM are prepared in five different plates, filled in all wells, and excited by blue LED. The color definition depicted due to fluorescence emitted by 1000 nM fluorescein concentration is the minimum for a fast transport efflux and fluorescence emitted by other

lower concentration than 1000 nM depicts the color definition of slow transport efflux. Figure 4 shows the Hue average profile for different concentration, describing the curves descending from blue region to green region of the Hue in HSV in accord to its corresponding concentration. The Hue profile shows the variation corresponding to the concentration leading to its suitability as feature.

The developed system extracts color intensities from the Hue component of segmented sub-images as features. The features extracted are mean, median, mode, maxi-

Table 1: Template for Fluorescence Transport Liquid Assay in 96-well format.

Assay	Test 1		Test 2		Test 3		Test 4		Test 5		Test 6	
Plate Columns	1	2	3	4	5	6	7	8	9	10	11	12
Plate Rows	1 (B)*	2 (C)‡	1 (B)*	2 (C)	1 (B)*	2 (C)‡	1 (B)*	2 (C)‡	1 (B)*	2 (C)‡	1 (B)*	2 (C)‡
A	3	4	3	4	3	4	3	4	3	4	3	4
B	5	6	5	6	5	6	5	6	5	6	5	6
C	7	8	7	8	7	8	7	8	7	8	7	8
D	9	10	9	10	9	10	9	10	9	10	9	10
E	11	12	11	12	11	12	11	12	11	12	11	12
F	13	14	13	14	13	14	13	14	13	14	13	14
G	15	16	15	16	15	16	15	16	15	16	15	16
H												

*B – Blank ‡C – Control

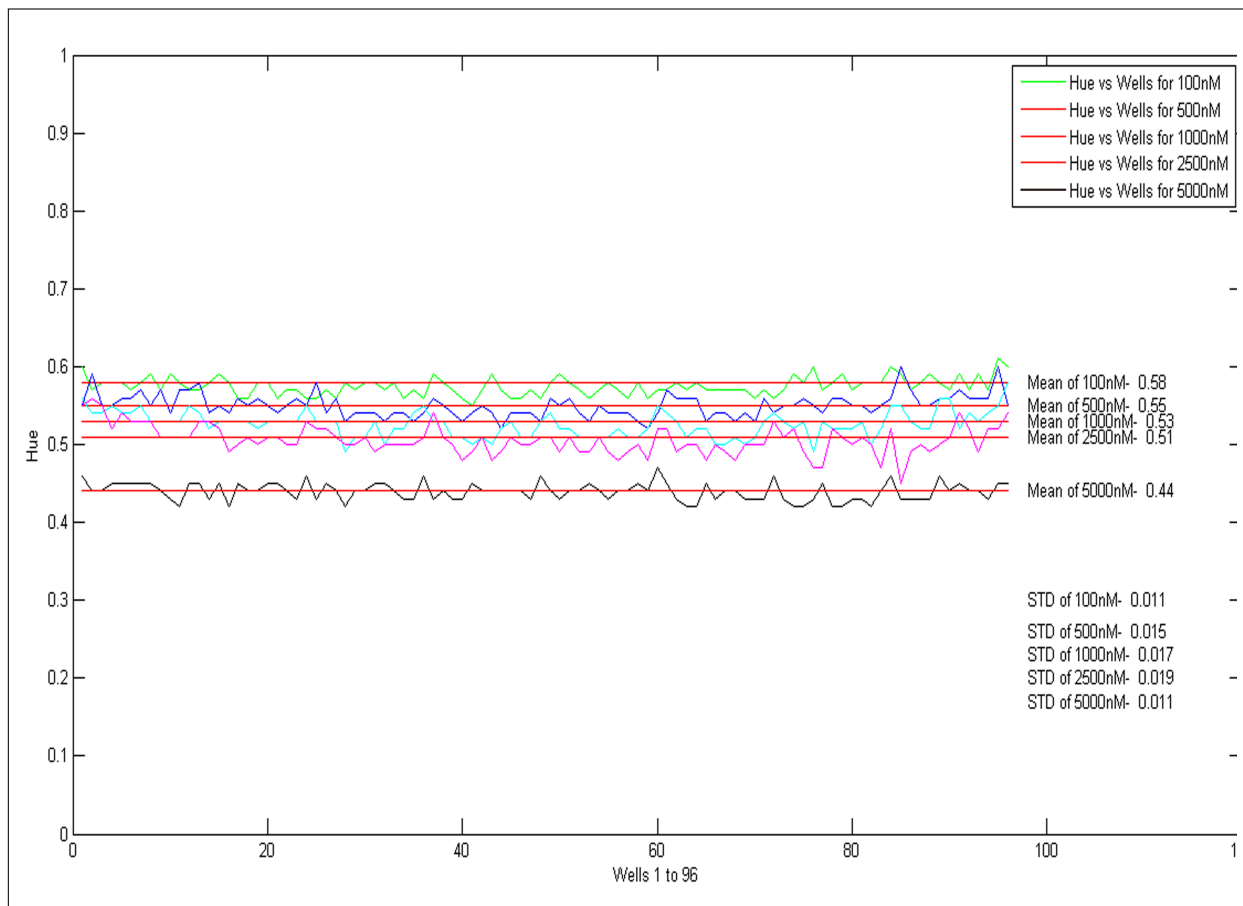


Figure 4: Hue Profile for Different Fluorescein Concentration in nanomolar excited by BLUE LED.

mum, and minimum are represented as f_{me} , f_{md} , f_{mo} , f_{ma} and f_{mi} respectively. With image I of size $m * n * p$ and segmented into sub-images of $H\{s\}$, where H represents the cell array, m represents rows, n represents columns, p represents pages which corresponds to their components and s represents the index of the sub-images, the reader calculates the features. T_1, T_2, T_3, T_4, T_5 , and T_6 represents the test groups re-assigned from the single cell array of $H\{s\}$ having a dataset of 16 sub-images in each groups. The index of the test groups is represented by t , which varies from 1 to 16 and not exceeding that. In the 3-page matrix of the HSV sub-images, converted from the 3-page RGB sub-images, the first page of HSV sub-image where $p = 1$ in the matrix $m * n * p$, is the Hue component represented as $T\{t\}(x, y, 1)$ where T is any test group. The x and y represents rows and columns of the segmented sub-images. The formula to calculate mean is given in equation (1).

$$f_{me} = \frac{1}{t} \sum_{t=1}^{16} [T\{t\}(x, y, 1)]. \quad (1)$$

For median (f_{md}), the data are sorted in ascending or descending order, and is calculated using equation (2).

$$f_{md} = \sum_{t=1}^{16} \frac{1}{2} \left[T\left\{\frac{t}{2}\right\}(x, y, 1) + T\left\{\frac{t}{2} + 1\right\}(x, y, 1) \right]. \quad (2)$$

Mode (f_{mo}) as feature extracted from sub-images by formula as in equation (3) where, l is the lower limit of modal class, F_m is the frequency of modal class, F_{pm} is the frequency of class preceding the modal class, F_{cm} is the frequency of class succeeding the modal class, h is the size of class interval. The above mentioned parameters are derived from $T\{t\}$.

$$f_{mo}(t) = l + \left(\frac{F_m - F_{pm}}{2F_m - F_{pm} - F_{cm}} \right) * h. \quad (3)$$

The features maximum (f_{ma}) and minimum (f_{mi}) are obtained from the equations (4) and (5) respectively.

$$f_{ma}(t) = \max_{t=1 \text{ to } 16} (T\{t\}). \quad (4)$$

$$f_{mi}(t) = \min_{t=1 \text{ to } 16} (T\{t\}). \quad (5)$$

The feature space is the vital factor, which determines the efficiency of the classifying system. Hence, analyzing the extracted statistical descriptive features of Hue by using different combination of the features and viewing it

in its feature space gives the suitability of the features as input feature vector in this classification. Figure 5 shows sample of different feature spaces of a test group in single image of microtiter plate generated. The implementation of k-means clustering for features in different feature spaces in an image comprising of six test groups, tested the stability of the cluster formation leading to the deduction of feature space for classification. The measure used in this deduction was, inter and intra cluster distance obtained from the clustering and comparing the labels of sub-images with assay template. From all other feature spaces, we found that the maximum-minimum feature space with maximum of Hue of a sub-image as feature vector 1 and minimum of Hue of a sub-image as feature vector 2 gives the feature space suitable for an efficient classification by giving us distant clusters with limited over-fitting when analyzed with other images.

3.3 Classification

A classification technique depends on the requirements of the pattern recognition problem. In this application, the problem definition of pattern recognition is, it has two-class classification with only optical intensity of sub-images as data to extract the feature. The optical intensity tends to vary at all times since living microorganism is used in the fluorescence transport liquid assay which reduces the probability of estimating the variation contributed by it. Due to this problem, a fixed threshold or adaptive threshold based classification for this two-class classification is not possible when live samples contribute to the unpredictable variation in data. Since this is a two-class classification, a minimum distance classifier [13] when fed with effective features that depicts distinct clusters is enough. However, high throughput analyses are in need in selecting such features which does not deviate even when there is variability introduced by the living microorganism. The classification technique here used is the k-means clustering technique [14].

The k-means clustering algorithm aims to minimize the objective function as in (6) defined by the distance metric of a data point and its corresponding cluster center. The distance measure used in this application is Squared Euclidean Distance.

$$J = \sum_{j=1}^k \sum_{i=1}^n \|x_i^{(j)} - c_j\|^2 \quad (6)$$

The $\|x_i^{(j)} - c_j\|^2$ is the chosen distance measure between a data point $x_i^{(j)}$ and the corresponding cluster center c_j . The k-means algorithm is composed of the following steps:

1. Initialize k center locations (i.e., c_1, \dots, c_k);
2. Assign each $x_i^{(j)}$ to its nearest cluster center c_j .
3. Update each cluster center c_j as the mean of all $x_i^{(j)}$ that have been assigned closest to it.

4. Recalculate the positions of the k centers.
5. Repeat steps 2, 3, and 4 until the centers no longer move. This produces a separation of the objects into groups from which the metric to be minimized can be calculated.

K-means clustering are widely used for image segmentation and when incorporated with feature sets it can classify [15, 16, 17]. The classification process for this application starts from the acquisition of assay in microtiter plate as an image I of size $m \times n \times p$. Then, the application segments single image into 96 sub-images and place it in the cell array $H\{s\}$. The $H\{s\}$ is re-assigned in accord to the assay template into six groups $T1\{t\}$, $T2\{t\}$, $T3\{t\}$, $T4\{t\}$, $T5\{t\}$, and $T6\{t\}$, with t being index of sub-images in test groups.

The application transforms these test groups from RGB color space to HSV color space and represented as $TH1\{t\}$, $TH2\{t\}$, $TH3\{t\}$, $TH4\{t\}$, $TH5\{t\}$, and $TH6\{t\}$. As discussed in Section 3.2, hue component from the HSV sub-images, represented as $TH1\{t\}(x, y, 1)$, $TH2\{t\}(x, y, 1)$, $TH3\{t\}(x, y, 1)$, $TH4\{t\}(x, y, 1)$, $TH5\{t\}(x, y, 1)$, and $TH6\{t\}(x, y, 1)$ for all the test groups.

Maximum-minimum features forms the feature space extracted by the formulae as in (4) and (5) for the classification. $f_{ma}^{TH1}\{t\}$, $f_{ma}^{TH2}\{t\}$, $f_{ma}^{TH3}\{t\}$, $f_{ma}^{TH4}\{t\}$, $f_{ma}^{TH5}\{t\}$, and $f_{ma}^{TH6}\{t\}$ represents the maximum of Hue for test groups $TH1\{t\}$, $TH2\{t\}$, $TH3\{t\}$, $TH4\{t\}$, $TH5\{t\}$, and $TH6\{t\}$ respectively, whereas, $f_{mi}^{TH1}\{t\}$, $f_{mi}^{TH2}\{t\}$, $f_{mi}^{TH3}\{t\}$, $f_{mi}^{TH4}\{t\}$, $f_{mi}^{TH5}\{t\}$, and $f_{mi}^{TH6}\{t\}$, represents the minimum of Hue for the same. $F1\{t\}$, $F2\{t\}$, $F3\{t\}$, $F4\{t\}$, $F5\{t\}$, and $F6\{t\}$ represents the feature space of $TH1\{t\}$, $TH2\{t\}$, $TH3\{t\}$, $TH4\{t\}$, $TH5\{t\}$, and $TH6\{t\}$ respectively, generated as per general expression $F \rightarrow f(v, w)$ where F is the feature space, $f(., .)$ is the function for feature elements v and w .

The function used in this application is to assign the f_{ma} features as x-axis elements and f_{mi} as y-axis elements in the feature space of F . Hence, $F1(t) \rightarrow f(f_{ma}^{TH1}\{t\}, f_{mi}^{TH1}\{t\})$, $F2(t) \rightarrow f(f_{ma}^{TH2}\{t\}, f_{mi}^{TH2}\{t\})$, $F3(t) \rightarrow f(f_{ma}^{TH3}\{t\}, f_{mi}^{TH3}\{t\})$, $F4(t) \rightarrow f(f_{ma}^{TH4}\{t\}, f_{mi}^{TH4}\{t\})$, $F5(t) \rightarrow f(f_{ma}^{TH5}\{t\}, f_{mi}^{TH5}\{t\})$, and $F6(t) \rightarrow f(f_{ma}^{TH6}\{t\}, f_{mi}^{TH6}\{t\})$.

These form as input to the k-means clustering with the two as number of clusters for each test group classification, represented by R for fast efflux and S for slow efflux for this application. $OH1\{t\}$, $OH2\{t\}$, $OH3\{t\}$, $OH4\{t\}$, $OH5\{t\}$, and $OH6\{t\}$, represents six different test output variables for the test groups $TH1\{t\}$, $TH2\{t\}$, $TH3\{t\}$, $TH4\{t\}$, $TH5\{t\}$, and $TH6\{t\}$, respectively. Let us represent k-means clustering based classification algorithm as a function whose notation is as in (7).

$$Label = Kmeans(F, n) \quad (7)$$

where, $Label$ is the cluster label index assigned to data index, by the clustering technique, $Kmeans$ represents the

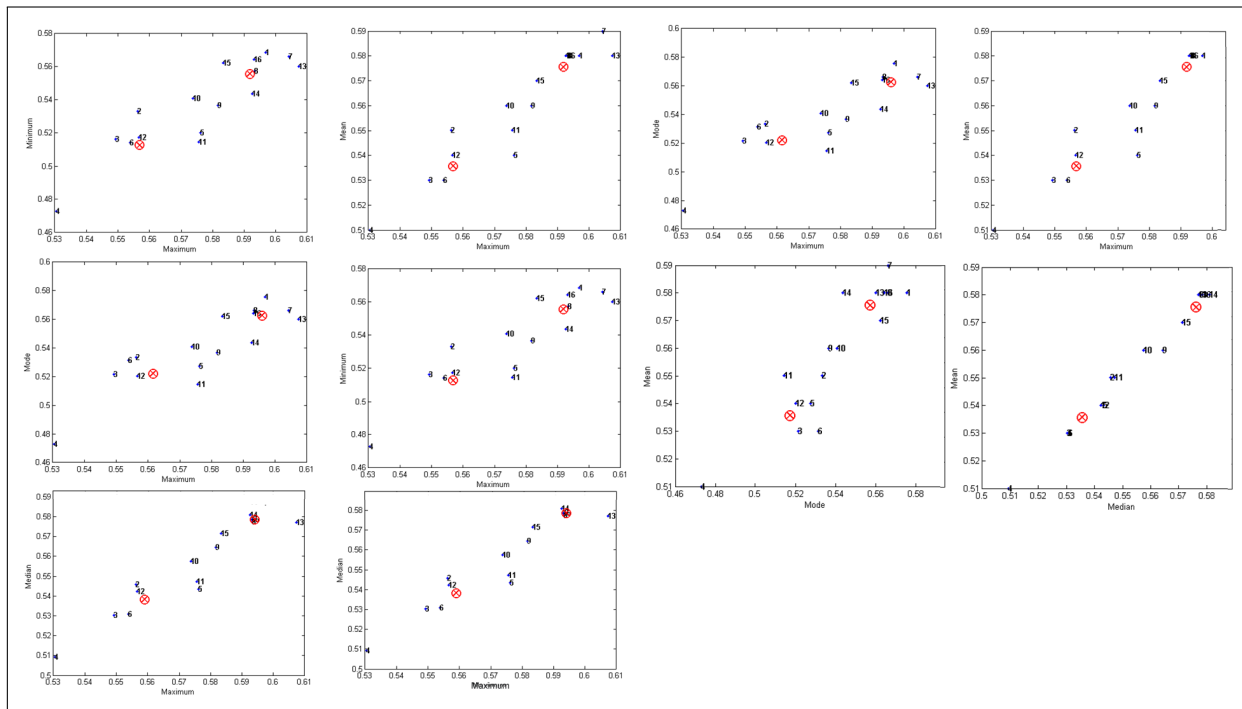


Figure 5: Different Feature Spaces Generated for Feature Selection.

function, F , the feature vector and n is the number of clusters. The application uses the above function for all test groups and obtains the cluster index.

$$OH1\{t\} = Kmeans(F1(t), 2) \quad (8)$$

$$OH2\{t\} = Kmeans(F2(t), 2) \quad (9)$$

$$OH3\{t\} = Kmeans(F3(t), 2) \quad (10)$$

$$OH4\{t\} = Kmeans(F4(t), 2) \quad (11)$$

$$OH5\{t\} = Kmeans(F5(t), 2) \quad (12)$$

$$OH6\{t\} = Kmeans(F6(t), 2) \quad (13)$$

The characters ‘R’ or ‘S’ representing fast and slow eflux respectively, replaces the index of the output variable of a single test assigned by k-means clustering. For each test, the classification gives output variables, which then re-assigned with indices along with content to a single cell array. $OH1\{t\}$, $OH2\{t\}$, $OH3\{t\}$, $OH4\{t\}$, $OH5\{t\}$, and $OH6\{t\}$, the test output variables, is re-assigned in to one single cell array $O\{s\}$, then re-ordered in matrix order 8×12 , for it to be displayed as result to the user.

Figure 6 shows the detailed system architecture of the reader system and a sample result along with the feature space of Test 5 with its centroids calculated by k-means clustering algorithm of the sample input image. There were no errors in classification by this technique for classifying the fluorescein concentrations that simulates the liquid transport assay, when Digital Camera was used for image acquisition; also paved the way for the usage of live samples such as Pathogens. Analyzing the variability introduced by a microorganism will lead to the incorporating changes to the algorithm of this reader system.

4 Results and Discussion

The suitability of k-means clustering technique for microtiter plate reader, which is a two-class pattern recognition application, depends on its accuracy and reproducibility. The classifier’s accuracy was 100% when tested with 20 microtiter plate images having a dataset of 1920 sub-images. In addition, the computational complexity of the k-means algorithm was overcome by reducing the dataset from 96 observations of a single image to 6 groups with 16 observations in each group in a single classification process which was discussed in Section 3.2 and Section 3.3. Since the classification of the reader was accurate and reproducible, an experiment is necessary to find when the accuracy deters. The experiment was carried out by using four test images differed only by the source excitation intensity.

As in Figure 2, the circuit of the SMD3528 blue LED uses a square trim potentiometer of resistance range 2k for intensity control. The electrical travel of the moving arm inside this 2k square trim potentiometer causes the variation in the driver current of the circuit due to change in its resistance, which in turn controls the luminous intensity of the source. The resolution having total pixels around 9 megapixels and the image size are same in all four different test images by the same imaging hardware, here a digital camera. The acquisition conditions of the test images are in detail as followed.

A blue filter placed below the microtiter plate filters the source. In addition, 0% electrical travel of the 2k square trim potentiometer allows maximum drive current to the circuit providing maximum luminous intensity of

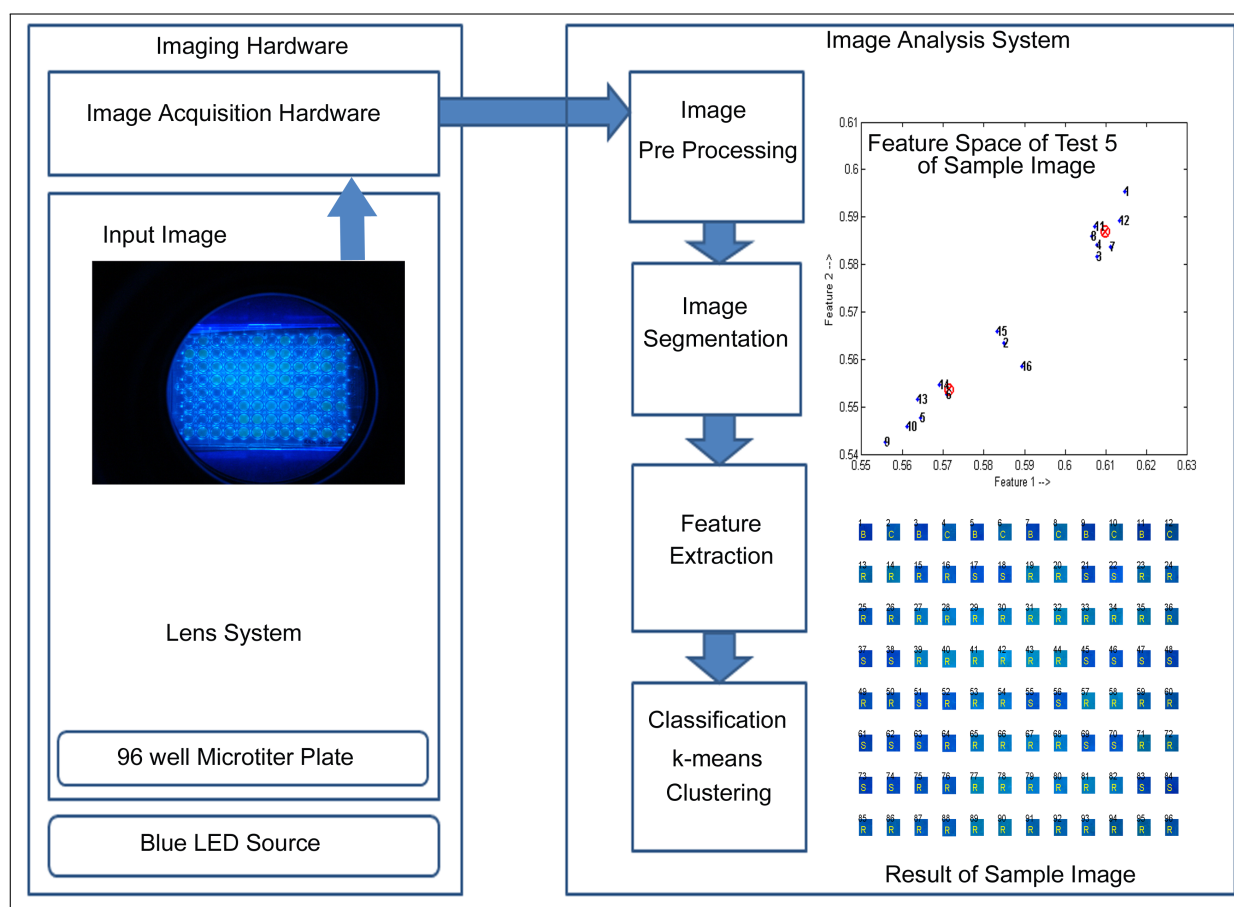


Figure 6: System Architecture of Microtiter Plate Reader System with Sample Analysis Process.

the source to the microtiter plate. Then the image acquired with these conditions by the digital camera having 9 megapixels CMOS sensor is the Test image 1. As for Test image 2, the conditions of Test image 1 are retained except for the change in the filtration of the excitation source which is, placing a green filter above the microtiter plate along with the blue filter placed below it. Test image 3 has the conditions of the Test image 2 with change only in the luminous intensity of the excitation source. The change was to alter the electrical travel from 0% to 30% 2k Ω square trim potentiometer causing reduction in the luminous intensity of the excitation source and acquire it as an image. For the Test image 4, the change from Test image 3 is only in electrical travel from 30% to 50% of the intensity controlling 2k Ω square trim potentiometer.

Figure 7 shows the Test Images 1 to 4 fed to the reader system as inputs. The Table 2 shows the classification accuracy for the test images fed as input to the developed system. From the Table 2 we see that Test images 1 and 2 offer an accuracy of 100% and reduced accuracy of other two images due to the decrement in the excitation intensity. Hence, we can deduce that an efficient classification by this technique for this application, will be achieved, if and only if with maximum intensity provided by the blue LED source and the quality of the image is retained with high resolution.

The usage of a statistical classifier such as k-means clustering have been effective in this is two-class pattern recognition application, even though the size of the classes varies. Although class discrimination in this application was challenging, the effectively selected feature space after the feature selection has overcome this and provided a good dataset to k-means algorithm leading to the development of an efficient microtiter plate reader. Computational statistical technique employed for the processes of feature selection, feature extraction, and classification from the sub-images of a single microtiter plate image had given an advantage of simplicity to the system. The algorithm of the reader has the facility to alter to the change incorporated in need of the requirement. The requirement for alterability are mentioned here, the format of microtiter plate used, automation of imaging, image segmentation, number of classes in classification, and change in the feature space.

In this image based analysis, quantification by microtiter assays is dependent on the resolution of the image acquisition system as well as the image analysis method. However, method as the one described will be of great value for those assays having two-class classification problem such as appearance or disappearance of fluorescence or a broad gradation of color intensity deciding the analyte's range of concentration in a semi quantitative man-

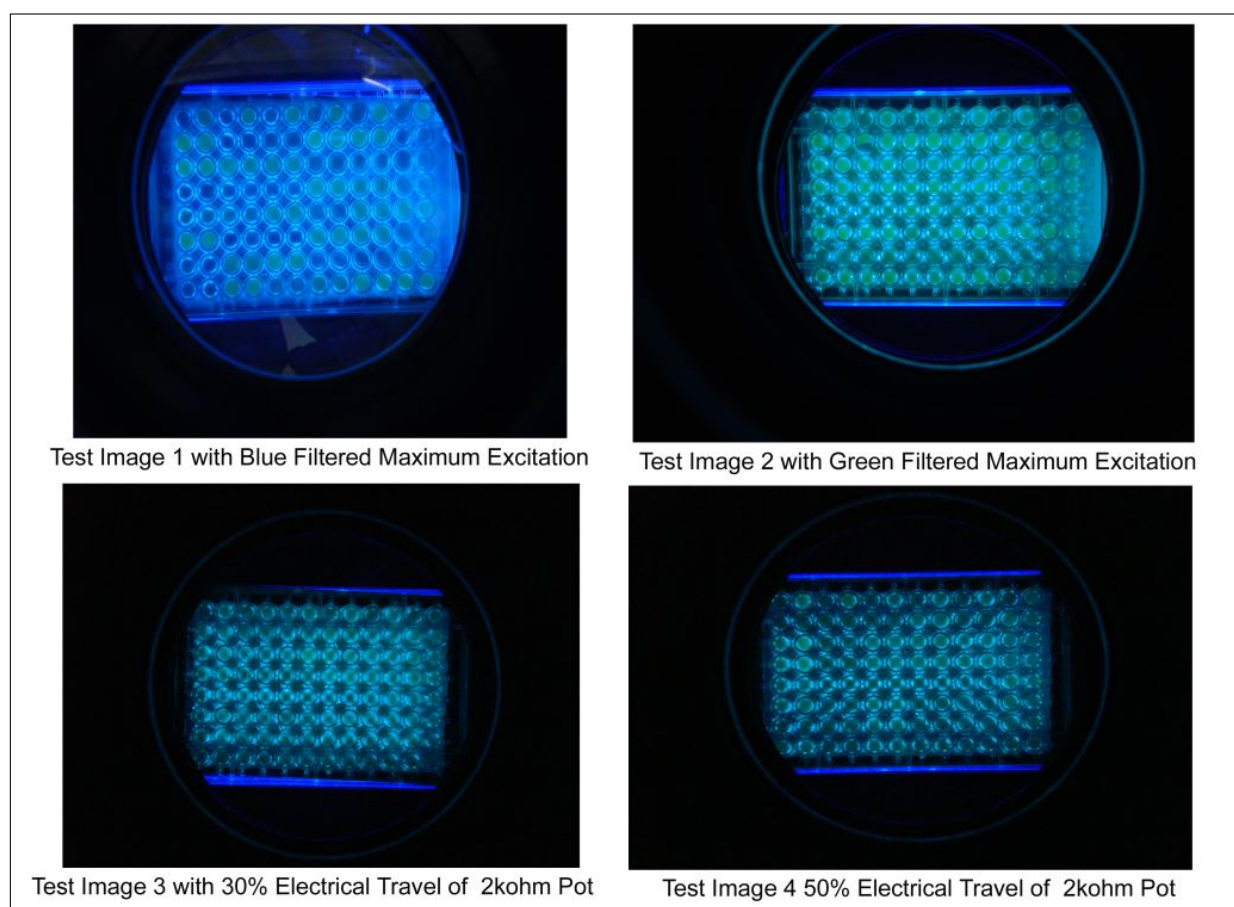


Figure 7: Test Images 1 to 4 of different Fluorescence Assays used for Performance Determination.

ner. When the image acquisition and software analysis are in perfect, the system could come close to the currently available scanning mode reader's performance with the decisive advantage of low cost, a big boon to clinical world.

5 Conclusions and Future Work

With the uniform illumination analysis and its dependency in degradation of classification performance, for this fluorescence assay it is deduced that, the SMD 3528 blue LED is suitable as source for this application, along with k-means clustering as the classification technique. This microtiter plate reader provides the maximum accuracy is achievable only when intensity of blue LED is max-

imum and the image quality retained as provided by a 9 megapixel-imaging sensor. The Future work is to experiment with low imaging sensor acquisition hardwares. In addition, to the above the goal is to achieve automation on imaging, image analysis and report generation. In addition, the assay when excited by the wavelengths in the visible-spectrum, captured as an image reduces the complexity in need of any heavy equipment. This reader system focused only on the 96-well format and easily alterable to any format, which is an advantage to this system. Thus using an image analysis system for such biotechnological assay reduces the time consumption, increases the efficiency, and converts all information to electronic data. The proposed imaging and image analysis system is very essential in the health care facilities due to its low complexity and cost effectiveness.

Table 2: Classification Accuracy of Different Assays.

Assay	Specificity %	Sensitivity %	Accuracy %
Test Image 1	100	100	100
Test Image 2	100	100	100
Test Image 3	97.92	97.92	97.92
Test Image 4	93.75	93.75	93.75

Acknowledgements

University Grants Commission (UGC), Government of India is acknowledged for financial support for the project in “Centre with Potential for Excellence in Environmental Science (CPEES), Anna University” and for the Fellowship of Junior Research Fellow to Durai Arun.

References

- [1] Vecht-Lifshitz SE, Ison AP, “Biotechnological applications of image analysis: present and future prospects”, *Journal of Biotechnology*, Volume 23, Issue 1, March 1992, Pages 1–18
- [2] Gonzalez, Digital Image Processing, 2nd Edition, Pearson Education Inc., 2008
- [3] Schalkoff, Artificial Neural Networks, McGrahill Publications, 1997
- [4] Earl Gose, Richard Johnsonbaugh, Steve Jost, Pattern recognition and Image Analysis, Prentice Hall PTR, 1996
- [5] Wendy L. Martinez, Angel R. Martinez, Computational Statistics Handbook with MATLAB, Chapman HALL/CRC, 2002
- [6] Anil K Jain, Fundamentals of Digital Image Processing, Pearson Education, Inc., 1989.
- [7] Muttan S, Durai Arun P, Sankaran K "Image Analysis System for 96-well Plate Fluorescence Assays" in the Proceedings of Third International Conference on Computing Communication Networking Technologies (ICCCNT 2012), Coimbatore, July 2012
- [8] Karthik G, Muttan S, Sankaran K "Optical Viewing System for 96 well Plate using Transilluminator" in Proceedings of Sixth National Conference on Recent trends in Information Technology and Communication, Chennai, pp 71-73, April 2012
- [9] Metin N. Gurcan, Anant Madabhushi, , Nasir M. Rajpoot, and Bulent Yener, “Histopathological Image Analysis: A Review,” *IEEE Reviews In Biomedical Engineering*, Vol.2, pp. 147-171, 2009
- [10] Le Jing, Li Yun, Hua Dengxin, Tan Linqiu, Cao Ning "Research on method of LED-induced chlorophyll fluorescence spectrum and image information acquisition" in the Proceedings of The Tenth International Conference on Electronic Measurement Instruments (ICEMI 2011)Pp. 311-315, 2011
- [11] Timothy, Transilluminator, U.S. Patent No. 5347342 issued at September 13, 1994, Available at (<http://www.google.com/patents/US5347342>)
- [12] Lei Li, Jin-Yan Li, Wen-Yan Ding. “A New Method For Color Image Segmentation Based on FSVM”, In Proceedings Of The Ninth International Conference On Machine Learning And Cybernetics, Qingdao, Pp. 664-779, 2009
- [13] Schalkoff, Pattern Recognition, 1st Edition, John Wiley Sons, 1992.
- [14] Anil K Jain, M.N. Murthy, P.J. Flynn, “Data Clustering: A Review”, *ACM Computing Surveys*, Vol. 31, No. 3, pp. 264-323, September 1999
- [15] G.Chamundeswari, G. Pardasaradhi Varma, Ch. Satyanarayana "An Experimental Analysis of K-means Using Matlab", *International Journal of Engineering Research Technology* (IJERT) ISSN: 2278-0181Vol. 1 Issue 5, July 2012
- [16] Surasit Songma Witcha Chimphlee Kiattisak Maichalernnukul Parinya Sanguansat "Classification via k-Means Clustering and Distance-Based Outlier Detection" in Proceedings of Tenth International Conference on ICT and Knowledge Engineering, Pp. 125-128, 2012
- [17] G.Subramanya Nayak Ottolina Davide Puttamadappa C "Classification of Bio Optical signals using K- Means Clustering for Detection of Skin Pathology" *International Journal of Computer Applications* (0975 – 8887) Volume 1 – No. 2 Pp 92-96